Sources of Variability in Transport and Deposition of Arctic Aerosols in Changing Climates

by

Chaoyi Jiao

A dissertation submitted in partial fulfillment
of the requirements for the degree of
Doctor of Philosophy
(Atmospheric, Oceanic and Space Sciences)
in The University of Michigan
2016

Doctoral Committee:

Associate Professor Mark G. Flanner, Chair
Assistant Professor Sarah M. Aciego
Associate Professor Christiane Jablonowski
Professor Joyce E. Penner

To my parents.

ACKNOWLEDGEMENTS

First and foremost, I would like to express my sincere gratitude to my advisor, Prof. Mark Flanner. Mark provided continuous guidance, support and encouragement which inspire and help me to conduct and finish my graduate research. Mark is a great mentor and I have learned a lot from his broad knowledge and experience in climate science. Mark is also a great scientist who has strong intellectual curiosity and inspires me to pursue research in many interesting topics. I would also like to thank my committee members: Prof. Sarah Aciego, Prof. Christiane Jablonowski and Prof. Joyce Penner. Their support and help were essential to this dissertation.

Many collaborators and colleagues provided help and support as well. Sarah Doherty and Sabine Eckhardt offered crucial help to the datasets used in this work. I also benefited a lot from many interesting conversations and discussions shared with Tami Bond, Thomas Kirchstetter, Liang Liu, Tianye Sun and Chelsea Preble. The collaborations with Drew Shindell and Yunha Lee helped me to broaden my research horizons. I also enjoyed many discussions shared with the group members: Justin Perket, Alex Gardner, Adam Schneider, Ayoe Buus Hansen, Deepak Singh and Jamie Ward. The comments and suggestions they have provided greatly benefited my research.

During the five years I have spent at Ann Arbor, I have shared the enjoyment of friendship with many amazing students and colleagues. I have enjoyed many adventures and conversations with my friends and it became a precious memory of graduate school. I thank them for their support and encouragement.

TABLE OF CONTENTS

LIST OF FIGURES

Figure

LIST OF TABLES

Table

ABSTRACT

Sources of Variability in Transport and Deposition of Arctic Aerosols in Changing Climates

by

Chaoyi Jiao

Chair: Mark G. Flanner

Light absorbing aerosols affect Arctic climate by reducing the albedo of snow and ice, increasing atmospheric solar heating, and accelerating the melting of the cryosphere. Previous studies have indicated that the reduction of snow and ice albedo caused by light absorbing aerosols is a significant source of Arctic warming and sea ice retreat. Thus, accurate numerical representation of the states and variability of aerosols in the Arctic is important for advancing our understanding of the Arctic and global climate. Although the developments of climate models have led to substantial improvements in the simulated Arctic aerosol fields, notable disagreements still exist between the models and observations.

This thesis assesses sources of uncertainties in aerosol related processes and explores possible improvements to aerosol simulations, with a focus on the Arctic region. Firstly, I evaluate concentrations and radiative effect of black carbon (BC, which is the most important component of light absorbing aerosols) in snow with an ensemble of climate models and ground measurements. Results show the inter-model variation

is large and the deposition processes dominate the model variance. The multi-model mean estimate of BC in snow radiative effect averaged over the Arctic is $0.17\,\mathrm{W\,m^{-2}}$, after correcting the model biases with observations. Secondly, I investigate how two processes that govern the aerosol distributions may change with future climate warming. I find the changing circulation patterns due to enhanced Arctic warming will promote the transport of aerosol tracers emitted from East Asia and West Europe. Meanwhile, these changes inhibit the poleward transport of aerosol tracers emitted from North America. Another experiment with realistic treatments of aerosol deposition processes reveals that wet removal is the dominant process determining the aerosol distribution in the Arctic. I estimate that the Arctic BC burden may decrease by 13.6% by the end of 21st century due solely to changes in aerosol transport and deposition. Thirdly, I conduct a sensitivity study to explore the influences of physical parameters, model resolution and emission patterns on the modeled Arctic aerosol distributions. Analysis shows that the simulated aerosol fields are most sensitive to the parameters associated with aerosol aging and wet deposition processes, especially in the Arctic. Further comparisons with aircraft measurements indicate that by adjusting these parameters, the biases between models and observations can be reduced substantially in the Arctic. This study provides a comprehensive analysis of aerosol transport and deposition processes in climate models and outlines further improvements.

CHAPTER I

Introduction

1.1 Aerosols and Climate

Aerosols originating from natural and anthropogenic sources can interact with radiation and clouds, and they have important and unique influence on the climate system. Major aerosol constituents include sulphate, nitrate, ammonium and sea salt, and organic aerosol (OA), black carbon (BC), mineral dust and primary biological aerosol particles (PBAPs). The majority of sulphate, nitrate and ammonium aerosols come from the oxidation of precursor gases, which mainly originate from anthropogenic sources in present day climate. Organic aerosol and black carbon are introduced into the atmosphere from anthropogenic sources such as fossil fuels and biofuels combustion, as well as natural sources like biomass burning. Organic aerosol can also be generated from some biogenic sources and non-combustion anthropogenic activities. Mineral dust and sea salt primarily originate from natural processes like wind erosion, disintegration of larger soil particles and wave breaking. Primary biological aerosol particles mainly come from the terrestrial ecosystems (*IPCC*, 2013).

Aerosols in the atmosphere are generally removed with dry deposition, wet deposition and sedimentation processes. The typical atmosphere lifetime for aerosol ranges from 1 day to 1 week, depending on the location of emission source, aerosol size and hygroscopicity, meteorological conditions and the rates of physical and chemical reac-

tions with gases and other aerosols. Though aerosols have much shorter atmosphere lifetime compared to some climate forcing agents like carbon dioxide or methane, their impact on the climate system is important and profound (e.g., *Kaufman et al.*, 2002; *Ghan and Easter*, 2006; *Koch et al.*, 2009a; *Myhre et al.*, 2009; *Stevens and Feingold*, 2009; *Penner et al.*, 2011; *Kahn*, 2012). The fifth assessment report of the Intergovernmental Panel on Climate Change (IPCC AR5) estimates the total effective radiative forcing (ERF) due to anthropogenic aerosols is $-0.9\,\mathrm{W\,m^{-2}}$ (-1.9 to $-0.1\,\mathrm{W\,m^{-2}}$) with medium confidence (*IPCC*, 2013). This estimate includes aerosol radiation interactions and rapid adjustments for aerosol cloud interactions. It does not take the radiative forcing (RF) from absorbing aerosols in snow and sea ice into consideration, which is assessed separately and will be discussed in details in Section 1.2.3.

Aerosols can directly scatter or absorb shortwave solar radiation and have both regional and global impacts on the radiative effects and energy budgets (e.g., *Kaufman et al.*, 2002; *Schulz et al.*, 2006; *Koch et al.*, 2009a; *Flanner*, 2013; *Myhre et al.*, 2013). Sulphate, nitrate, most of organic aerosol and sea salt are light scattering aerosols which generally increase the reflectance of the planet (e.g., *Koch et al.*, 2009a; *Kahn*, 2012). Thus excerting a cooling effect on the climate system. Meanwhile, black carbon has large mass absorption efficiency in the shortwave band. Thus it can absorb solar radiation and warm the climate system (e.g., *Ramanathan and Carmichael*, 2008; *Flanner*, 2013). Other aerosols such as mineral dust and brown carbon (BrC, a type of light-absorbing organic carbon) have intermediate light scattering and absorption properties, and their effects on the climate system depend on the local environment.

Aerosols can affect the distribution and properties of clouds and indirectly induce a pronounced radiative forcing to the climate system (e.g., *Kaufman et al.*, 2002; *Stevens and Feingold*, 2009; *Penner et al.*, 2011). This process is also referred to aerosol's indirect effect. Many aerosol species, such as sulphate, nitrate, organic

carbon and sea salt, can serve as cloud condensation nuclei (CCN) (e.g., *Novakov and Penner*, 1993). In cold environments, black carbon, mineral dust and PBAPs may serve as ice nuclei (IN) (e.g., *DeMott et al.*, 2010; *Hoose and Möhler*, 2012). The presence of such aerosols in the liquid, ice or mixed phase cloud system can alter the size and number of cloud droplets and influence the phase changes between liquid and ice. For example, studies have shown that with increased CCNs, the liquid cloud will have more droplets but with small size and greater total droplet surface area. This process will increase the albedo of liquid cloud and enhace its cooling effect in the climate system by reflecting more solar energy back to the space. It may also influence the cloud's lifetime by either promoting or inhibiting precipitation. The magnitude of radiative forcing due to aerosol cloud interaction still remains largely uncertain due to its complexity.

1.2 Snow, Aerosols and the Arctic Climate

1.2.1 Snow and the Arctic Climate

The Arctic environment is unique with its large snow, sea ice and glacier covers. The typical land surface substances are dark in the shortwave band and absorb a large portion of incoming solar radiation. But as the temperature is low in the Arctic and a significant fraction of its surface is covered with snow and sea ice, this region has a much larger reflectivity, or albedo, compared to the global mean.

The albedo of a surface depends on the surface's properties, the wavelength and angular distribution of incident radiation. A larger value of albedo means the surface is more reflective and absorbs less radiation. The common land surfaces have small albedo in the spectrum of solar radiation (e.g., *Briegleb and Ramanathan*, 1982; *Henderson-Sellers and Wilson*, 1983; *Lawrence and Chase*, 2007). For example, land surfaces covered with grass, tundra and forrest generally have albedo ranging from

0.02 to 0.10 in the visible band. The albedo of soil surface depends on the type and condition of the soil, and typically ranges from 0.05 to 0.18. Desert surface has a larger albedo which ranges from 0.28 to 0.42. Thus in the Arctic, the snow-free land surface has small albedo and can absorb most of the incoming solar radiation during sunlit season. Ice-free ocean surface is also very dark in the solar spectrum and its albedo depends greatly on the solar zenith angle for direct solar radiation. The ice-free ocean's albedo normally ranges around 0.05 to 0.08. However, the land or ocean surfaces covered with snow and sea ice have much higher albedo and can reflect a great fraction of downwelling solar radiation back to atmosphere. The albedo of clean snow is very large and ranges from 0.76 to 0.95 depending on its age (*Briegleb and Ramanathan*, 1982). The sea ice surface is quite reflective as well, especially when it is covered by fresh snow.

1.2.2 The Albedo Feedback

Since the albedo of the Arctic region depends highly on the snow and ice cover, the melt of snow and sea ice introduces a great threat to the climate system. A well studied positive climate feedback mechanism, called albedo feedback, is associated with this process. The albedo feedback occurs when the snow and sea ice in the cryosphere melt due to increased global mean temperature. Then the underneath land and ocean surfaces, with much smaller albedo, will absorb a greater fraction of incoming solar radiation. This process will warm the Arctic climate and enhance the climate warming. *Flanner et al.* (2009) estimated the albedo feedback induced by the north hemisphere cryosphere is 0.3 to $1.1\,\mathrm{W\,m^{-2}\,K^{-1}}$based on observation analysis. The albedo feedback is self-reinforced and among the most important climate feedback processes.

1.2.3 Influence of Ligth-absorbing Aerosols on Arctic Climate

Typically, aerosols affect the climate when they are suspended in the atmosphere and interact with radiation and clouds. Once aerosols deposit to the land or ocean surfaces, their direct radiative forcing on the climate system vanishes. But if the light absorbing aerosols deposit on snow or sea ice surfaces, which are very reflective to solar radiation, they can reduce the surface albedo and increase radiative absorption (e.g., *Hansen and Nazarenko*, 2004; *Jacobson*, 2004; *Flanner et al.*, 2007; *Bond et al.*, 2013). Such light absorbing aerosols consist of black carbon (BC), brown carbon and some types of dust. Among them, the BC aerosol has the strongest light absorption efficiency. BC originates mostly from the incomplete combustion of biomass and fossil fuels and its emission has increased substantially during the industrial era (*Ito and Penner*, 2005; *Bond et al.*, 2013). Studies have shown that during the sunlit season, the reduction of the cryposphere albedo induced by BC and other light absorbing aerosols increases surface temperature and accelerates melting of snow and sea ice (e.g., *Hansen and Nazarenko*, 2004; *Flanner et al.*, 2007; *Bond et al.*, 2013). Combined with the albedo feedback in the climate system, the light absorbing aerosols in snow and ice can introduce a high climate forcing efficacy. Moreover, the direct atmospheric aerosol effect is positive at high latitudes as well, due to aerosol absorption over high albedo surfaces such as snow, ice and high clouds (e.g., *Shindell and Faluvegi*, 2009; *Myhre et al.*, 2013). Thus is our interests to understand and better constrain and understand how the light absorbing aerosols can be transported to and deposited in the Arctic, influencing the local and global climate.

1.3 Aerosol Simulation in the Community Earth System Model

1.3.1 The Community Earth System Model

The Community Earth System Model (CESM) is a state-of-the-art Earth System Model (ESM) for simulating the full spectrum of climate state and variability (e.g., *Hurrell et al.*, 2013). An ESM has the capability to simulate fully coupled climate processes, which may include the states and variations of the atmosphere, ocean, land, sea ice, glacier and land ice, biogeochemical cycles and the ecosystems. Other widely used ESMs are those developed by the Geophysical Fluid Dynamics Laboratory, the Max Planck Institute for Meteorology and the Met Office of Hadley Centre. The CESM is developed and maintained by the National Center for Atmospheric Research (NCAR) and many other collaborating institutes.

The major components of the CESM version 1 (CESM1) include the Community Atmosphere Model version 5 (CAM5), the Community Land Model version 4 (CLM4), the Community Ice CodE version 4 (CICE4), the Parallel Ocean Program version 2 (POP2) and the Glimmer Community Ice Sheet Model (Glimmer-CISM). CAM5 is an atmospheric general circulation model and incorporates substantial improvements for the treatments of liquid and ice clouds, water vapor and aerosols (e.g., *Gettelman et al.*, 2008; *Morrison and Gettelman*, 2008; *Liu et al.*, 2012; *Ghan et al.*, 2012). CLM4 is a land process model which can simulate the interactions between physical, chemical and biological processes within the terrestrial ecosystems and climate systems (e.g., *Oleson et al.*, 2010; *Lawrence et al.*, 2011). Coupled with the SINCAR (Snow, Ice, and Aerosol Radiative) model, CLM4 can represent the aerosol cycling process and radiative effects of land snow as well (*Flanner et al.*, 2007). CICE4 simulates sea ice thickness and distributions and can also resolve the deposition and cycling of BC and dust in the ice. An improved treatment for the multiple-scattering of shortwave radiation is also included in CICE4 (e.g., *Briegleb and Light*, 2007; *Holland et al.*,

2012). POP2 is an ocean general circulation model and can simulate various processes in the ocean climate. Glimmer-CISM is a thermomechanical ice sheet model which can represent the ice sheet movements and has parametrized treatments for basal sliding and iceberg calving. These components of CESM, together with many other improved and advanced modules and subroutines, have the capability to simulate and represent the fully coupled climate, biogeochemistry and ecology system. The CESM is a powerful and flexible tool for advancing our knowledge and understanding of the climate system.

1.3.2 Aerosol Simulations in CESM

CESM1 uses the Modal Aerosol Module (MAM) for the simulations of aerosol processes. The MAM is the successor of the Bulk Aerosol Module (BAM), which can also be coupled with CESM1 as well. Unlike MAM, the bulk method applies external mixing between different aerosol species and often prescribes a constant e-folding time for aerosol aging process. The BAM simulates the mixing ratios of aerosols with prescribed fixed size distribution and cannot resolve the aerosol size distribution variations. The assumption of external mixing of aerosols also limits its ability to properly represent the aerosol radiative forcing in the atmosphere. An advantage of BAM is the ease of which new aerosol tracers can be introduced to the code. Due to this merit, BAM is applied for studies described in Chapter III.

MAM has fundamental changes and sophisticated improvements for aerosol treatments compared to its predecessor. Two versions of MAM have been developed, which are the MAM with three lognormal modes (MAM3) and the MAM with seven lognormal modes (MAM7). The MAM7 is a more complete version and has comprehensive aerosol treatment, yet is quite computationally expensive. The MAM3 only has three aerosol modes and simplifies some aerosol treatments. Compared to the seven modes module, MAM3 requires relatively less computational resources and is

suitable for long-term climate integration.

The MAM7 includes seven different aerosol modes which are: Aitken, accumulation, primary carbon, fine dust, fine sea salt, coarse dust and coarse sea salt modes (*Liu et al.*, 2012). The prescribed geometric standard deviations (σ_g) and dry diameter size ranges for each mode in MAM7 are: Aitken (σ_g= 1.6, 0.015 – 0.052 µm), accumulation mode (σ_g= 1.8, 0.056 – 0.26 µm), primary carbon (σ_g= 1.6, 0.039 – 0.13 µm), fine sea salt (σ_g= 2.0, 0.095 – 0.56 µm), fine dust (σ_g= 1.8, 0.14 – 0.62 µm), coarse sea salt (σ_g= 2.0, 0.63 – 3.70 µm) and coarse dust (σ_g= 1.8, 0.59 – 2.75 µm). The temporal and spatial variations of size distributions in each mode are calculated prognostically in MAM7. In each mode, different aerosol species are internally mixed and their mass mixing ratios are predicted. The primary carbon mode contains freshly emitted primary organic matter (POM) and black carbon (BC) aerosols. When sulphate, ammonium or other semi-volatile organics condense on the surface of POM and BC aerosols, they are transferred to the accumulation mode. Thus this module has explicit treatment for the aging process of BC and POM, which is a key process determining the temporal and spatial distribution of these aerosols. The aerosols in the primary carbon mode can also coagulate with species in Aitken and accumulation modes. Secondary organic matter (SOM, or secondary organic aerosol, SOA) is assumed to be in the Aitken and accumulation modes. The soil dust and sea salt aerosols are emitted to their fine or coarse modes correspondingly, depending on their sizes. The sea salt can internally mix with aerosols in the Aitken and accumulation modes as well. The interaction between aerosol and stratiform cloud is calculated explicitly in MAM7. While in convective cloud, the aerosol activation process is predicted with an implicit method (*Easter et al.*, 2004; *Ghan and Easter*, 2006; *Liu et al.*, 2012).

A simplified version of the modal aerosol module is MAM3. In MAM3, there are three modes which are: Aitken, accumulation and coarse modes. Simplifications

in MAM3 include that the primary carbon is emitted into the accumulation mode and assumed to be internally mixed with other aerosols immediatedly. A single coarse mode is used to predict all the dust and sea salt with large sizes, and the fine dust and sea salt modes are merged into the accumulation mode instead. The prescribed geometric standard deviations (σ_g) and dry diameter size ranges for modes in MAM3 are: Aitken (σ_g= 1.6, 0.015 – 0.053 µm), accumulation mode (σ_g= 1.8, 0.058 – 0.27 µm), coarse mode (σ_g= 1.8, 0.80 – 3.65 µm). The total number of simulated aerosol tracers in MAM3 is less than half of those in MAM7 (*Liu et al.*, 2012).

1.3.3 The Limitations of Aerosol Simulations in CESM

Liu et al. (2012) assessed the performance of MAM by comparing the simulated aerosol mass and number concentrations, size distributions and optical depths with a variety of measurements. They found that the model is able to predict the general characteristics of the spatial and temporal distribution of aerosol field. Yet numerous biases also exist. The model underestimates the total aerosol optical depth (AOD) globally, compared to the AOD measurements provided by the AERONET (AErosol RObotic NETwork) and satellite observations. Another caveat is that this model significantly underestimates BC concentrations in the Arctic. As we discussed in Section 1.2.3, the absorbing aerosols, such as BC, can have strong impact on the Arctic climate. Thus the biases between modeled and observed BC concentrations at high latitudes can potentially undermine the assessment of Arctic climate change.

Wang et al. (2013) identified several key processes which are not well represented in CAM5. They implemented a series of improvements related to the aerosol aging and wet removal processes in MAM. With these modifications and improvements, the biases between simulated BC concentrations in the Arctic and surface and aircraft measurements were reduced substantially. Their modifications also improve the modeled aerosol optical depth and mixing ratios in other regions as well. We apply these

modifications for studies described in Chapter IV.

1.4 Organization of Research

In this study, we will explore different aspects which may contribute to the developments of aerosol simulations in climate models, with a focus on the Arctic region. Firstly, in Chapter II, we assess the vertically resolved BC in snow concentrations simulated with the aerosol deposition fluxes from 25 climate models contributing to two phases of the AeroCom (Aerosol Comparisons between Observations and Models) project. We discuss the agreements and biases between the simulated BC in snow concentrations and field observations taken from an extensive Arctic measurement campaign (*Doherty et al.*, 2010). Different factors that may contribute to these biases are also analyzed with sensitivity studies. This chapter also provides a measurement-constrained estimate of BC in snow radiative effect.

In Chapter III, we focus on two processes that govern the aerosol distributions in the Arctic, which are atmospheric transport and deposition. In this study, we investigate the effects of aerosol transport and deposition separately. Furthermore, we design experiments to explore how these processes may change in the context of global warming, and how the distributions of Arctic aerosols may respond.

Chapter IV discusses a parameter sensitivity study which is designed to further improve the simulated vertical distribution of black carbon aerosol in the Arctic. We perturb a series of physical parameters which control the aerosol aging, activation in convective clouds and wet and dry deposition processes to study their impact on Arctic BC fields. The sensitivity of model resolution and emission inventory is also explored. This provides guidances for further optimizing the aerosol simulations in CAM5. Chapter V summarizes major results and conclusions of the dissertation and identifies relevant future studies.

CHAPTER II

Assessment of Black Carbon in Arctic Snow and Sea Ice with AeroCom Models

As appears in:
Jiao, C., Flanner, M. G., Balkanski, Y., Bauer, S. E., Bellouin, N., Berntsen, T. K., Bian, H., Carslaw, K. S., Chin, M., De Luca, N., Diehl, T., Ghan, S. J., Iversen, T., Kirkevåg, A., Koch, D., Liu, X., Mann, G. W., Penner, J. E., Pitari, G., Schulz, M., Seland, Ø., Skeie, R. B., Steenrod, S. D., Stier, P., Takemura, T., Tsigaridis, K., van Noije, T., Yun, Y., and Zhang, K. (2014): An AeroCom assessment of black carbon in Arctic snow and sea ice, *Atmos. Chem. Phys.*, 14, 2399-2417, doi:10.5194/acp-14-2399-2014.

2.1 Introduction

Black carbon (BC) is a light-absorbing carbonaceous component of aerosol originating from the incomplete combustion of biomass and fossil fuel. The amount of BC emitted into the atmosphere has increased substantially during the industrial era (*Bond et al.*, 2007, 2013). The spatial pattern of BC emissions has also shifted considerably, with North American emissions likely decreasing since the early 20th century (*McConnell et al.*, 2007), European emissions declining after the 1960s, and emissions from Asia increasing during recent decades (e.g., *Bond et al.*, 2007). Global BC emissions from fossil fuel and biofuel combustion have increased by more than a factor of 4 since 1850.

BC aerosols can influence climate through different ways, including direct radiative forcing, semi-direct cloud effects, indirect cloud effects, and deposition to snow and ice surfaces (e.g., *Menon et al.*, 2002; *Hansen and Nazarenko*, 2004; *Jacobson*, 2004; *Stier et al.*, 2007; *Flanner et al.*, 2009; *Koch and Del Genio*, 2010; *Koch et al.*, 2011; *Bond et al.*, 2013). During the sunlit seasons, the reduction of snow and ice albedo caused by BC increases surface solar heating and can accelerate melting of the cryosphere. This process triggers albedo feedback in the climate system, leading to higher efficacy than other forcing mechanisms (*Hansen and Nazarenko*, 2004). The instantaneous increase of solar radiation absorption caused by the presence of BC in snow and sea-ice, termed the BC-in-snow radiative effect, has been estimated from forward modeling with global aerosol and climate models (GCMs), but has uncertainties originating from global BC emissions, atmospheric transport and deposition processes, model snow and ice cover, BC optical properties, snow effective grain size, coincident absorption from other light-absorbing constituents, and post-depositional transport of BC with meltwater (*Flanner et al.*, 2007; *Bond et al.*, 2013). *Flanner et al.* (2007) quantified some of these uncertainties using a series of GCM simulations, finding that BC emissions and snow aging (which determines the snow effective grain size) are large sources of uncertainty. They did not, however, examine uncertainty or inter-model variability associated with BC transport and deposition to snow surfaces, a topic explored in this study.

Measurements of BC in Arctic snow and ice provide an opportunity to evaluate model deposition of BC at high latitudes and constrain the Arctic BC-in-snow radiative effect (*Dou et al.*, 2012; *Lee et al.*, 2013b). *Doherty et al.* (2010) report on a comprehensive survey of Arctic BC-in-snow measurements collected during 2005–2009. More than 700 snow samples were collected, melted, filtered, and analyzed for BC mass using the spectral distribution of light absorption through the filter. This publicly-available dataset, with extensive spatial distribution over the Arctic, provides

a useful basis for conducting a multi-model evaluation of Arctic BC deposition.

The Aerosol Comparisons between Observations and Models (AeroCom) project was initiated for the aerosol observation and modeling communities to synthesize results in order to improve aerosol simulation skills (*Kinne et al.*, 2006; *Schulz et al.*, 2006; *Textor et al.*, 2006, 2007; *Koffi et al.*, 2012; *Myhre et al.*, 2013; *Samset et al.*, 2013; *Stier et al.*, 2013). A large number of global aerosol models have contributed to the AeroCom archive. Several studies have used this archive to evaluate model spatial and temporal distributions of aerosol properties (e.g., *Textor et al.*, 2007; *Koch et al.*, 2009b; *Koffi et al.*, 2012; *Myhre et al.*, 2013). For example, *Koch et al.* (2009b) evaluate AeroCom models against surface and aircraft measurements of BC concentrations, aerosol absorption optical depth (AAOD) retrievals, and BC column estimates. They find the largest model diversity in northern Eurasia and the remote Arctic, and show that most models simulate too little BC in the springtime lower Arctic atmosphere relative to aircraft measurements, but models may simulate too much BC in the higher Arctic atmosphere. *Schwarz et al.* (2010) also find AeroCom models underestimate BC in the lower Arctic troposphere compared with observations from the HIPPO (High-performance Instrumented Airborne Platform for Environmental Research Pole-to-Pole Observations) campaign.

Other studies of large model ensembles also find important features that are valuable for understanding Arctic pollutant impacts. *Shindell et al.* (2008) apply 17 models to assess the pollution transport to the Arctic. They find that inter-model variations are large and originate mainly from differences in the representations of physical and chemical processes, but the relative importance of emissions from different regions is robust across models. North America is the major contributor to Arctic ozone and BC deposited on Greenland, whereas European emissions dominate the total BC deposition elsewhere in the Arctic. *Lee et al.* (2013b) evaluated historical BC aerosols simulated by 8 ACCMIP (The Atmospheric Chemistry and Climate Model

Intercomparison Project) models against observations. They found that year 2000 global atmospheric BC burden varies by about a factor of 3 among models, despite all models applying the same emissions. Modeled BC concentrations in snow and sea ice were generally within a factor of 2–3 of observations, while the seasonal cycle of atmospheric BC in the Arctic was poorly simulated.

Though all AeroCom models simulate aerosol deposition to the surface, most of them do not simulate vertically-resolved concentrations of BC in snow and sea-ice, governed, e.g., by meltwater removal, fresh snowfall, and sublimation. The simulation of such distributions is critical for meaningful evaluation of model data against surveys like that of *Doherty et al.* (2010), which includes measurements of BC at different snow depths and in snow subject to different climate conditions. New capabilities in the Community Land Model (CLM) and Community Ice CodE (CICE) components of the Community Earth System Model (CESM) permit 1) the simulation of vertically-resolved BC concentrations in snow and sea-ice, and 2) the use of prescribed aerosol deposition fields, such as those generated from AeroCom models, to drive the offline land and sea-ice models. Here, we exploit these capabilities in dozens of CLM and CICE simulations to explore inter-model variabilities in Arctic BC transport and deposition, and evaluate subsequent impacts on Arctic BC-in-snow radiative effects. We also explore the sensitivity of model–measurement comparisons to meltwater removal efficiency, one of the key uncertainties in simulated BC-in-snow forcing (*Flanner et al.*, 2007; *Bond et al.*, 2013), and consistency between model meteorology and deposition. We have also applied the framework developed here in recent collaborative efforts to quantify radiative effects from ACCMIP models (*Lee et al.*, 2013b; *Shindell et al.*, 2013).

2.2 Observational Data

We use the measurements of BC-in-snow concentration published by *Doherty et al.* (2010). These measurements were conducted in different sectors of the Arctic during 2005–2009, mostly during March to August. The snow samples were generally collected in locations far from anthropogenic sources (e.g. roads, villages and cities) so they represent regions which are not strongly affected by local pollution. Samples collected near the city of Vorkuta, Russia, have high BC-in-snow concentrations (i.e. $>> 100\,\mathrm{ng\,g^{-1}}$), however, indicating influence of local pollution, and are also included in our model evaluation.

Doherty et al. (2010) report three types of BC concentrations from their measurements: maximum BC, estimated BC and equivalent BC. The estimated BC is the estimated true mass of black carbon per mass of snow by using the wavelength-dependence of the measured absorption, and the estimate BC is used for comparison with simulated BC mass in our study. The mass-absorption cross-section (MAC) of BC assumed in the analysis was $6.0\,\mathrm{m^2\,g^{-1}}$at 550 nm. If actual BC MAC was higher (lower) than that assumed by *Doherty et al.* (2010), actual BC mass in the snow was lower (higher). The non-BC light-absorbing aerosols are likely dominated by organic carbon (OC) and dust. A more detailed description of the method is provided by *Grenfell et al.* (2011). Most models do not differentiate aerosol species such as brown carbon, which is generally grouped into the OC category in emission inventories employed by models. The observations include 797 samples in total, and have been grouped into 8 different regions: (1) Arctic Ocean, (2) Canadian Arctic, (3) Alaska, (4) Canadian Sub-Arctic, (5) Greenland, (6) Ny-Ålesund, (7) Tromsø, and (8) Russia. Here we adopt the same partitioning of regions. The locations of these samples are shown in Figure 2.1. The campaign includes snow samples collected during five years, but data from most locations have temporal extent of only a few months at most.

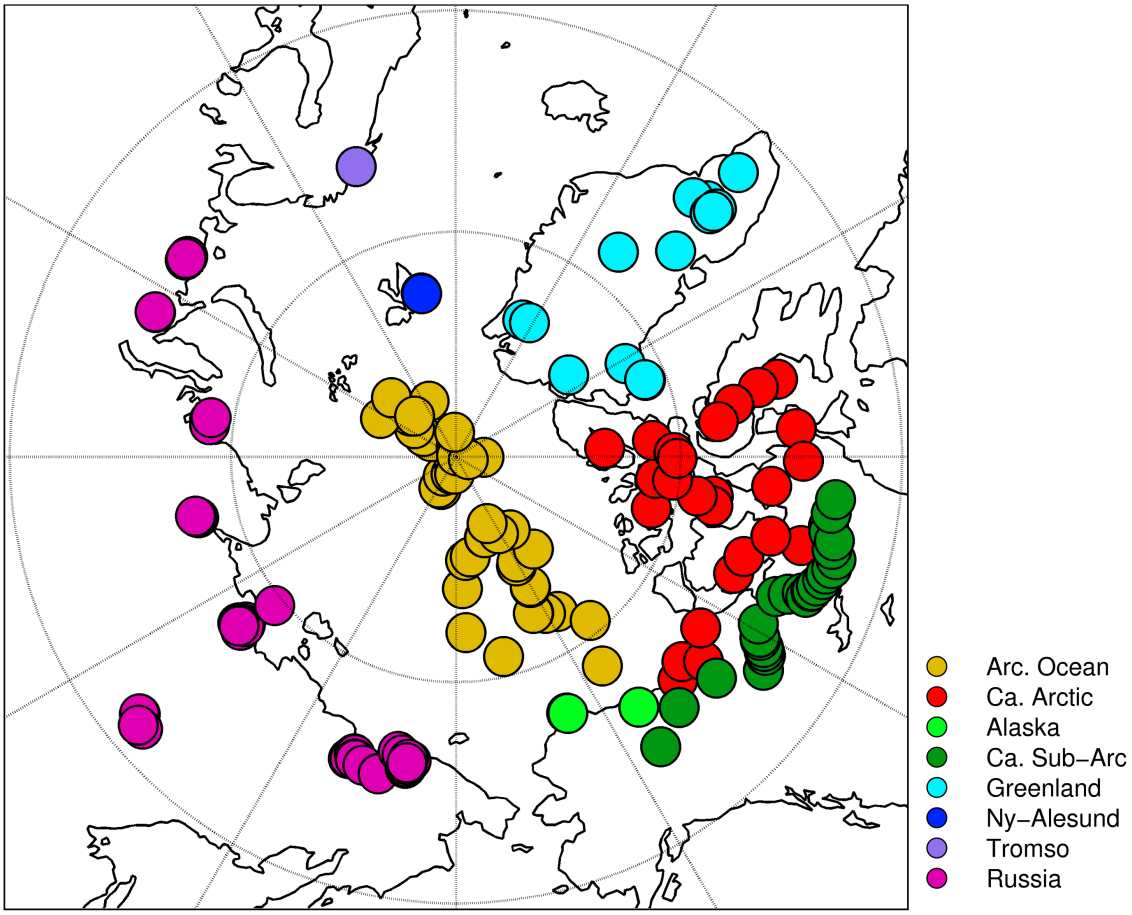

Figure 2.1: Locations of the BC-in-snow concentration measurements sampled by *Doherty et al.* (2010). The colors of the dots indicate different regions in the Arctic.

2.3 Methods

BC concentrations in land-based snow are simulated with CLM4 (e.g., *Lawrence et al.*, 2011), run at $1.9^\circ \times 2.5^\circ$ horizontal resolution. To simulate BC in snow on sea ice, we use the CICE4 model (e.g., *Holland et al.*, 2012). *Flanner et al.* (2007) and *Lawrence et al.* (2011) provide descriptions of the treatment of radiative transfer and aerosol processes in land snow, and sea-ice treatments are described by *Briegleb and Light* (2007) and *Holland et al.* (2012). Briefly, both model components apply two-stream, multi-layer, multi-spectral radiative transfer models, and both models simulate changes in vertical aerosol distributions arising from deposition, meltwater flushing, sublimation, and layer combinations and divisions. We drive both models with interannually varying atmospheric re-analysis data with a six hour time resolution from 2004–2009, during which the BC-in-snow measurements were conducted. CLM employs a blended re-analysis from the Climatic Research Unit (CRU) and National Centers for Environmental Prediction (NCEP), described at: http://dods.extra.cea.fr/data/p529viov/cruncep/readme.htm. We drive CICE with NCEP/NCAR reanalysis data (*Kistler et al.*, 1999). Model spin-up occurs during 2004 and the 2005–2009 period is used for the evaluation and analysis of radiative effect. We also conduct a sensitivity study using self-consistent meteorology and aerosol deposition fields at a high temporal resolution (Section 2.4.3).

We use data from 12 models contributing to the AeroCom Phase I intercomparison project (e.g., *Kinne et al.*, 2006; *Schulz et al.*, 2006; *Textor et al.*, 2006, 2007; *Koffi et al.*, 2012), and 13 models contributing to the more recent Phase II project (e.g., *Myhre et al.*, 2013; *Samset et al.*, 2013; *Stier et al.*, 2013). Table 2.1 summarizes the names and descriptions of these models. Each of these models has provided monthly gridded deposition fields of BC, partitioned into wet and dry components. Phase I simulations are conducted under the present-day "B" protocol (*Kinne et al.*, 2006), where all models adopt harmonized BC emissions fields, though possibly with slight

differences in the partitioning of emissions in vertical space and size distributions. Phase II simulations are conducted under the present-day "A2 Control" protocol (*Dentener et al.*, 2006; *Schulz et al.*, 2009), where each model employs its own emissions, leading to a wider diversity in model deposition fluxes, BC concentrations in snow, and BC-in-snow radiative effects.

We re-gridded all BC and dust deposition fields to $1.9^\circ \times 2.5^\circ$ resolution, and use monthly-resolved fields to drive the CLM and CICE models. CLM and CICE track vertically-resolved hydrophilic and hydrophobic species of BC, from which radiative effect is calculated. We assign all wet deposition to the hydrophilic species, and partition dry deposition into the two species based on monthly, gridded ratios obtained from a CAM4 aerosol simulation. This process results in slightly more than half of dry deposition being assigned to the hydrophilic species. One model (UIO-GCM in Phase I) did not contribute dust deposition fields to AeroCom. Because dust is also a light absorbing aerosol, the lack of dust contributes to a small positive bias in BC radiative effect diagnosed for this model, but does not influence the model–observation evaluation.

For each model contribution, we run CLM and CICE with two sets of BC meltwater scavenging coefficients. The BC meltwater scavenging coefficient is the ratio of BC concentration in the meltwater flux leaving a snow layer to the bulk concentration in that snow layer (*Flanner et al.*, 2007). The scenario with inefficient scavenging (IS) applies meltwater scavenging coefficients of 0.2 and 0.03 for hydrophilic and hydrophobic BC, respectively, as used by *Flanner et al.* (2007) and derived from field measurements (*Conway et al.*, 1996). The efficient scavenging (ES) scenario assumes meltwater scavenging efficiencies of 1.0 for both hydrophilic and hydrophobic BC, meaning each unit of meltwater that passes out of a snow layer carries an amount of BC exactly proportional to the BC mass concentration in that layer.

Because some samples were collected in the same site or in sites that are very close

Table 2.1: Phase I and Phase II AeroCom models used in this study.

Phase	Model Name	Resolution (lon×lat×lev)	Year of Available Deposition Field	References
I	DLR	$96 \times 48 \times 19$	-	*Ackermann et al.* (1998)
I	GISS	$72 \times 46 \times 20$	-	*Koch et al.* (2006); *Koch* (2001); *Bauer and Koch* (2005)
I	LOA	$96 \times 73 \times 19$	-	*Reddy and Boucher* (2004)
I	LSCE	$96 \times 73 \times 19$	-	*Szopa et al.* (2013)
I	MATCH	$192 \times 94 \times 28$	-	*Barth et al.* (2000); *Rasch et al.* (2000, 2001)
I	MPI-HAM	$192 \times 96 \times 31$	-	*Stier et al.* (2005)
I	TM5	$60 \times 45 \times 25$	-	*Krol et al.* (2005); *de Meij et al.* (2006)
I	UIO-CTM	$128 \times 64 \times 40$	-	*Grini et al.* (2002, 2005); *Myhre et al.* (2007); *Berglen et al.* (2004)
I	UIO-GCM	$128 \times 64 \times 18$	-	*Iversen and Seland* (2002); *Kirkevåg and Iversen* (2002)
I	UIO-GCM-V2	$128 \times 64 \times 26$	-	*Seland et al.* (2008)
I	ULAQ	$16 \times 19 \times 26$	-	*Pitari et al.* (2002, 2008)
I	UMI	$144 \times 91 \times 30$	-	*Liu and Penner* (2002)
II	CAM4-Oslo	$144 \times 96 \times 26$	9999	*Kirkevåg et al.* (2013)
II	CAM5.1	$144 \times 96 \times 30$	2006	*Liu et al.* (2012); *Ghan et al.* (2012)
II	GISS-MATRIX	$144 \times 90 \times 40$	2006-2008	*Bauer et al.* (2008, 2010)
II	GISS-ModelE	$144 \times 90 \times 40$	2004-2008	*Koch et al.* (2006, 2007); *Bauer et al.* (2007)
II	GLOMAP	$128 \times 64 \times 31$	2006	*Spracklen et al.* (2005, 2011)
II	GMI	$144 \times 91 \times 42$	2006	*Bian et al.* (2009)
II	HadGEM2	$192 \times 145 \times 38$	2006-2008	*Bellouin et al.* (2011)
II	ECHAM5-HAM2	$192 \times 96 \times 31$	2006,2008	*Stier et al.* (2005); *Zhang et al.* (2012)
II	OsloCTM2	$128 \times 64 \times 60$	2006	*Myhre et al.* (2009); *Skeie et al.* (2011b,a)
II	SPRINTARS	$320 \times 160 \times 56$	2006	*Takemura et al.* (2005, 2009)
II	TM5	$120 \times 90 \times 34$	2006	*Vignati et al.* (2010); *Aan de Brugh et al.* (2011); *von Hardenberg et al.* (2012)
II	IMPACT	$144 \times 91 \times 30$	9999	*Yun and Penner* (2012)
II	GOCART	$144 \times 91 \times 30$	2006	*Chin et al.* (2009)

Year "9999" indicates the deposition fields are generated from generic present-day meteorological conditions

to each other, multiple measurements taken at similar times and depths can reside within the same grid cell and snow layer(s) represented by the model. This could be problematic for the calculation of mean and median BC concentrations, since the grid cells containing more observations would receive more weight. Thus if two or more observations are collected at the same year, month and depth and are within the same grid cell in the model, we first average them and then treat them as one for the model comparison. Measurements collected in 1998 for the SHEBA campaign are not used in this exercise. Six measurements align with model grid cells that do not have any snow during the month of measurement, and are discarded from the analysis. After the merge and elimination, there are 485 unique observations in 8 regions. The following analysis is based on this merged sample set.

Data from *Doherty et al.* (2010) include most top and bottom depths from which the snow samples were taken, and we use this information to determine the appropriate model snow layer(s) to compare with. CLM uses up to 5 snow layers, depending on total snow thickness, and we weight the BC concentration from each snow layer based on its fractional overlap with the measurement. If the sample only spans a fraction of the snow layer thickness, we use this fraction multiplied by the snow mass in the layer as the weight for that layer. If the model layer is completely contained within the measurement boundaries, we use the total snow mass as the weight for that layer. Finally the BC-in-snow concentrations from the available layers are averaged by the snow mass weights (normalized to 1) to get the model simulated BC concentrations for depths matching the position of the observation. Due to the short spin-up time (1 year), BC concentrations in the deepest snow layer did not always reach equilibrium, especially in regions of perennial snow cover and low accumulation like Greenland. Thus we only use the top 4 layers for the comparison. The CICE model applies 2 snow layers overlying 4 sea ice layers. The depth of the surface snow layer changes with the total snow thickness, equaling half of the total thickness when

snow depth is less than or equal to 8 cm, and equaling 4 cm when the total snow depth is greater than 8 cm. For the observations sampled over sea ice, we use the top and bottom depth of the sample to determine which snow layer on sea ice should be compared with. If the sample extends to both layers, we use the averaged BC concentration from both layers to compare with the observation.

2.4 Results and Discussion

2.4.1 Comparison of Models and Observations

Figure 2.2 shows BC-in-snow concentrations from models and observations. The spatial and temporal mean observed BC concentration averaged over all samples is 19.2 ng g^{-1}. The 75% quartile of the observations is close to the mean value, due to skewness caused by high BC concentrations in some parts of Russia. Each color symbol in the figure represents the mean BC concentration of a model simulation averaged over the locations (grid cell and layer) and months matching the observations. With inefficient melt scavenging (IS), the multi-model mean concentration over the observational domain is 14.8 ng g^{-1} for the twelve Phase I simulations and 23.3 ng g^{-1}for the thirteen Phase II models. With efficient scavenging (ES), the Phase I and Phase II multi-model means are 14.0 and 22.3 ng g^{-1}, respectively. The relatively small decrease associated with ES is discussed more in Section 2.4.4. There is a factor of 5 spread between the highest and lowest Phase I model means, and a 6.5-fold spread among Phase II models. The normalized standard deviation of model means is 0.41 and 0.40 for Phase I and Phase II IS runs, respectively. The inter-model variation in bias is also large for both Phase I and Phase II models (Table 2.2).

Three general factors could lead to the large inter-model diversity. Firstly, the transport schemes and meteorology vary between models. A large portion of the aerosol burden in the Arctic is transported from mid and lower latitudes (*Koch and*

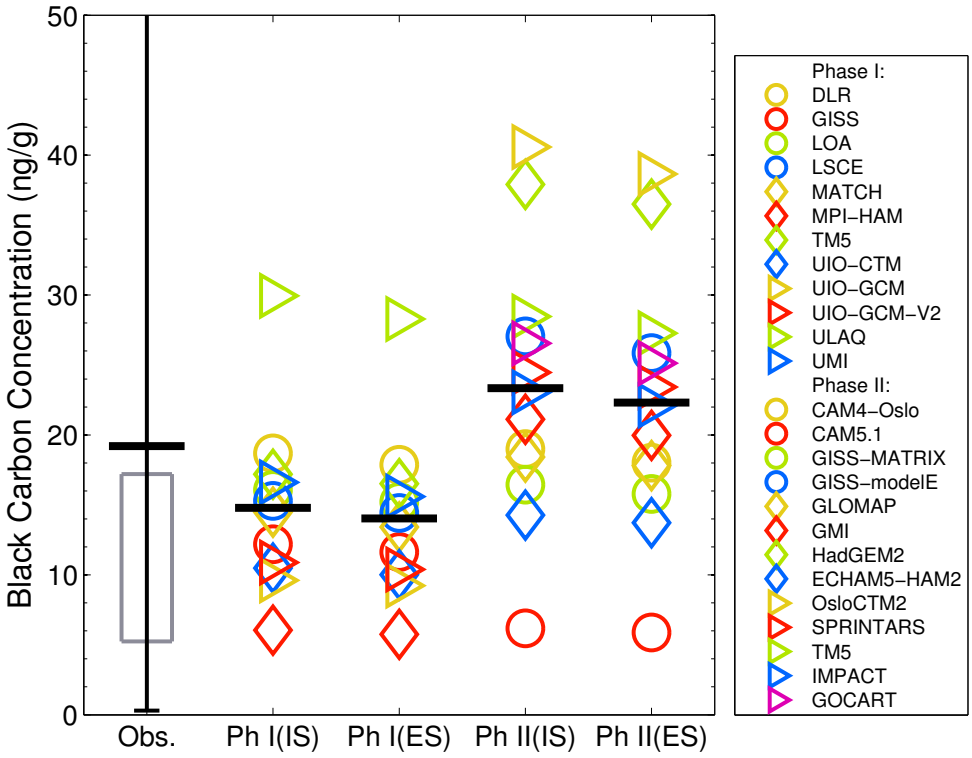

Figure 2.2: Observed and modeled black carbon (BC) in snow concentrations in the Arctic. From left to right are observed BC-in-snow concentrations from *Doherty et al.* (2010), simulated concentrations over the observational domain from AeroCom Phase I models with inefficient meltwater scavenging (Ph I(IS)) and efficient scavenging (Ph I(ES)), and simulated concentrations from Phase II models with inefficient scavenging (Ph II(IS)) and efficient scavenging (Ph II(ES)). The gray box indicates the 25% and 75% quartiles of the observations, and the whisker depicts the full extent of the observations. Note that the maximum value of $783.5\,\mathrm{ng\,g^{-1}}$ is outside the figure. The bold horizontal line shows the mean of the observations and models for each scenario. Each colored dot represents the mean of a particular model's simulated BC-in-snow concentration averaged over grid cells matching the location, time, and depth of measurements.

Table 2.2: Statistics of the comparison between models and observations. The correlation coefficients and significance levels are calculated by a linear regression fitted to all pairs of observations and corresponding modeled values from the same time and location. Biases are the differences between the mean of modeled values and the mean of observations. The mean observed BC-in-snow concentration is 19.2 $\mathrm{ng\,g^{-1}}$.

Phase	Model	Correlation Coefficient	Bias ($\mathrm{ng\,g^{-1}}$)	Correlation Coefficient	Bias ($\mathrm{ng\,g^{-1}}$)
		(inefficient scavenging)		(efficient scavenging)	
I	DLR	0.21*	-0.5	0.20*	-1.3
I	GISS	0.15*	-7.0	0.14*	-7.6
I	LOA	0.15*	-3.1	0.14*	-4.0
I	LSCE	0.16*	-3.9	0.15*	-4.8
I	MATCH	0.11*	-4.7	0.12*	-5.8
I	MPI-HAM	0.22*	-13.2	0.21*	-13.4
I	TM5	0.28*	-2.0	0.27*	-2.7
I	UIO-CTM	0.28*	-8.7	0.27*	-9.2
I	UIO-GCM	0.15*	-9.6	0.14*	-10.0
I	UIO-GCM-V2	0.14*	-8.3	0.13*	-8.8
I	ULAQ	0.14*	+10.7	0.14*	+9.1
I	UMI	0.21*	-2.6	0.21*	-3.6
Phase I Mean		-	**-4.4**	-	**-5.2**
II	CAM4-Oslo	0.12*	-0.2	0.12*	-1.2
II	CAM5.1	0.23*	-13.0	0.22*	-13.3
II	GISS-MATRIX	0.21*	-2.8	0.21*	-3.4
II	GISS-modelE	0.21*	+7.8	0.20*	+6.7
II	GLOMAP	0.05	-0.8	0.04	-1.4
II	GMI	0.10*	+1.9	0.10*	+0.8
II	HadGEM2	0.18*	+18.7	0.18*	+17.3
II	ECHAM5-HAM2	0.18*	-4.9	0.17*	-5.5
II	OsloCTM2	0.10*	+21.4	0.09*	+19.5
II	SPRINTARS	0.06	+5.3	0.06	+4.2
II	TM5	0.14*	+9.3	0.14*	+8.1
II	IMPACT	0.18*	+3.8	0.17*	+2.9
II	GOCART	0.04	+7.3	0.03	+5.9
Phase II Mean		-	**+4.1**	-	**+3.1**

* indicates the regression is significant at $\alpha = 0.05$ level.

Hansen, 2005), amplifying the effects of differences in model transport and removal physics. There are several pathways for pollutant transport to the Arctic, each with seasonality governed by scavenging efficiency and features of the Arctic dome. *Stohl* (2006) found that Arctic pollution originating from North America and Asia generally experiences uplift outside the Arctic and then descent into the Arctic. Pollution from Europe travels to the Arctic by low-level transport followed by ascent in the Arctic or low-level transport alone. Secondly, the characteristics of aerosol deposition processes vary considerably between models. Deposition fluxes are influenced by dry and wet removal representations, model precipitation, aerosol aging and mixing, and aerosol–cloud interactions. Among Phase I models, the normalized standard deviation for Arctic BC deposition flux is 0.22 while for Phase II models it is 0.27, indicating larger inter-model diversity for Phase II contributions. Some of the increased spread in Phase II BC deposition originates from use of different emission inventories, the third factor contributing to inter-model diversity.

Scatter plots shown in Figures 2.3 and 2.4 compare simulated and observed BC concentrations in different regions. In general, observations and models are more likely to agree with each other in the Arctic Ocean and Ny-Ålesund. Models tend to overestimate BC-in-snow concentrations in the Canadian Arctic, Alaska, Canadian Sub-Arctic and Greenland. In the Canadian Arctic, Canadian Sub-Arctic and Greenland, the means of Phase I models are generally within a factor of 3 higher than the means of the observations, while the means of Phase II models are about a factor of 3–4 higher. In those three regions, the biases are positive for most of the models, although several models simulate BC concentrations relatively close to the observations. In Alaska, the model–observation disagreement is more substantial. The mean observed BC concentration in this region is about $12\,\mathrm{ng\,g^{-1}}$, while the highest value among all models is nearly $170\,\mathrm{ng\,g^{-1}}$, and the mean Phase I and Phase II concentrations are $50\,\mathrm{ng\,g^{-1}}$ and $90\,\mathrm{ng\,g^{-1}}$, respectively. These model values are higher than

those of other regions (Figures 2.3 and 2.4). Importantly, however, there are only 3 measurement samples in the Alaska region, all showing less than $20\,\mathrm{ng\,g^{-1}}$, potentially biasing the evaluation for this region. The multi-model mean concentration of BC in surface snow, averaged annually over all of Alaska, is $41\,\mathrm{ng\,g^{-1}}$, smaller than averages over the Alaskan sampling domain. In Tromsø and Russia, models tend to underestimate BC-in-snow concentrations over the observational domain. The mean for Phase I models is around half the observational mean. The Phase II mean is closer to the observations, though these models show more inter-model diversity in these regions than Phase I models. One potential factor that could contribute to the underestimation of BC-in-snow concentration in Russia is the omission of high-latitude flaring source in the AeroCom emission inventories (*Stohl et al.*, 2013).

From Figures 2.3 and 2.4, we see that the models capture some spatial characteristics of the observed BC-in-snow concentrations, though correlations between the observations and models are weak. This indicates that the current stage of global aerosol models has difficulty in reproducing the observed distribution of BC in Arctic snow, caused by some combination of biased emission inventories, atmospheric and/or snow aerosol parametrizations, or inconsistent meteorology from that which prevailed during the measurement campaign. Table 2.2 shows the correlation coefficient (R), statistical significance (i.e. p-value smaller than 0.05), and bias between the models and observations. The correlation coefficients are generally small, ranging from 0.11 to 0.28 in Phase I IS simulations and 0.12 to 0.27 in ES simulations. In Phase II, the correlation coefficients range from 0.04 to 0.23 and 0.03 to 0.22, respectively, in IS and ES simulations. Despite poor correlation coefficients, mean model biases are reasonably small. Phase I models generally slightly underestimate observed Arctic BC-in-snow concentrations (Table 2.2). This is consistent with results from *Koch et al.* (2009b) showing that most AeroCom Phase I models underestimate the atmospheric concentration of BC compared with observations in the remote Arctic, and

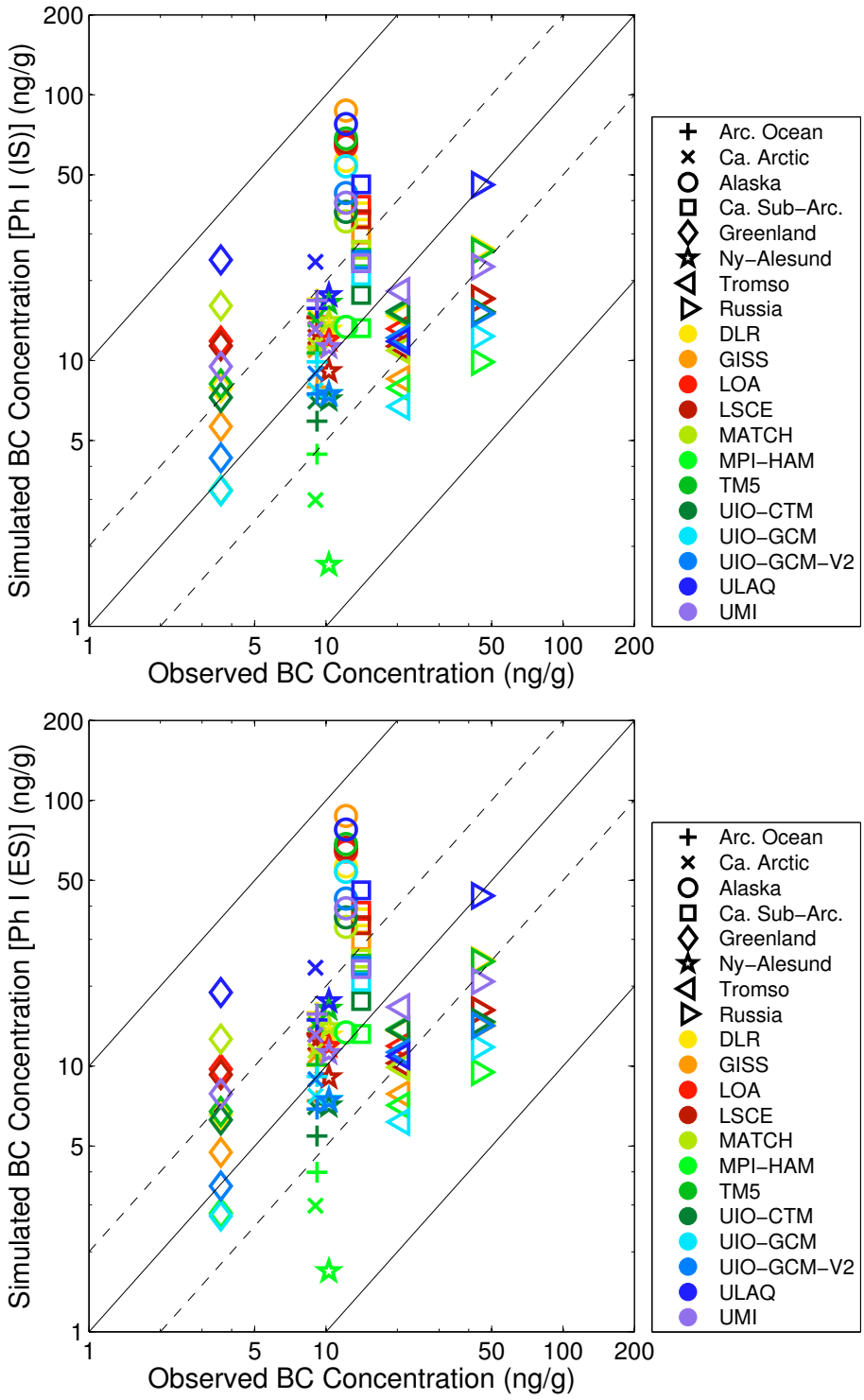

Figure 2.3: Log-scale scatter plot of BC-in-snow concentrations simulated in different regions with Phase I models applying inefficient meltwater scavenging (upper panel) and efficient scavenging (lower panel), compared with observations. The mean values for each region are averaged over grid cells matching the location, time, and depth of measurements.

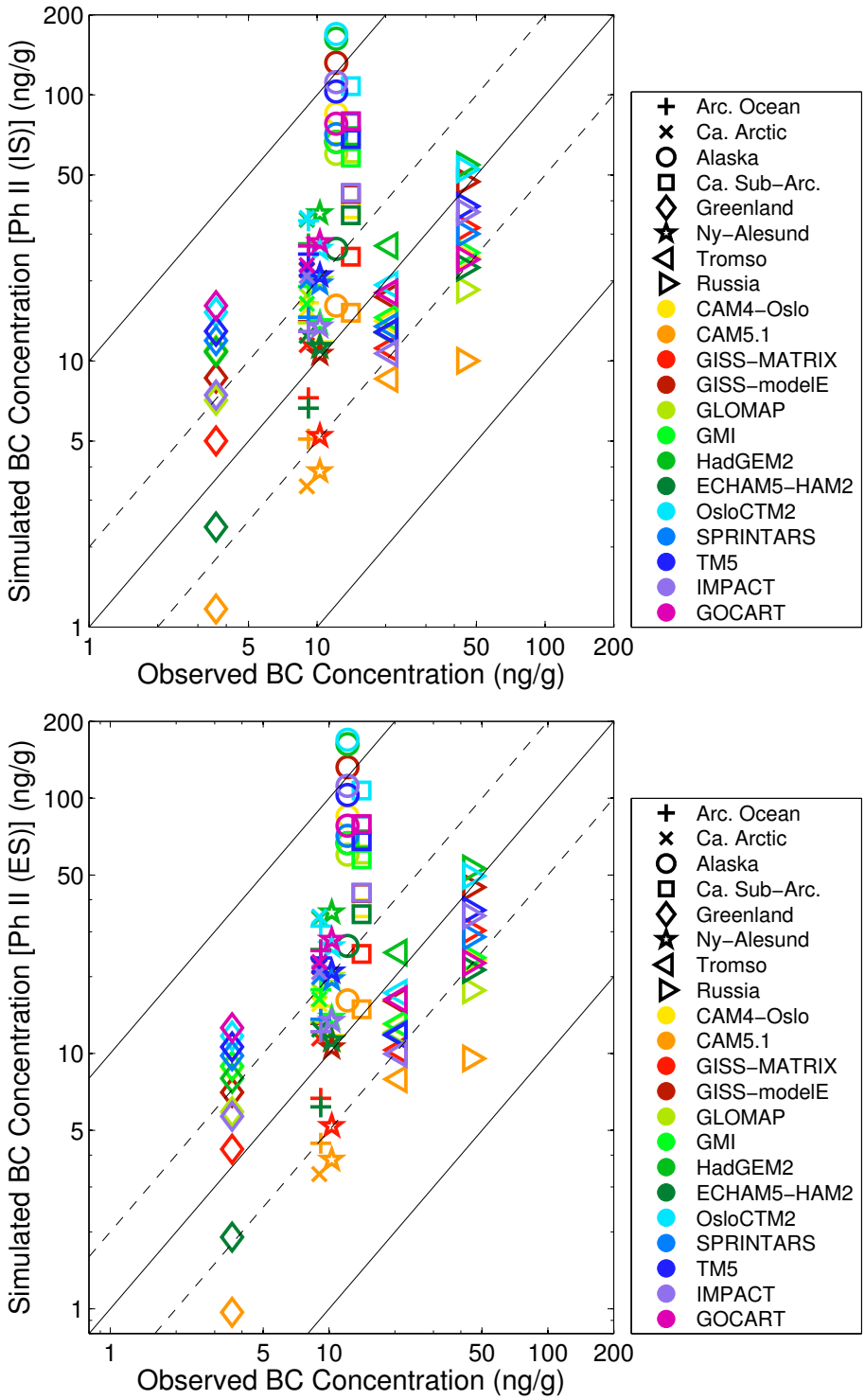

Figure 2.4: Same as Figure 2.3, but for Phase II models.

also with *Shindell et al.* (2008), who showed that HTAP models also generally underestimate near-surface measurements of BC at Barrow and Alert. Five of the Phase II models are biased low while the other eight overestimate BC-in-snow concentrations. With inefficient scavenging, the biases range from $-13.2\,\mathrm{ng\,g^{-1}}$ to $+10.7\,\mathrm{ng\,g^{-1}}$ for Phase I models. For Phase II, the lowest and highest mean biases are $-13.0\,\mathrm{ng\,g^{-1}}$ and $+21.4\,\mathrm{ng\,g^{-1}}$.

We have so far reported results for both inefficient (IS) and efficient (ES) melt scavenging parameters. The IS parameters are derived from a very limited set of observations, while the ES studies are idealized and designed to test the sensitivity of results to this parameter. Although there is large uncertainty in melt scavenging efficiency, a growing number of observational studies indicate that BC is scavenged inefficiently with melt water (*Xu et al.*, 2012; *Doherty et al.*, 2013; *Sterle et al.*, 2013). From field measurements, *Doherty et al.* (2013) derived BC meltwater scavenging efficiencies ranging from 10% to 30%, broadly consistent with the parameters used by *Flanner et al.* (2007). We also find that 16 of 25 AeroCom simulations produce a higher correlation coefficient with IS than ES (though the mean improvement is only 0.01). Consequently, the analysis that follows focuses on IS simulations, except for a sensitivity analysis of melt scavenging in Section 2.4.4.

The observations cover a large area of the Arctic but are relatively sparse in some sectors. Also, the measurements were conducted only during spring and summer, the seasons of most relevance for radiative effects. Thus a question arises of how well the sampling domain represents the Arctic-mean distribution of BC in surface snow. Figure 2.5a shows, for each model, the annual mean BC concentration in the surface snow layer averaged over the whole Arctic plotted against the annual mean surface-layer BC concentration averaged spatially and temporally over the model domain matching observations. There is a strong linear relationship between these two quantities. The R^2 of the linear fit is 0.73 and statistically significant at the

0.001 level. Figure 2.5b plots BC concentrations weighted by the surface incident solar radiation (ISR) and averaged over the whole Arctic against the same quantity on the x-axis as Figure 2.5a. This metric places a stronger weight on polluted snow exposed to intense sunlight, which exerts a stronger radiative effect than the same snow surface in polar darkness. It thus gives a better indication of how representative the measurement survey is of the Arctic BC-in-snow radiative effect. The linear relationship in Figure 2.5b is stronger, with a R^2 value of 0.80. This result suggests that the sampling domain surveyed by *Doherty et al.* (2010), conducted during seasons of relatively strong insolation, could provide a reasonable constraint on Arctic-wide annual-mean radiative effects from BC-in-snow. The correlation between annual-mean BC concentrations at each of the measurement sites (a proxy for a scenario with year-round sampling) and Arctic-mean BC-in-snow concentrations is very high ($R^2 = 0.95$; not shown).

2.4.2 Emissions

Phase I models apply the same emission inventory, while Phase II models use different inventories. Figure 2.6 shows the zonal-mean emissions used in each model, plotted globally and for the northern high-latitudes. From Figure 2.6 and Table 2.3 we see that Phase II models show substantial variations in emissions, especially in the tropics, where biomass burning emissions are large and more variable between inventories. The peak emission fluxes are mostly within 30–40°N, which includes major populated industrial regions (East Asia, South Asia, parts of North America and Europe). Figure 2.6b shows that the inter-model variation in BC emissions at high latitudes is relatively small, and that emissions north of 70°N are negligible in the inventories applied.

To identify the importance of inter-model variability in local emissions, we regress annual mean Arctic (60–90°N) surface BC-in-snow concentrations against annual-

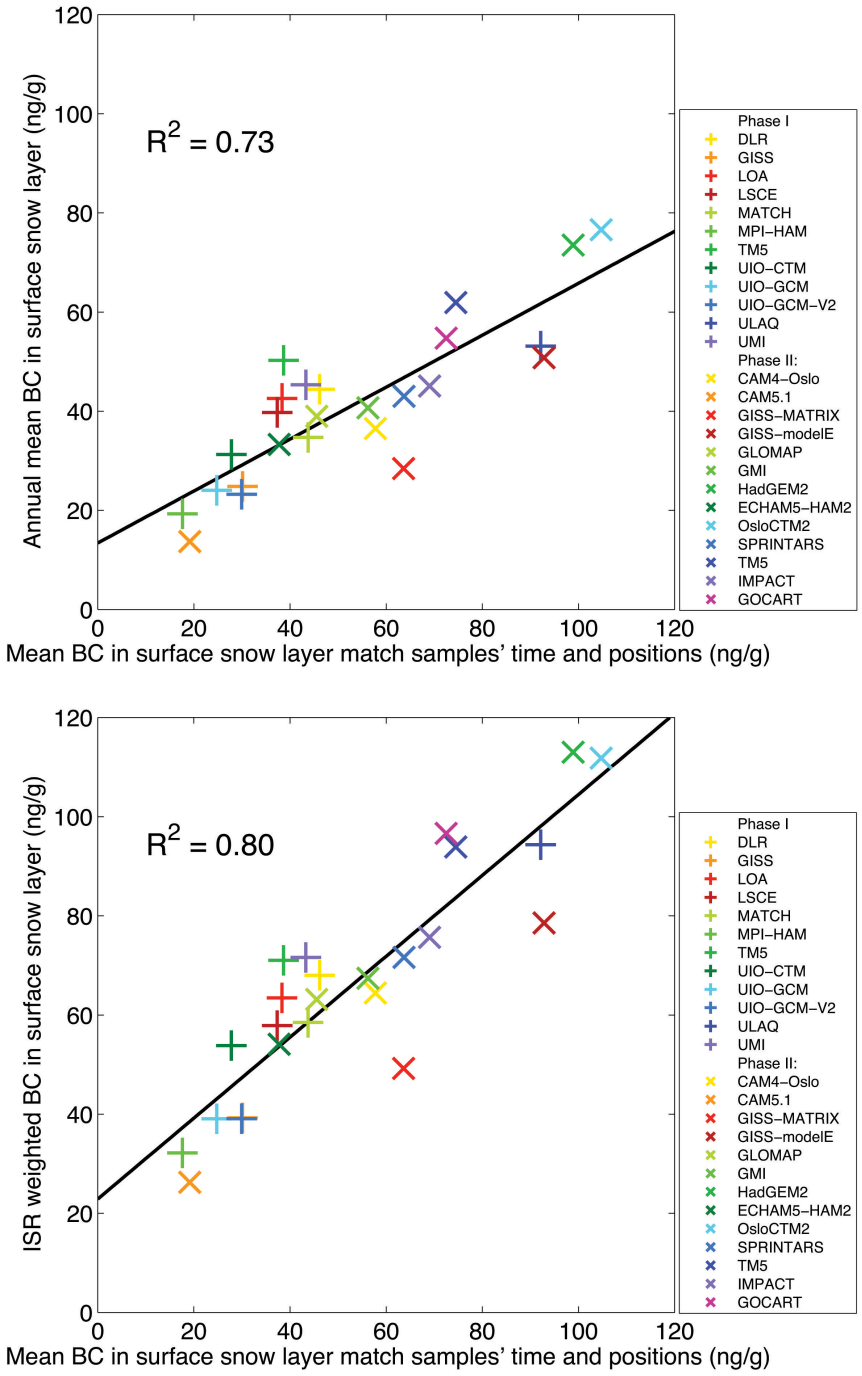

Figure 2.5: Relationships between simulated BC-in-snow concentrations averaged over the locations and months of observations and over the whole Arctic region. The abscissa is the surface layer BC-in-snow concentration averaged over grid cells matching the location and time of measurements. The ordinate is the annual mean surface layer BC-in-snow concentration averaged over the whole Arctic region (60°N to 90°N) (upper panel: Figure 2.5a), and averaged over the Arctic with insolation weighting (lower panel: Figure 2.5b).

mean emission fluxes, but find insignificant correlations both with the fluxes averaged over the Arctic (60–90°N) ($R^2 = 0.03$, $p = 0.55$) and with emission fluxes averaged in a larger region (50–90°N) ($R^2 = 0.09$,$p = 0.29$). Among Phase II models, the ratio between annual mean Arctic deposition and Arctic emission ranges from 2.1 to 6.1, with 10 models having a ratio larger than 3. For Phase I models, the ratio ranges from 1.6 to 3.3. This proves, as expected, that most of the model BC depositing in the Arctic originates from emissions outside the Arctic. The large range of this ratio reveals potential large inter-model vertical variability in aerosol scavenging efficiency as well as in transport efficiency to the Arctic. Variability in mid- and low-latitude emissions contributes to some of the diversity in Arctic deposition of Phase II models, but is entwined with the effects of variation in model transport and scavenging mechanisms.

2.4.3 Inter-model Deposition Variability

Inter-model variability in BC deposition, the primary direct driver of variation in BC-in-snow concentrations, originates from different emissions and model physics. Figure 2.7 shows annual zonal-mean BC deposition for Phase I (left) and Phase II (right) models, and indicates that the inter-model variation is generally larger in Phase II models, including at northern high latitudes. The peak deposition fluxes are near the equator and 30–40°N, owing to large emissions sources at these latitudes and efficient removal from ITCZ and monsoon precipitation. Spatial distributions of annual mean BC deposition over 50–90°N are shown in Figures 2.8 and 2.9. These figures show similar patterns among the models, with relatively large deposition over Northern Europe, North America and East Asia, and small deposition on Greenland and the Arctic Ocean. Though the spatial patterns are consistent among these models, the relative magnitudes are different. The Phase II HadGEM2 and OsloCTM2 models, in particular, show large BC deposition fluxes in the Arctic. The strong lin-

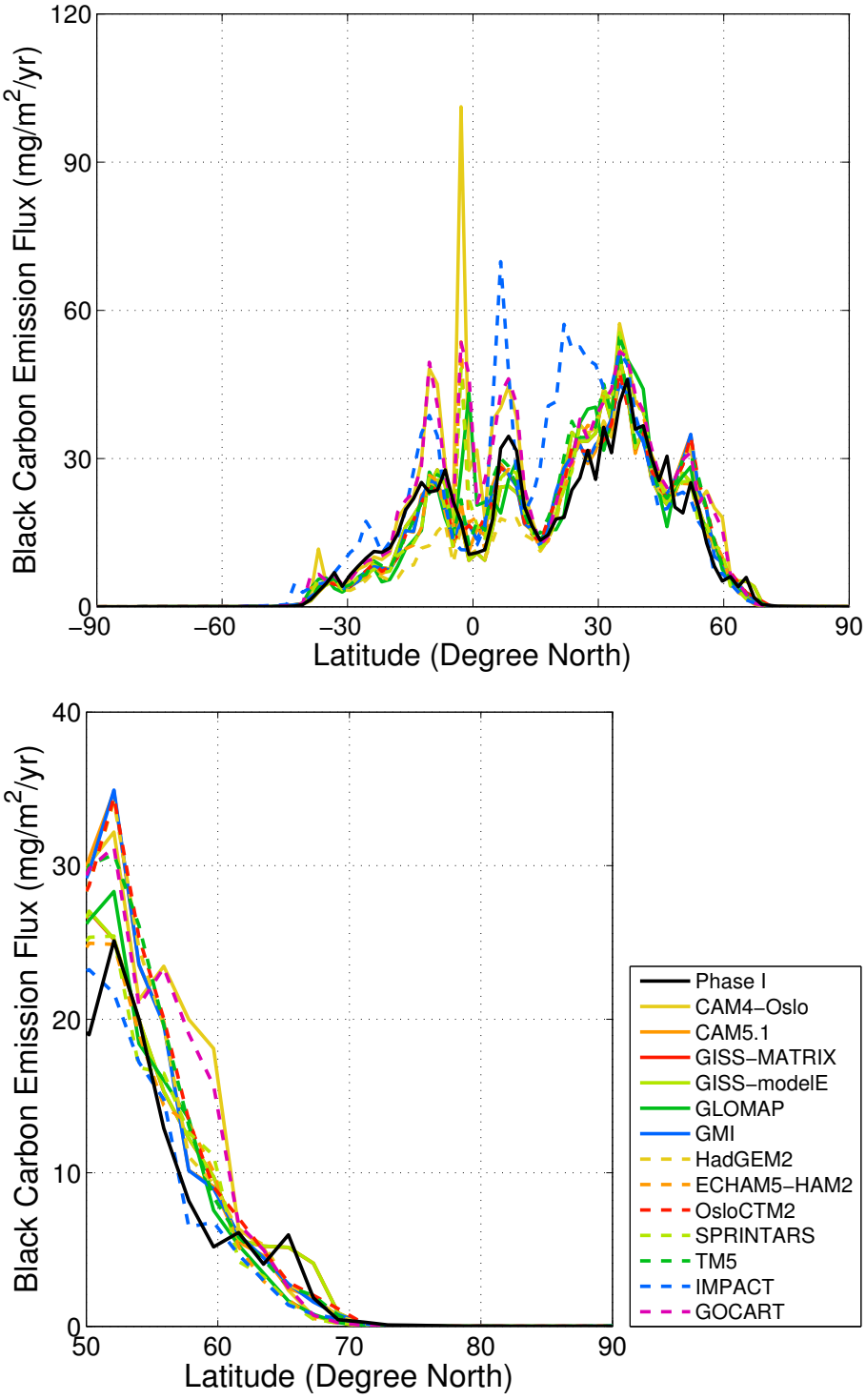

Figure 2.6: Annual, zonal-mean black carbon emission fluxes applied in Phase I and Phase II models for the global (upper panel: Figure 2.6a) and in more detail in the northern latitude regions (lower panel: Figure 2.6b).

Table 2.3: Annual mean BC emission and deposition fluxes for the globe and Arctic (60°N to 90°N).

Phase	Model	Global Emission Rate ($\mathrm{Tg\,yr^{-1}}$)	Arctic Emission Rate ($10^7\,\mathrm{kg\,yr^{-1}}$)	Arctic Deposition Rate ($10^7\,\mathrm{kg\,yr^{-1}}$)
I	DLR	7.77	6.93	22.04
I	GISS	*	*	10.84
I	LOA	*	*	22.47
I	LSCE	*	*	20.22
I	MATCH	*	*	21.19
I	MPI-HAM	*	*	14.07
I	TM5	*	*	19.95
I	UIO-CTM	*	*	18.27
I	UIO-GCM	*	*	13.88
I	UIO-GCM-V2	*	*	14.95
I	ULAQ	*	*	22.65
I	UMI	*	*	20.29
II	CAM4-Oslo	10.62	5.61	21.45
II	CAM5.1	7.76	5.64	13.19
II	GISS-MATRIX	7.58	7.67	16.20
II	GISS-modelE	7.59	7.68	22.05
II	GLOMAP	8.13	4.34	19.46
II	GMI	7.76	5.86	20.04
II	HadGEM2	6.63	6.33	34.45
II	ECHAM5-HAM2	8.11	4.05	19.49
II	OsloCTM2	7.80	6.77	28.19
II	SPRINTARS	8.12	3.71	22.45
II	TM5	8.22	5.78	25.54
II	IMPACT	10.55	3.94	16.13
II	GOCART	10.34	5.76	28.83

*The total amounts of BC emission are the same for Phase I models.

ear relationship ($R^2 = 0.80$, $p < 0.001$) between BC deposition fluxes averaged over 60–90°N and surface layer BC-in-snow concentration averaged over the same region demonstrates the first-order importance of regional deposition fluxes.

The normalized standard deviation of Arctic deposition is 0.22 for Phase I and 0.27 for Phase II models. While there is no inter-model variation of emissions (in terms of total emitted mass) for Phase I models, the normalized standard deviation of Phase II Arctic emissions is 0.23. Together, these results imply that aerosol transport, evolution, and removal processes (combined) are more important contributors to inter-model variation in Arctic BC deposition than emissions. This is also consistent with previous AeroCom analyses showing large variability in model aerosol burdens with harmonized emissions (*Textor et al.*, 2007).

The seasonal cycle of BC deposition can be important for Arctic BC-in-snow radiative effects. Forcing only occurs during the sunlit period, but BC deposited during winter can become exposed at the surface during spring and summer melt. Figure 2.10 shows the monthly mean BC deposition fluxes averaged over 60–90°N for Phase I and Phase II models. The Arctic BC deposition fluxes are relatively low during winter, when precipitation rates are low and the atmosphere is stably stratified. Deposition starts to increase after March and models generally show a sharp peak between June and August. Among Phase I models, one shows Arctic BC deposition peaking in June, seven peak in July, and four in August. Among Phase II models, one peaks in May, nine peak in July, one in August and two in September. The seasonal cycles of deposition among Phase I models are broadly similar. Most Phase II models follow similar seasonal patterns as Phase I, though some models peak later. For some models, the contrast between summer and winter is high, while for others it is not. For example, the Arctic deposition flux in July is at least a factor of 3 higher than that in the lowest month for Phase II CAM4-Oslo and HadGEM2 models, while seasonal variation is very small in the GMI and IMPACT models. This diversity

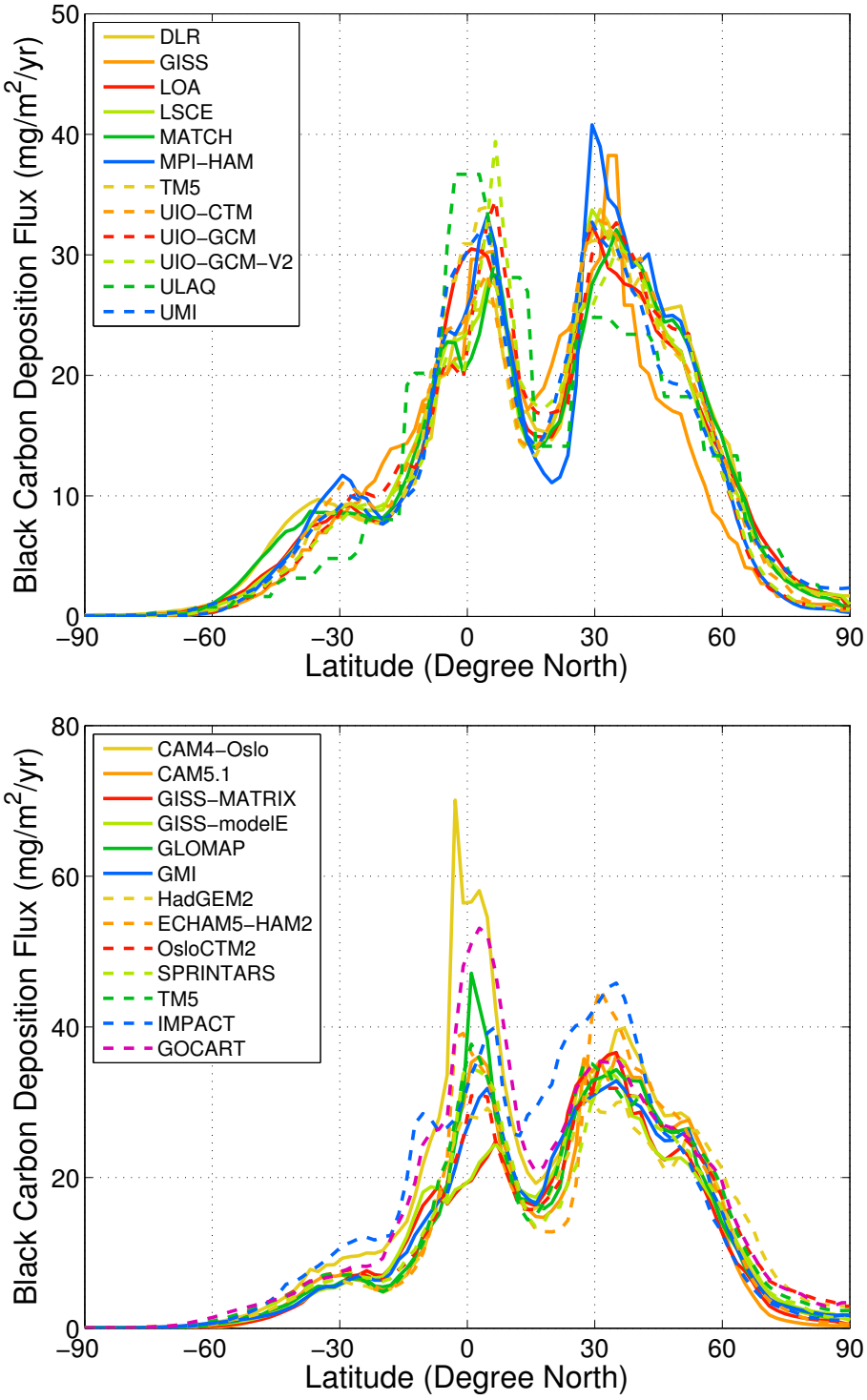

Figure 2.7: Annual, zonal-mean black carbon deposition fluxes for Phase I (upper panel: Figure 2.7a) and Phase II (lower panel: Figure 2.7b) models. (Note the scale on ordinate is different for the two plots.)

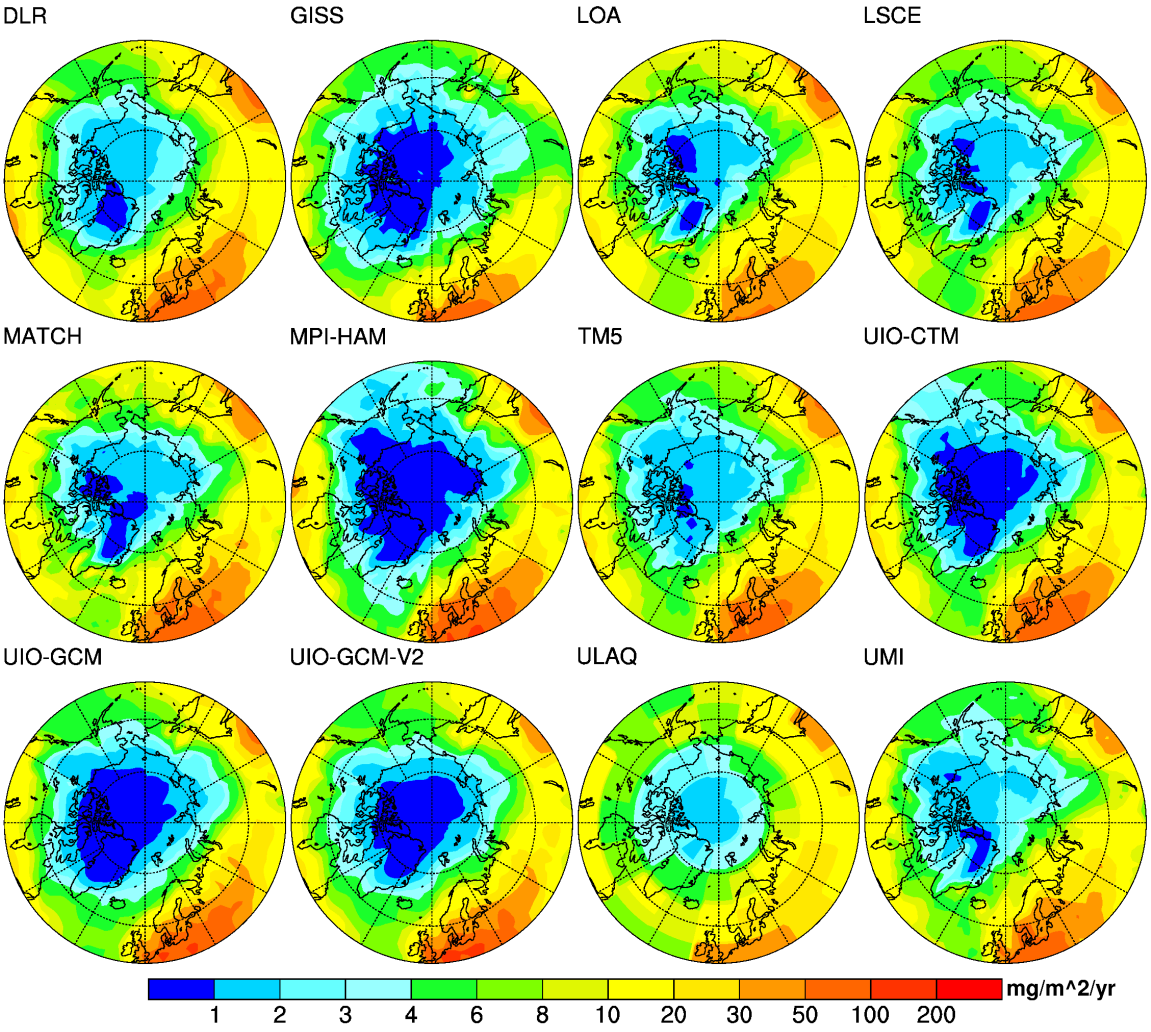

Figure 2.8: Annual mean black carbon deposition fluxes for Phase I models, plotted from 50°N to 90°N.

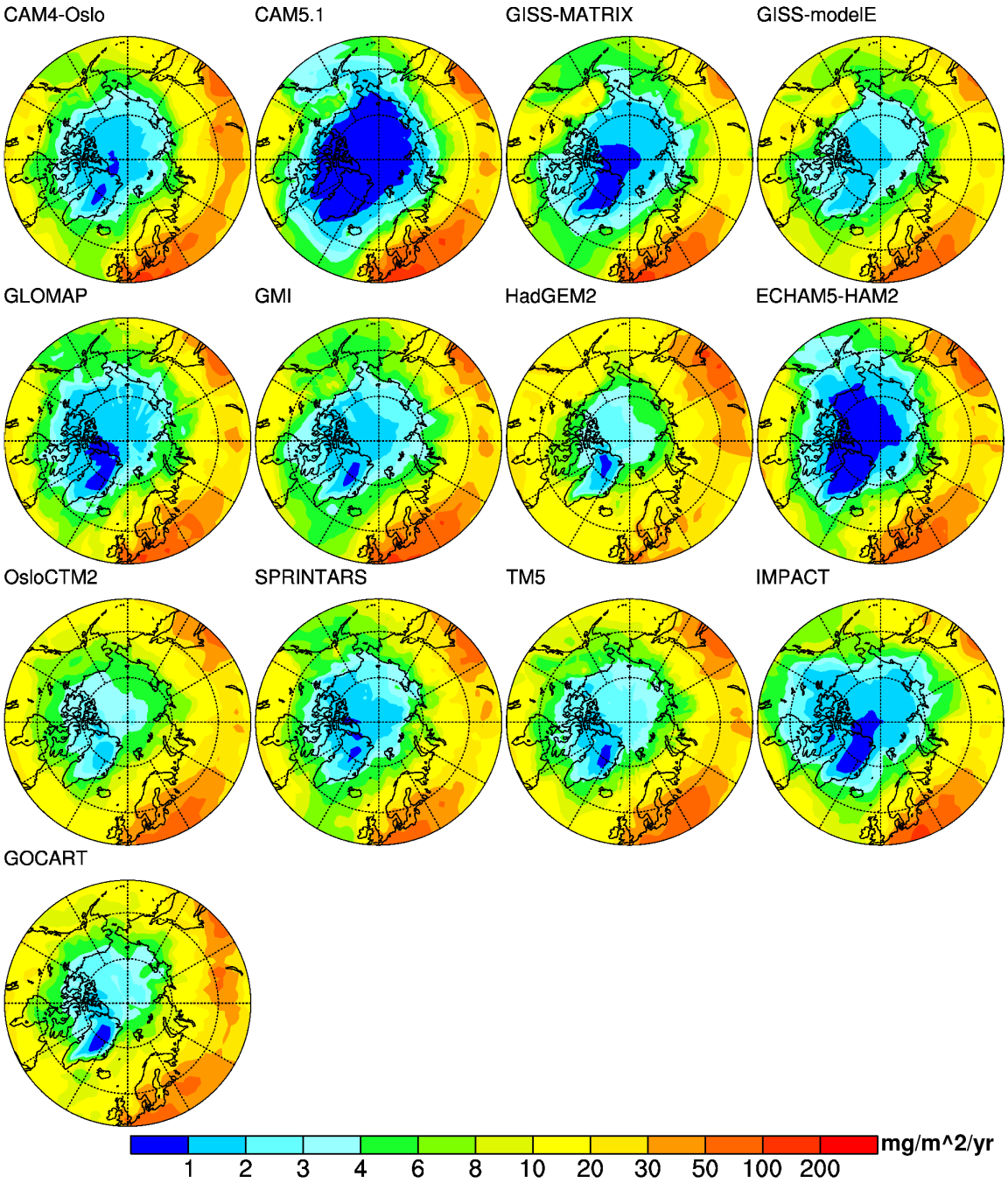

Figure 2.9: Annual mean black carbon deposition fluxes for Phase II models, plotted from 50°N to 90°N.

originates both from different emission inventories and different chemical and physical parametrizations. Most AeroCom models do not have seasonality for fossil fuel and biofuel emissions. In reality, however, high-latitude biofuel and fossil fuel emission sources tend to be stronger in winter, indicating a potential bias in seasonality of deposition fluxes simulated with seasonally-constant emission inventories.

Dividing the Arctic BC column burden by the Arctic deposition flux provides a proxy for Arctic BC residence time. This is imperfect because BC passing through the Arctic atmosphere will contribute to mean burden but not deposition. Nonetheless, the averages are taken over a sufficiently large area that they should approximate actual Arctic residence time. Here for simplification, we will call this term "Arctic residence time" despite its potential bias. The Arctic residence time is an indicator of how effectively BC in the Arctic atmosphere deposits through wet and dry processes. *Textor et al.* (2006) reported that global BC atmospheric residence times for Phase I models ranges from 5.2 to 15.0 days. Figure 2.11 shows the global and Arctic atmospheric residence times of BC in Phase II models. The global BC residence time ranges from 3.9 to 11.9 days while the Arctic residence time ranges from 3.7 to 23.2 days. The Arctic residence time is longer on average by 4.0 days (median of 2.5 days) than the global residence time, although three models show shorter Arctic than global residence times. Causes for high Arctic residence times include low precipitation rates (especially during polar winter), stable stratification that limits dry turbulent deposition, and long residence time of air parcels that become trapped within the polar dome. *Koch et al.* (2009b) evaluated Arctic atmospheric BC in AeroCom Phase I models, and found that increasing BC lifetime, which is accomplished by decreasing the aging rate or by reducing removal by ice clouds, has a large impact on BC surface concentrations in remote regions. Analysis of surface measurements at Barrow, Alaska indicates that the seasonal cycle of "Arctic Haze" is dominated by wet scavenging, rather than efficiency of transport pathways from source regions

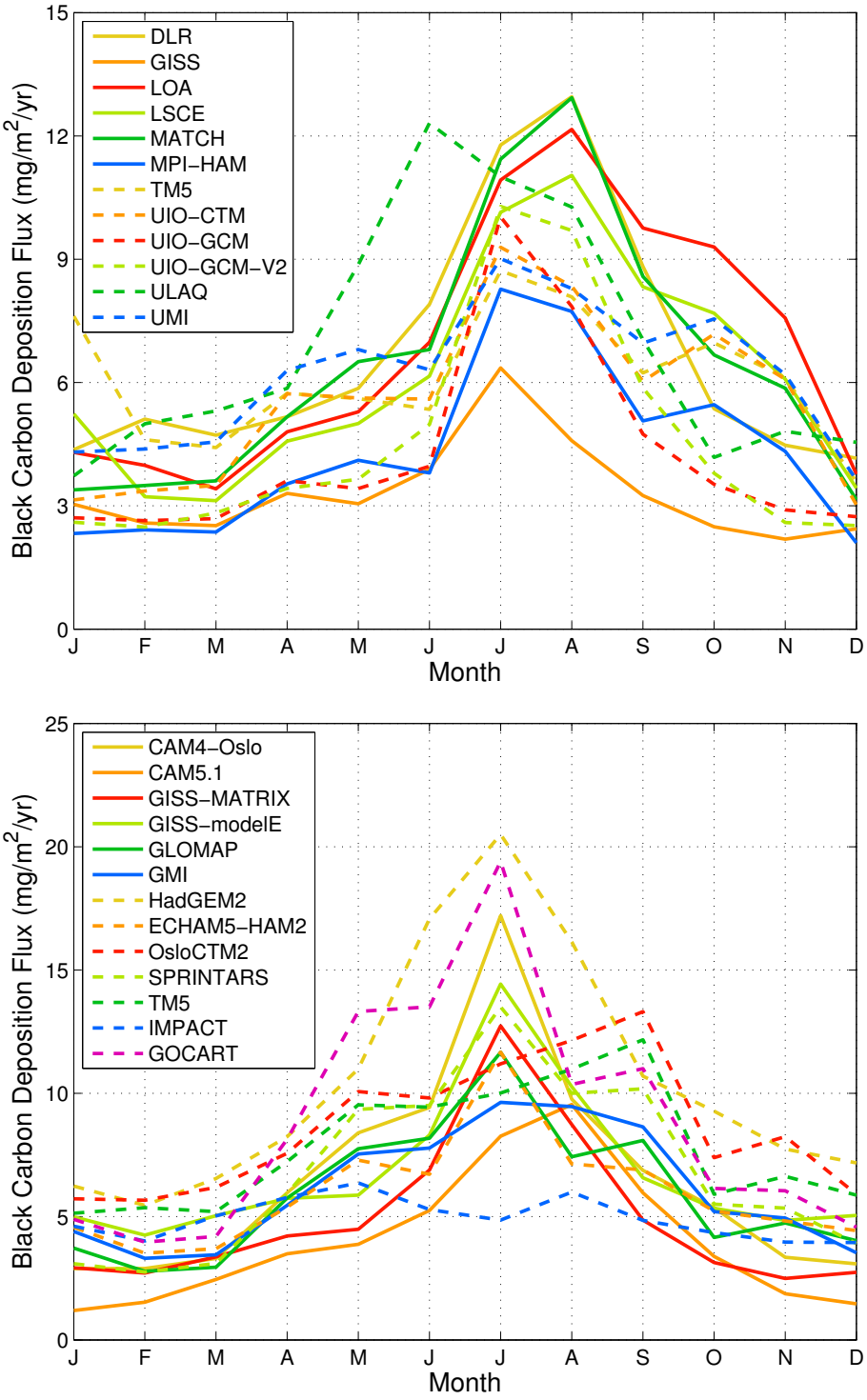

Figure 2.10: Seasonal cycle of black carbon deposition fluxes averaged over the Arctic (60°N to 90°N) for Phase I (upper panel: Figure 2.10a) and Phase II (lower panel: Figure 2.10b) models. (Note the scale on ordinate is different for the two plots.)

(*Garrett et al.*, 2010; *Browse et al.*, 2012; *Lund and Berntsen*, 2012; *Wang et al.*, 2013). *Liu et al.* (2011) concluded that the simulation of BC in the Arctic is significantly improved by using a parameterization of BC aging rate that is proportional to the OH radical concentration, reducing dry deposition velocities over ice and snow, and decreasing ice cloud wet removal efficiency. These changes increased wintertime BC concentrations by a factor of 50–100. *Browse et al.* (2012) improved the simulated seasonal cycle of Arctic aerosols by including more realistic treatment of the transition in scavenging efficiency associated with changes in cloud phases. *von Hardenberg et al.* (2012) reported a more realistic yearly averaged simulated AOD in the Arctic compared to observations by using the modified wet scavenging scheme suggested by *Bourgeois and Bey* (2011). Together, these studies indicate that deposition parametrizations are critical for determining both the latitudinal profile of the modeled BC, and the efficiency through which Arctic atmospheric BC is removed. Precise attribution of how physical parameterizations contribute to model diversity requires carefully designed perturbation experiments, such as those conducted by *Lee et al.* (2013a).

One consequence of our methodology for simulating BC-in-snow concentrations is that the meteorological conditions used to drive CLM and CICE may be inconsistent with those determining the model deposition amounts. We chose to drive each simulation with the same 2005–2009 re-analysis data because 1) these meteorological conditions are likely to be more compatible than model-generated fields with conditions that prevailed during the measurement campaigns, and thus will produce more similar model snowpack conditions to those from which measurements were drawn, and 2) using the same meteorological conditions for each simulation reduces the number of free variables and enables a more lucid inter-comparison of BC-in-snow concentrations resulting from different BC deposition fields. To evaluate the potential impact of this design choice, we conducted a sensitivity study with CLM and CICE coupled inter-

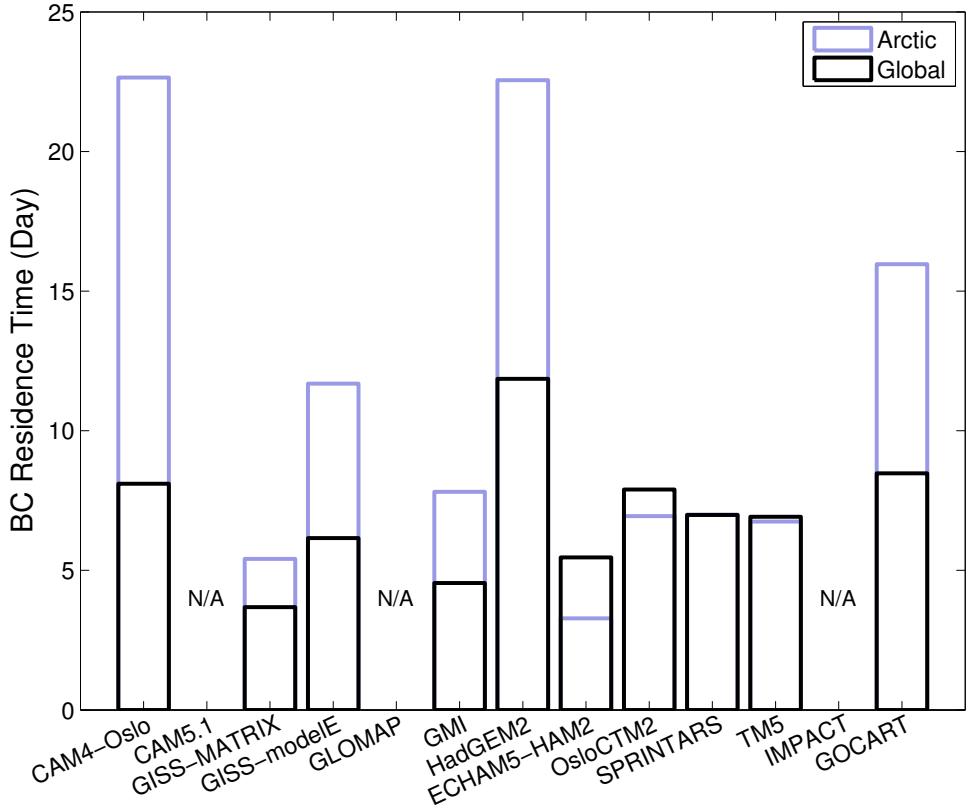

Figure 2.11: Global and Arctic atmospheric residence times for black carbon in Phase II models. (Three models are excluded in this analysis due to missing or incomplete data.)

actively (online) with the Community Atmosphere Model (CAM), and the transport and deposition of aerosols are simulated prognostically in a self-consistent way with model meteorology. We then used deposition fields from this simulation to drive CLM and CICE offline in the same period, using the same re-analysis product as described in Section 2.3. We find that the model–measurement bias averaged over the sampling domain is –9.7 $\mathrm{ng\,g^{-1}}$ in the online simulation, while it is –0.1 $\mathrm{ng\,g^{-1}}$ for the offline CLM/CICE simulation. The correlation coefficient between model and observation is 0.16 for online simulation and 0.18 for offline simulation. This sensitivity study indicates that choice of meteorology can have a significant impact on model–measurement comparison. The sign of impact is also consistent with a preliminary study (Sarah Doherty, personal communication) suggesting that use of inconsistent deposition and precipitation fluxes can produce a high bias in surface layer BC concentrations. This could imply that model deposition fluxes in the Arctic have more low bias (or less high bias) than indicated by our study. Applying identical meteorological fields with all deposition fields also likely reduces inter-model diversity in simulated BC-in-snow amounts.

2.4.4 The Effect of Meltwater Scavenging

As insolation increases during spring in the Arctic, surface snow begins to melt. As the meltwater percolates into deeper snow it collects some of the impurities, altering the vertical distribution of BC in snow and sea-ice. We run CLM and CICE with two sets of BC meltwater scavenging coefficients in order to evaluate impacts of uncertainty in these parameters. The inefficient scavenging (IS) scenario applies the same scavenging coefficients used by *Flanner et al.* (2007), leading to accumulation of BC near the snow surface as melt occurs, whereas the ES sensitivity studies apply scavenging coefficients of 1.0 for both hydrophilic and hydrophobic BC. Though the ES scenario is not supported with observations, it enables an assessment of the

potential impact of this parameter on the model evaluations.

Figure 2.12 divides the model–measurement comparison shown in Figure 2.2 into eight different regions. From Figure 2.12, we can see that the scavenging sensitivity study has different impacts in different regions, reflecting differing degrees to which the regional sampling domains are affected by melt. In some regions, including the Canadian Arctic, Alaska, Canadian Sub-Arctic and Ny-Ålesund, the differences between IS and ES scenarios are very small. In Greenland however, and to a lesser extent Tromsø and the Arctic Ocean, there are noticeably higher modeled BC-in-snow concentrations in the IS scenario. To highlight the role of snow melt in modulating the importance of these parameters, we plot the histogram of the months when the samples are collected and the monthly mean snow melt rate averaged over grid cells matching the observations in the different regions (Figure 2.13). In regions that show no significant difference between IS and ES scenarios, there are few samples collected during times of large snow melt. For example, the Ny-Ålesund samples were collected during March–May, before the July peak in model snow melt rate, meaning the sub-sampled model domain is largely unaffected by melt. Most of the Greenland samples were collected at lower elevations during July and August, however, coincident with peak melt rates in the matching model domain (Figure 2.13). About 43% of the sampling space coincides with the top model snow layer, and over 70% of it coincides with the top two model layers, where simulated concentrations are sensitive to the scavenging parameter during conditions of melt. Because much of the sampling space does not coincide with strong melt, however, the melt scavenging coefficients have only a second-order impact on the Arctic-wide model–measurement evaluation.

2.5 BC-in-snow Radiative Effect

Figure 2.14 shows the annual mean surface radiative effects caused by BC in snow, as simulated with deposition fields from the Phase I and Phase II models. Regions

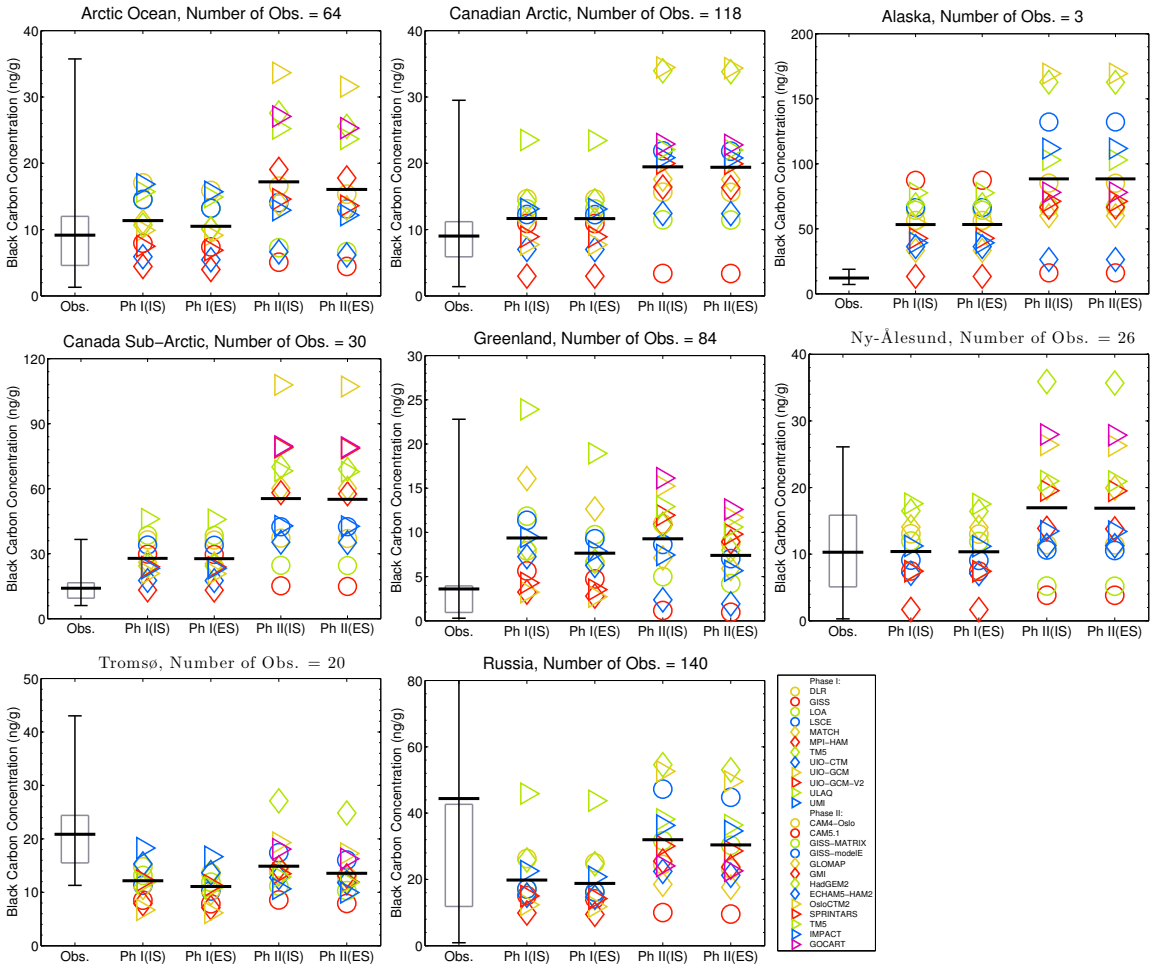

Figure 2.12: Same as Figure 2.2, but plotted for 8 individual regions. The number of observations within each region is listed in the figure titles.

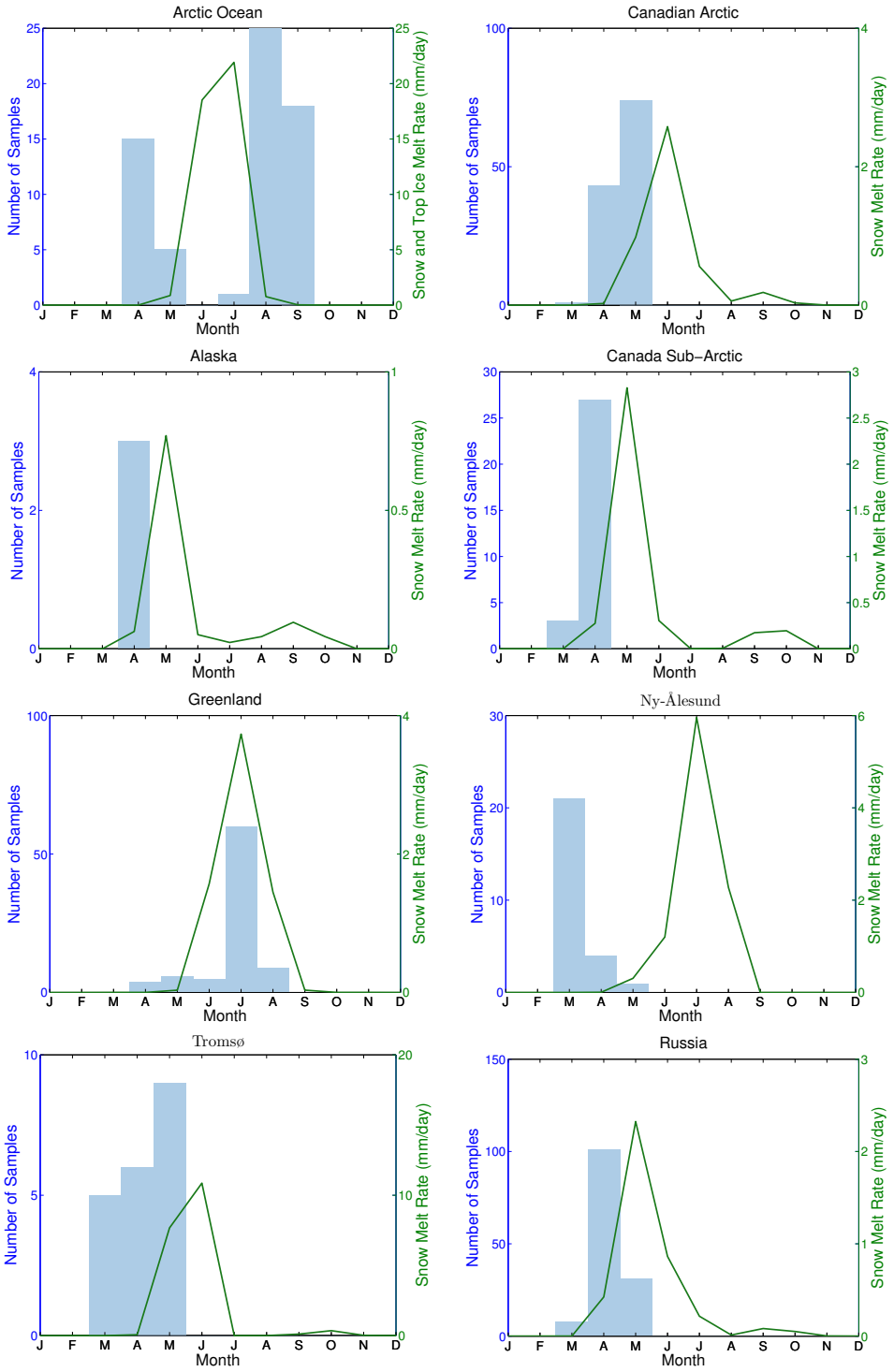

Figure 2.13: Histogram of the months when the samples are collected in each regions (plotted against left axis) and seasonal cycle of snow and ice melt rates (plotted against right axis). The melt rates are averaged only over grid cells containing observations within each region.

with relatively large radiative effects are northern Europe, Russia and Greenland. The two primary factors influencing annual-mean radiative effect in different regions are the amount of BC in snow and the seasonal evolution of snow cover fraction. For example, perennial snow cover on Greenland enables large forcing in this region despite relatively small BC concentrations. Persistence of cryospheric cover through summer is especially important because it maximizes the amount of insolation incident on impurity-laden snow and ice. The relatively small BC-in-snow radiative effects in central Greenland are caused by the small BC deposition fluxes in this area (Figure 2.8 and 2.9) as well as little surface BC accumulation due to low snow melt rate associated with high altitude and low temperature. Arctic annual mean BC in snow radiative effects for both phases and both sets of meltwater scavenging coefficients are shown in Table 2.4. With inefficient scavenging, the modeled Arctic radiative effects for Phase I models range from $0.07\,\mathrm{W\,m^{-2}}$ to $0.25\,\mathrm{W\,m^{-2}}$, and range from $0.06\,\mathrm{W\,m^{-2}}$ to $0.28\,\mathrm{W\,m^{-2}}$ for Phase II models. With efficient scavenging, the radiative effects are slightly smaller, ranging from 0.06–$0.21\,\mathrm{W\,m^{-2}}$ and 0.05–$0.24\,\mathrm{W\,m^{-2}}$, respectively, for Phase I and Phase II models.

The multi-model mean BC-in-snow radiative effect averaged over the Arctic (here, 60–90°N) is $0.15\,\mathrm{W\,m^{-2}}$ and $0.18\,\mathrm{W\,m^{-2}}$ for Phase I and Phase II models, respectively, with inefficient meltwater scavenging. Model biases in BC concentrations in snow may also translate into biases in Arctic-mean radiative effect. Here we use the ratio between simulated and observed BC concentrations in different regions of the Arctic to derive observationally-constrained forcings. In doing so, we assume a linear relationship between the near surface BC-in-snow concentration and radiative effect, which is a reasonable assumption for small perturbations about low BC concentrations (e.g., *Flanner et al.*, 2007), such as those found in most of the Arctic. We divide the Arctic into 6 regions (Europe, Russia, Alaska, Canada, Greenland and the Arctic Ocean) and scale the modeled radiative effects in each region by the ratio of observed-to-

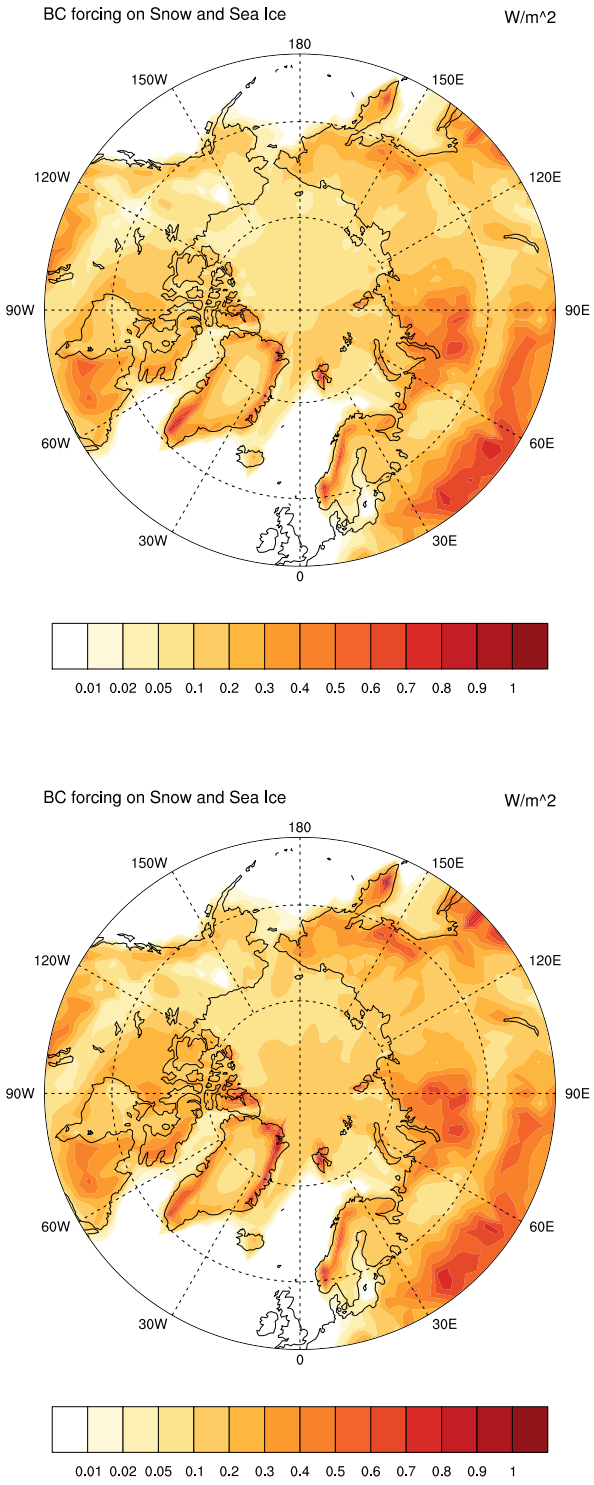

Figure 2.14: Annual mean BC-in-snow radiative effects averaged across Phase I (upper panel: Figure 2.14a) and Phase II (lower panel: Figure 2.14b) models with inefficient meltwater scavenging.

Table 2.4: Arctic BC-in-snow radiative effects, averaged from 60°N to 90°N ($\mathrm{W\,m^{-2}}$)

Phase I	IS	ES	Phase II	IS	ES
DLR	0.18	0.15	CAM4-Oslo	0.16	0.13
GISS	0.10	0.09	CAM5.1	0.06	0.05
LOA	0.17	0.14	GISS-MATRIX	0.12	0.10
LSCE	0.15	0.13	GISS-modelE	0.20	0.17
MATCH	0.14	0.12	GLOMAP	0.16	0.14
MPI-HAM	0.07	0.06	GMI	0.15	0.13
TM5	0.19	0.16	HadGEM2	0.28	0.24
UIO-CTM	0.13	0.11	ECHAM5-HAM2	0.11	0.09
UIO-GCM	0.10	0.08	OsloCTM2	0.27	0.23
UIO-GCM-V2	0.10	0.08	SPRINTARS	0.18	0.15
ULAQ	0.25	0.21	TM5	0.23	0.20
UMI	0.18	0.15	IMPACT	0.17	0.15
			GOCART	0.22	0.18

IS indicates inefficient meltwater scavenging
ES indicates efficient meltwater scavenging

modeled BC concentrations in the sampling domain within each region. For each of the five land-based regions, the radiative effect is simulated with CLM, whereas radiative effect within the Arctic Ocean is simulated with CICE. Using this correction technique, we calculate an Arctic-mean BC-in-snow radiative effect of $0.17\,\mathrm{W\,m^{-2}}$ for the combined Phase I and Phase II ensembles. This approach has the advantage of accounting for model performance in different regions of the Arctic, but is only useful to the extent that model performance over the sampling domain is representative of model performance over each region as a whole.

2.6 Conclusions

We have used black carbon (BC) deposition fields produced from 25 global aerosol models to simulate vertically-resolved BC concentrations in snow and sea-ice with offline components of the Community Earth System Model. This exercise has enabled us to explore inter-model variability in Arctic BC deposition, evaluate model BC fields against a comprehensive field survey of BC measurements in Arctic snow (*Doherty*

et al., 2010), and develop an observationally-constrained estimate of Arctic radiative effects from BC in snow and sea-ice. Though model mean BC concentrations in snow, averaged over the measurement domain, are generally close to the observational means, correlation coefficients between simulated and observed values are low, and variability among models is large. Models tend to underestimate BC amounts in snow in the Russian Arctic and northern Norway, while overestimating BC elsewhere in the Arctic. On average, however, Phase I and Phase II multi-model mean BC-in-snow concentrations are only $4.4\,\mathrm{ng\,g^{-1}}$ lower and $4.1\,\mathrm{ng\,g^{-1}}$ higher, respectively, than the observational mean of $19.2\,\mathrm{ng\,g^{-1}}$. Analysis shows that model aerosol transport and removal processes are the main factors influencing model–measurement evaluations, rather than the efficiency of particle removal with snow melt water or variability in emissions applied within the models. Model residence times of BC in the Arctic atmosphere range from 3.7 to 23.2 days, much larger than the range in global residence times, indicating large model variability in local deposition efficiency. Multi-model means (ranges) of Arctic (60–90°N) annual-mean radiative effects from BC in snow are 0.15 (0.07–0.25) $\mathrm{W\,m^{-2}}$ and 0.18 (0.06–0.28) $\mathrm{W\,m^{-2}}$ in Phase I and Phase II models. After correcting these estimates for biases in different regions of the Arctic, the mean Arctic radiative effects become $0.17\,\mathrm{W\,m^{-2}}$ for the combined Phase I and Phase II ensembles.

CHAPTER III

Changing Black Carbon Transport to the Arctic from Present Day to the End of 21st Century

3.1 Introduction

Arctic climate has changed rapidly during recent decades, including increased surface temperature, reduced sea ice and land snow, and altered atmospheric circulation. One contributor to this change is altered distributions of absorptive aerosols (black carbon, brown carbon and dust) which are transported to the polar region, heat the atmosphere, and darken snow and ice surfaces (e.g., *Flanner et al.*, 2007; *Ramanathan and Carmichael*, 2008; *Bond et al.*, 2013). The Arctic aerosol distribution is governed by three factors: emission, transport and deposition. The emission source within the Arctic is small (e.g., *Lamarque et al.*, 2010; *Browse et al.*, 2013) and hence emissions outside the Arctic contribute the majority of the Arctic aerosol burden via atmospheric transport (e.g., *Koch and Hansen*, 2005; *Law and Stohl*, 2007). Understanding the transport and deposition processes that govern Arctic aerosols will help us to better constrain the Arctic aerosol budget. Furthermore, both the transport and deposition processes are subject to change associated with global climate warming. Thus it is our interest to examine those changes and investigate their influences on the Arctic aerosol budget.

The characteristics of aerosol transport and deposition have been examined in several studies. *Stohl* (2006) used a Lagrangian particle dispersion model to show that aerosol tracers emitted from North America and Asia generally experience uplift outside the Arctic and then can be transported into the Arctic. Pollution from Europe can travel to the Arctic by both low and high altitude pathways. *Shindell et al.* (2008) used a multi-model approach to reveal that European emissions dominate the surface aerosol and carbon monoxide budget of the Arctic, while emissions from East Asia are important for high altitude burden. They also concluded that Europe and North America are the two most dominant contributors to black carbon (BC) on Greenland, with each contributing about 40% of the total BC deposition in that region. Along with aerosol transport to the Arctic, the removal processes that occur during the transport to and within the Arctic are equally important for the Arctic aerosol budget. *Garrett et al.* (2010) and *Garrett et al.* (2011) applied observations to show that the seasonality of both light absorbing and light scattering aerosols in the Arctic are controlled by wet scavenging. They argued that high relative humidity and warm temperatures would lead to more efficient removal of aerosols in spring and summer seasons. *Garrett et al.* (2011) also suggested that the Arctic might be cleaner in the future due to the projected warmer and wetter climate. *Liu et al.* (2011) found that simulated Arctic BC concentrations improved significantly compared to observations after adjusting the aerosol aging, dry deposition and wet removal processes represented in the GFDL AM3 model. *Zhou et al.* (2012) found that both the meteorological fields and the wet deposition treatment in their model have strong influences on BC concentrations and deposition in polar regions. *Wang et al.* (2013) evaluated and improved the aerosol processes, including aerosol–cloud interactions, cloud microphysics and macrophysics, aerosol transformation, convective transport and aerosol wet removal, in the Community Atmosphere Model version 5 (CAM5). They significantly improved the BC and sulfate distribution in the Arctic

compared to observations, and identified wet removal, aerosol aging time and aerosol–cloud interactions as the most important processes that influence the remote aerosol budget.

Previous studies have explored features of global aerosol transport using Eulerian models with different tracer identification methods (e.g., *Koch and Hansen*, 2005; *Shindell et al.*, 2008; *Wang et al.*, 2011; *Ma et al.*, 2013; *Wang et al.*, 2014a). All of those studies either used explicit regional emission tags or emission sensitivity (perturbation) techniques to track and archive the temporal and spatial characteristics of aerosols emitted from different regions. Studies with Lagrangian particle dispersion models can track the behavior of many individual tracers, which makes them ideal for studies of aerosol transport process (*Stohl*, 2006). These models typically do not have sophisticated representations of aerosol removal processes, however, and it is our interest here to examine the relative impacts of changing aerosol transport and deposition in the context of Arctic climate change.

In this study, we combine merits of both modeling approaches. We modified the bulk aerosol module (BAM, (*Rasch et al.*, 2000)) component of CAM to explicitly simulate hundreds of tagged BC aerosol tracers. Each of these tagged tracers has a distinct emission source region. With the modeling framework developed for this study, we investigate how the aerosol tracer distribution from different emission locations is influenced solely by changes in atmospheric transport, and secondly by transport and deposition processes combined. Detailed description of the experiment design is in Section 3.2.

One of the primary objectives of this study is to investigate how warming of the climate system could affect the spatial distribution of aerosols emitted from different locations, especially in high latitude regions. This is motivated by numerous recent studies showing that there will be pronounced changes in Arctic circulation and climate associated with global climate warming (e.g., *Serreze et al.*, 2009; *Screen and*

Simmonds, 2010; *Francis and Vavrus*, 2012; *Screen et al.*, 2012; *Bintanja and van der Linden*, 2013). For example, *Serreze et al.* (2009) showed that surface and lower tropospheric Arctic air temperatures are projected to rise at a significantly faster pace than other regions of the northern hemisphere, in response to increasing greenhouse gas concentrations, especially during the winter season. This phenomenon is referred to as Arctic Amplification (*Holland and Bitz*, 2003; *Screen and Simmonds*, 2010). *Francis and Vavrus* (2012) argued that Arctic Amplification could produce important changes in mid-latitude circulation, including a weakening of zonal winds and an increase in Rossby wave amplitude, particularly during the fall and winter seasons. *Lee et al.* (2015) stated that anomalously warm sea surface temperatures and low sea ice concentrations in the Arctic led to recent mid-latitude winter atmospheric circulation anomalies. It follows that aerosol transport pathways to the Arctic will also change in concert with changing circulation patterns associated with Arctic amplification. Here, we run experiments with present day climate conditions as well as climate conditions and emissions at the end of the 21st century as simulated under the Representative Concentration Pathway 8.5 (RCP8.5) scenario. By comparing the simulations from those two climate states, we quantitatively analyze changes in aerosol transport pathways, column burdens, deposition fluxes and atmospheric lifetimes associated with emissions from different locations. In order to distinguish the characteristics of tracers emitted from different geographical locations, we resolve the major emission source regions in northern hemisphere mid-latitude regions with 200 tagged tracers. The number of different tagged tracers studied here is much larger than in other studies employing Eulerian transport models, but the relatively simple aerosol treatment of BAM permits such simulations to be conducted with modest computational expense.

3.2 Experiment Design

We use the coupled Community Atmosphere Model version 4 (CAM4), Community Land Model version 4 (CLM4), Community Ice Code (CICE) and Data Ocean Model within the framework of the Community Earth System Model version 1.1.1 (CESM1). The models are driven with prescribed annually-repeating sea surface temperature (SST) and sea ice fields. This model framework generally shows low biases in the simulated climatological fields such as surface temperature, sea ice fraction and precipitation, and has realistic representation of the El Niño – Southern Oscillation and Madden - Julian oscillation (*Gent et al.*, 2011). Meanwhile, *Gent et al.* (2011) also pointed out the CAM4 has relatively poor representation of the precipitation field in the tropical Pacific Ocean and the low cloud content in the Arctic. Previous studies have also evaluated the simulated aerosol fields of CAM4 with BAM (e.g., *Lamarque et al.*, 2011, 2012). *Lamarque et al.* (2012) found that CAM4 tends to underestimate the aerosol optical depth over most regions compared to MODIS (Moderate Resolution Imaging Spectroradiometer) and MISR (Multi-angle Imaging SpectroRadiometer) satellite observations. In CAM4, the simulated sulfate fields generally agree with observations (*Lamarque et al.*, 2012). Yet elemental carbon and organic carbon aerosol fields simulated by CAM4 show relatively large biases compared to near-surface measurements at the IMPROVE (United States Interagency Monitoring of Protected Visual Environments) sites (*Lamarque et al.*, 2012). Some of the biases in CAM4, such as the underestimation of BC both near surface and in middle – high troposphere in Arctic, are also consistent with other models (e.g., *Koch et al.*, 2009b; *Lee et al.*, 2013b; *Eckhardt et al.*, 2015).

In this study, we run CAM4 at $2.5^\circ \times 1.9^\circ$ horizontal resolution with 26 hybrid sigma pressure layers. In order to record multiple tagged tracers in the model, we modify BAM to enable any number of BC-like aerosol tracers to be simulated. All added tracers are identical to BC in terms of physical properties. BAM treats BC

as externally mixed with respect to other aerosol species, and hence this model is relatively unsophisticated compared with aerosol models that consider internal mixing and evolving size distributions of BC, e.g., via aerosol coating and coagulation (e.g., *Liu et al.*, 2012). We exclude the added tracers from the radiative transfer calculations in the model, and BAM also does not treat aerosol-cloud microphysical interactions. Hence, the added tracers are climate passive and the simulated climate is exactly like the one without the added tracers. This is a necessary design feature because aerosol distributions in some of our idealized experiments are unrealistic and would have detrimental effects on the simulated climate if they were radiatively active.

One scientific question we strive to address in this study is how much of the change in each tracer's spatial and temporal distribution under different climate scenarios can be attributed to changes in atmospheric transport pathways, and how much is caused by changes in aerosol deposition. In order to quantify the individual contributions from transport and deposition, we design two experiments to separate the change in Arctic aerosol distribution associated with those two processes. Experiment "Transport" (EXP:T) is designed so only changes in atmopsheric transport affect the tracer's distribution. In EXP:T, all tracers have the same e-folding lifetime of 4 days. Both the dry and wet deposition for these tracers are disabled, so all tracers will stay in the atmosphere for exactly the same time and all changes in the tracer's distribution are caused solely by changes in atmospheric circulation. Experiment "Transport+Deposition" (EXP:T+D) is designed to consider both transport and deposition processes. In EXP:T+D, all tracers are emitted in the hydrophobic mode and convert to hydrophilic mode with an e-folding lifetime of 1.2 days, as in the default configuration of BAM. The hydrophobic tracer can only be removed by dry deposition and the hydrophilic tracer can also be removed from the atmosphere by both in-cloud and below cloud removal processes (*Rasch et al.*, 2000; *Barth et al.*, 2000). In other words, in EXP:T+D, the parameter settings for tracer wet and dry

deposition processes are the same as the default settings for BC aerosol in BAM. For both EXP:T and EXP:T+D, the model uses the CAM4 default finite volume dynamical core for tracer advection.

To compare tracer transport and deposition in changing climates, we drive the model with SST and sea-ice distributions which represent present day and future climate for both EXP:T and EXP:T+D. For present day climate we drive the model with a climatological mean annual cycle of SSTs, averaged from 1982 to 2001. The SSTs representing future climate are averaged from the last ten years (2090 – 2099) of a CESM1 simulation with fully coupled atmosphere, ocean and land model components under the RCP8.5 forcing scenario. We denote simulations which represent present day climate by "PRD" and future climate by "RCP".

There are therefore four sets of simulations conducted for this study: EXP:T in PRD, EXP:T in RCP, EXP:T+D in PRD and EXP:T+D in RCP. In all four experiments, we simulate 200 tagged tracers which are emitted from different locations from the northern hemisphere mid-latitude land area. Figure 3.1 shows the emission locations for the 200 individual aerosol tracers applied in this study. All 200 tracers have the same emission rates, enabling us to easily explore the relative geographic differences in how aerosol distributions are influenced by transport and removal processes. In Section 3.4.3, we also include two additional tracers associated with global BC emission inventories for present day and year 2100 under the RCP8.5 scenario (*Rao and Riahi*, 2006; *Riahi et al.*, 2007, 2011). These tracers are subject to model circulation and deposition as in EXP:T+D. The analysis in Section 3.4.3 enables us to quantify how the actual Arctic BC budget might change in future climate due to changes in aerosol transport and deposition processes as well as changes in emissions. In each of the experiments, we run the model for 16 years with annually repeating SSTs and sea-ice fields for present and future climatologies. The first year is used for spin-up and the remaining 15 years of simulation are used for analysis.

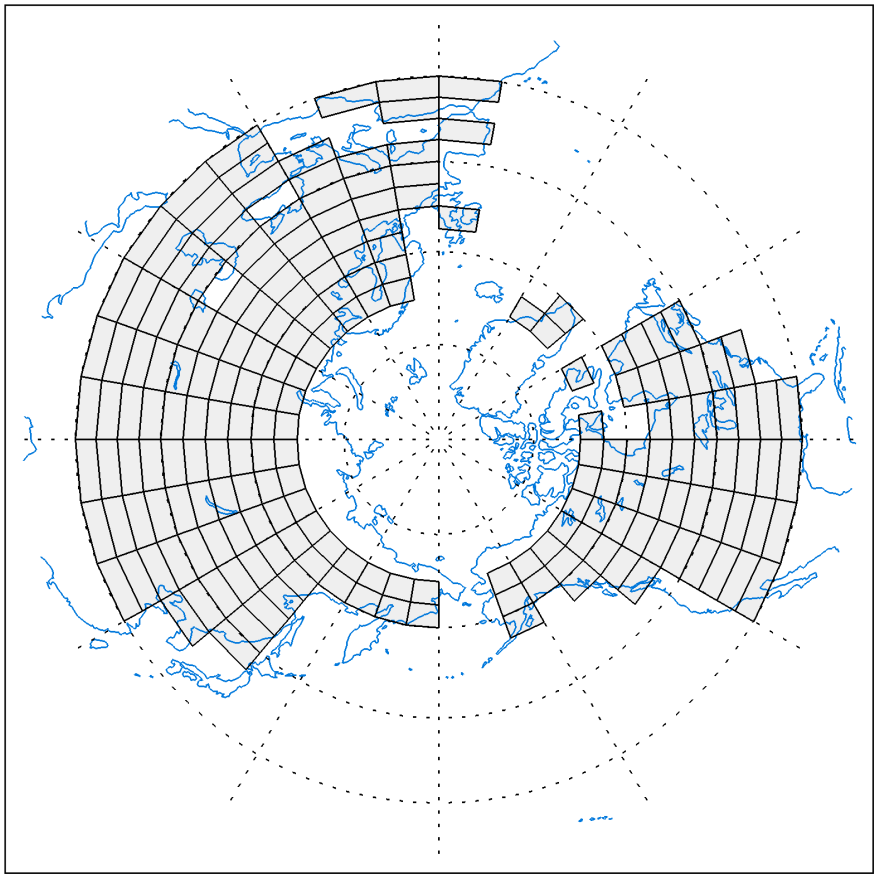

Figure 3.1: The emission locations of the 200 tagged aerosol tracers are indicated by each individual box with grey shading in this figure.

3.3 Methods

3.3.1 Arctic Aerosol Fraction

In order to quantify how effectively an aerosol tracer from a particular source location travels to (and remains within) the Arctic region (60 – 90°N), we utilize the ratio of the tracer's Arctic mean atmospheric column burden to global mean burden. We apply the term "Arctic aerosol fraction" (AAF) to this proxy value and quantify a tracer's AAF as:

$$AAF_{Tracer} = \frac{\int_{0^\circ}^{360^\circ} \int_{60^\circ}^{90^\circ} \int_{0}^{\mathrm{TOA}} q_{Tracer}(z)\, \rho(z)\, cos(\phi)\, dz\, d\phi\, d\theta}{\int_{0^\circ}^{360^\circ} \int_{-90^\circ}^{90^\circ} \int_{0}^{\mathrm{TOA}} q_{Tracer}(z)\, \rho(z)\, cos(\phi)\, dz\, d\phi\, d\theta} \tag{3.1}$$

where $q_{Tracer}(z)$ is the atmospheric mass mixing ratio for that particular tracer at altitude z with unit $\mathrm{kg\,kg^{-1}}$, and $\rho(z)$ is the air density at altitude z with unit of $\mathrm{kg\,m^{-3}}$. The AAF is unitless and simply the fraction of the aerosol tag's total global atmospheric burden that is located within the Arctic. For tracers that experience efficient transport to the Arctic, the AAF will be higher than those that experience transport barriers to the Arctic and/or have shorter atmospheric lifetimes. This quantity is utilized in the analysis of both EXP:T and EXP:T+D.

3.3.2 Polar Dome Definition

The polar dome is a boundary which separates cold air in the Arctic from the relatively warm air in mid-latitude regions. This is an important feature both for aerosol transport and as a general atmospheric phenomenon (*Klonecki et al.*, 2003; *Stohl*, 2006). In order to quantitatively analyze the polar dome's influence on aerosol transport, we have developed a rigorous definition of the polar dome by analyzing the 500 hPa geopotential height fields. First we calculate the latitudinal gradient of northern hemisphere 500 hPa geopotential height at all longitudes. Then we find the latitude, at each longitude, in which the geopotential height gradient is maximal. Next

we take the average of the corresponding 500 hPa geopotential heights in those grid cells found above. We then locate a circumpolar isopleth based on the value calculated above and define this isopleth as the boundary of the polar dome. By this method, the polar dome is identified by the maximum zonal mean latitudinal gradient of 500 hPa geopotential height in the northern hemisphere. Logic behind this definition is that where the latitudinal geopotential height gradient is largest, the zonal component of the geostrophic wind at that level is likely to be strongest, and this narrow band of strong geostrophic wind plays an important role for tracer transport in the middle troposphere. This narrow band of strong geostrophic wind, often referred to as the jet stream, also has a strong influence on weather systems, surface temperature, and storm tracks. The location of the polar dome and the strength of the wind speed associated with the jet stream have strong seasonal cycles. The location extends to middle latitude regions during winter and the jet wind speed reaches a maximum during this time of year. This results from the stronger temperature gradient between low and high latitude regions in winter. During summer, the location of the polar dome retreats to the north and the jet stream also weakens.

3.4 Results

This paper explores how warming of the climate system could influence the Arctic contributions of emissions from different regions via changing atmospheric transport and deposition processes. For EXP:T, we will focus our analysis primarily on January based on two reasons. First, as mentioned, the polar dome is strongest and has the most southerly extent in January, and hence changes in the dome during this season are likely to have the most pronounced impact on aerosol transport to the Arctic. Second (and related), observations show that the Arctic aerosol surface air concentrations have strong seasonality (e.g., *Sharma et al.*, 2006), with the winter months showing higher amounts and peak surface concentrations occurring in March, likely

due to winter accumulation and weak winter deposition. Thus compared to summer, the winter budget of Arctic aerosol appears to be more dependent on transport processes. Although our analysis of EXP:T focuses on January, we also provide a brief discussion of a summer month (July). From analysis of climate-induced changes in tracer AAF in EXP:T+D, we will see that aerosol deposition processes become the dominant source of change in Arctic aerosol burden, leading us to explore impacts during both winter (January) and summer (July) for this experiment. The additional BC tracers associated with realistic global BC emissions discussed in Section 3.4.2 and 3.4.3 will be used to examine the relative change in normalized tracer deposition rate (sometimes referred to as the first order removal rate) and its relationship to changes in precipitation. The annual mean Arctic budget of this set of BC tracers will also be analyzed, providing a quantitative assessment of how the Arctic BC budget would change in future climate due to changes in transport and deposition processes as well as changes in BC emissions.

3.4.1 Result for Experiment Transport

3.4.1.1 Arctic Aerosol Fraction

Figure 3.2a shows the spatial pattern of the Arctic aerosol fraction (AAF) for all of the 200 tracers in present day climate with Experiment Transport (EXP:T) in January. From Figure 3.2a we can see that, as expected, the AAF of tracers emitted closer to the Arctic is generally larger. The pattern also exhibits zonal asymmetries in the mid-latitudes, however, especially over Eurasia. The figure shows a trough-like structure near eastern Europe and western Asia, and the wave-like pattern is disrupted by the high Tibetan Plateau. Tracers emitted from the European continent general have higher AAF compared to the tracers emitted from East Asia in the same latitude. The pattern over North America is more symmetric. Zonal asymmetry in transport efficiency is caused by the combined effects of the location of the polar dome,

which controls the middle to upper troposphere long range transport (Figure 3.5), differences in surface potential temperature, and variable topography that controls low level transport from the source region. Figure 3.2b shows the AAF pattern in future climate, and Figure 3.2c shows the relative change of the AAF from present day to future climate, normalized by the present day value ((RCP-PRD)/PRD). We find that for tracers emitted from the eastern and western boundaries of the Pacific Ocean, the AAF changes substantially in future climate. Tracers emitted from East Asia have an increased Arctic fraction in the future, while the Arctic fraction for tracers emitted from North America decreases significantly. As *Koch and Hansen* (2005) and *Stohl* (2006) discovered, tracers from those two regions transport to the Arctic primarily through the middle to upper troposphere, which means they need to be lifted in the troposphere before they can be transported to the Arctic. Based on this, we try to link the change in transport to change in middle troposphere dynamics in the relevant regions.

Figure 3.2c indicates that emissions from different regions will experience substantially different changes in dynamical transport efficiency to the Arctic associated with warming climate. For example, the AAFs for tracers emitted from East Asia increase around 10% – 22% in future climate, and the AAFs for North American tracers decrease around 21% – 33%, due solely to changes in aerosol transport. Here we use two case studies to highlight the transport pattern shifts associated with tracers emitted from East Asia and North America, two of the largest anthropogenic emission regions in the northern hemisphere. Figure 3.3a depicts the distribution of tracers emitted from East Asia in January. Following emission, these tracers tend to travel in one of two directions: towards the southwest or northeast. The northeast branch is the one primarily taken by tracers contributing to the Arctic burden. Figure 3.3b shows the change of tracer distribution from present day to future climate, which reveals an enhanced burden of tracers over the Arctic, especially over eastern Russia and

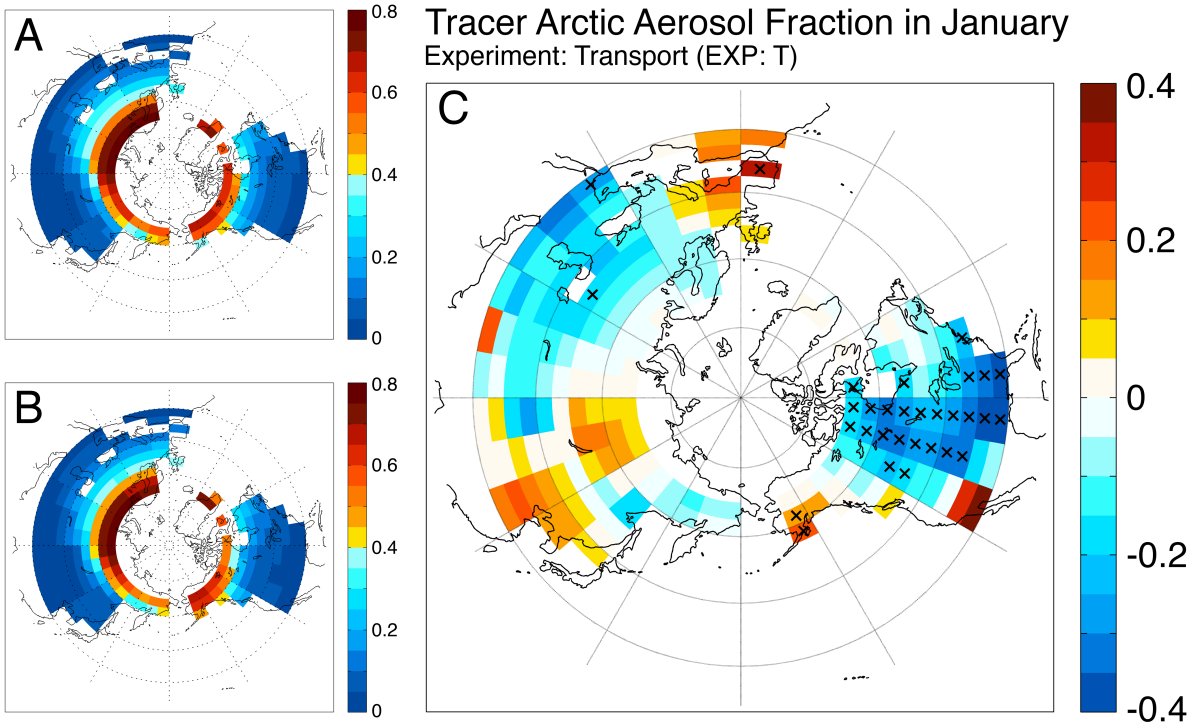

Figure 3.2: Contour plot of January Arctic aerosol fraction (AAF) of the 200 tracers for (a): present-day (PRD) climate, (b): end of 21st century climate (RCP8.5), and (c): the relative change between RCP and PRD ((RCP-PRD)/PRD). Relative changes significant at the $\alpha < 0.05$ level, determined with the Wilcoxon rank-sum test, are shown with cross signs.

Alaska, indicating enhanced transport via the northeast branch. For tracers emitted from North America, Figure 3.3d shows that the Arctic burden decreases significantly in future climate.

To explore reasons for the changes shown in Figure 3.3, we turn to an analysis of the tracers' three dimensional distribution. Figure 3.4 shows the zonal mean vertical profile of tracers from East Asia, North America and Europe averaged over different latitudinal zones in January and July. The four latitudinal zones are chosen to represent mid-latitude regions and the Arctic: 32 – 42°N, 42 – 52°N, 52 – 62°N and 62 – 90°N. Figure 3.4a shows that tracers emitted from East Asia in January are concentrated near the surface and in the lower troposphere near the source region. The tracer moves into the higher atmosphere when it travels northward, as the mid-troposphere concentration increases while the lower atmospheric concentration decreases. When the tracer reaches the Arctic, its vertical profile (purple line) indicates the maximum concentration is located near the middle to upper troposphere (around 400 hPa to 500 hPa). This reveals that East Asian tracers travel to the Arctic mostly through the middle to upper troposphere. Combined with Figure 3.3a, we identify the middle to upper troposphere over northeastern Siberia, the Bearing Sea and Alaska as the most important transport gateway to the Arctic for East Asian emissions. Figure 3.4b shows the zonal mean vertical profile of tracers emitted from North America in January. This indicates that, like the East Asian tracers, emissions from North America tend to travel to the Arctic through the middle to upper troposphere. Based on this analysis, we attribute the warming-induced change in these tracers' Arctic transport efficiencies to changes in the mid-tropospheric wind near each respective transport gateway. European emissions are also an important source of the total Arctic burden. Figure 3.4c shows the zonal mean vertical profile for a representative subset of European tracers in January. We can see that the tracers are concentrated near the surface and lower atmosphere throughout the source region

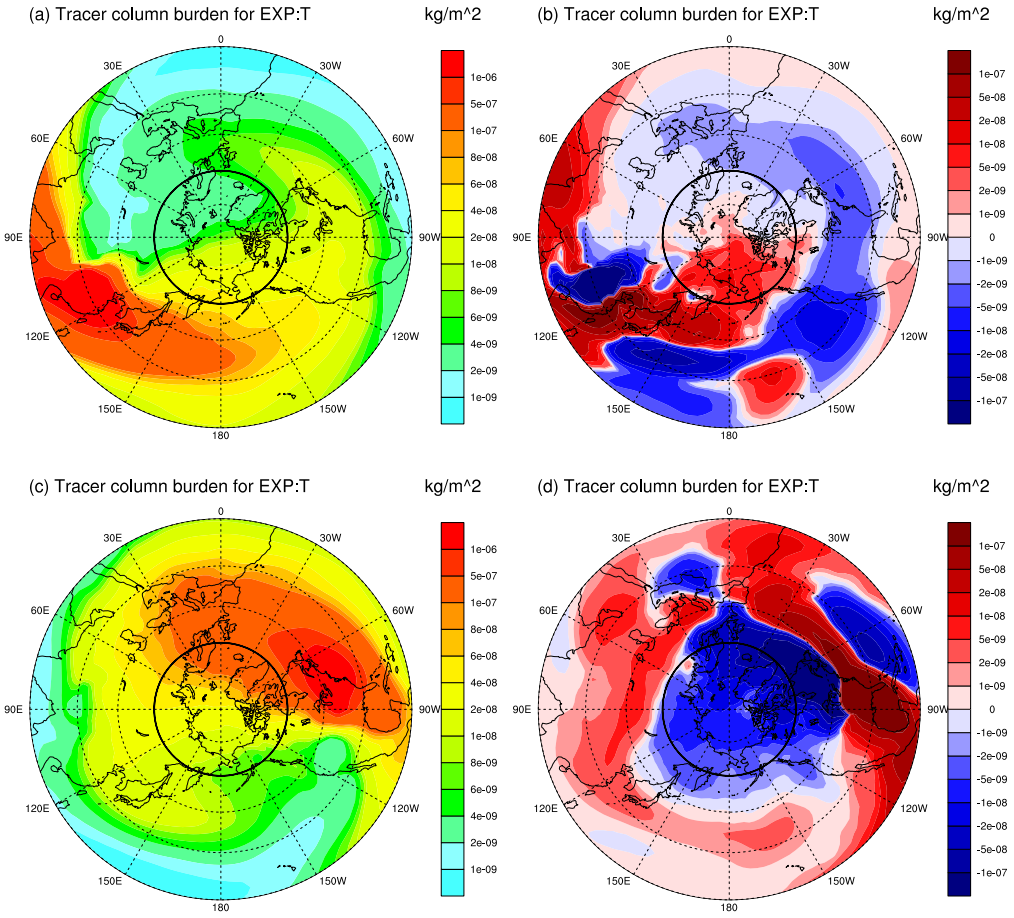

Figure 3.3: Tracer column burden distributions in EXP:T during January for (a): East Asian tracer emissions in present day climate, (b): the difference in column burden between future and present day climate (RCP–PRD) for East Asian emissions, (c): the same as (a) but for North American tracers, and (d): the same as (b) but for North American tracers. Figures show the region between 15°N to 90°N, and the bold black line indicates the 60°N circle.

to the Arctic. This indicates that these emissions transport to the Arctic mostly via the lower troposphere pathways, as shown by *Stohl* (2006). Thus these emissions are not as sensitive as the East Asian or North American tracers to changes in free troposphere dynamics.

3.4.1.2 Changing Polar Dome and its Influence on Aerosol Transport

Before studying how the mid-troposphere wind might change between the two climate scenarios, we first exam how the winter polar dome position shifts in the future. Figure 3.5 shows the January mean 500 hPa geopotential height with wind vectors and the polar dome position for present (PRD), future (RCP), and their difference. From the polar dome position we can see that the wave amplitude of the dome increases over the Bearing Sea and Alaska in the future. The geopotential height difference exhibits a dipole feature with a low pressure center near the central North Pacific and a high pressure center near Alaska and northwestern Canada. The net result is an enhanced northward wind component over this region at the 500 hPa level (*Francis and Vavrus*, 2012; *Lee et al.*, 2015). From Figure 3.3a we can see that the East Asian tracer mixes into the Arctic over the same region where the wind shifts toward the north. This shift in the wind direction favors transport of East Asian emissions to the Arctic.

One possible explanation for the extension of the meridional amplitude of the polar dome over the Bering Sea and Alaska is inhomogeneity of Arctic warming in future climate. Under the RCP8.5 scenario, by the end of the 21st century the increase of winter surface temperature is simulated to be much stronger near the Chukchi Sea and Alaska than other regions of the Arctic, at least in this model. Figure 3.6a shows the surface temperature change from present day to future climate in January. The surface temperature around Chukchi Sea ranges from –10°C to –25°C in present day climate. While most of the Arctic warms by 5 – 10°C, the area near the Chukchi Sea

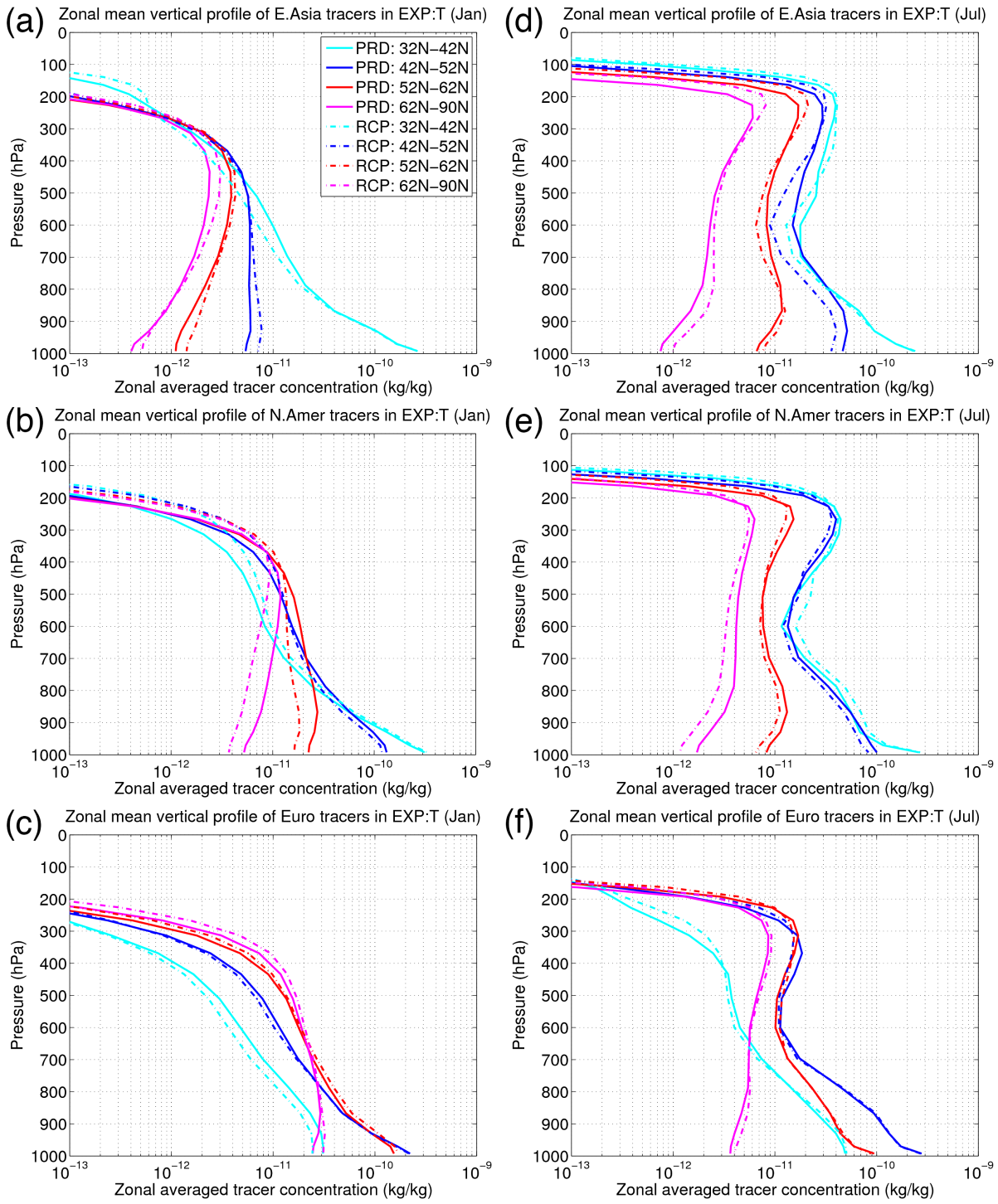

Figure 3.4: Vertical profile of zonally averaged concentration of (a): East Asian tracers in January, (b): North American tracers in January, (c): European tracers in January, (d): East Asian tracers in July, (e): North American tracers in July, and (f): European tracers in July.

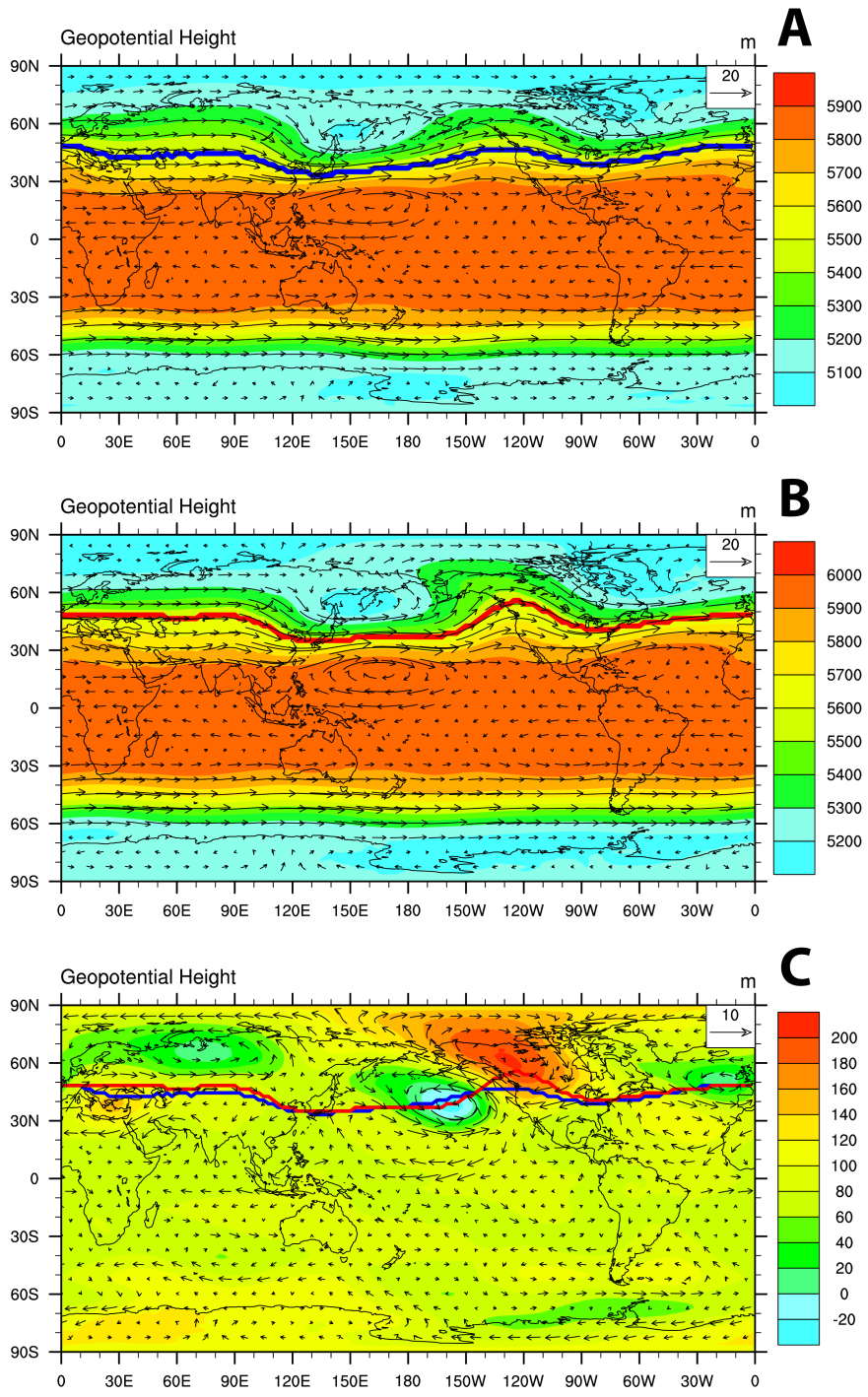

Figure 3.5: The 15-year mean January 500 hPa geopotential height and wind (units of m/s) for (a): present-day, (b): future, and (c): their difference (future – present). The bold blue and red lines depict the mean positions of the polar dome in present and future climate, respectively.

warms by 25 – 30°C in future climate. The enhanced warming of the Chukchi Sea is associated with substantial sea ice loss in this region during winter. Figure 3.6b shows the change of sea ice extent in January from present day to future climate. From the figure, we can see that the maximum sea ice loss is also in the vicinity of the Chukchi Sea. The inhomogeneity of Arctic warming and sea ice loss leads to inhomogeneity of the latitudinal temperature gradient across different longitudes. With the latitudinal temperature gradient decreasing most rapidly in the Chukchi Sea and Bering Sea region, we expect the zonal wind component of the tropospheric mid-latitude jet will become slower in this region. This, in turn, will lead to the northward extension of the polar dome boundary near the Bering Sea and Alaska.

Figure 3.3c shows that tracers emitted from North America primarily mix into the Arctic over the North Atlantic, Greenland and northeastern Canada. As the North American tracers also transport to the Arctic via high altitude pathways, they are sensitive to the change of wind at 500 hPa level over the North Atlantic. Figure 3.5c shows that the wind over the North Atlantic and northeastern Canada shifts southward in future climate. This is a net result of a high pressure anomaly over northwestern Canada and a weak low pressure anomaly over the Atlantic. The southward shift of wind inhibits the transport of North American tracers to the Arctic in future climate, opposite of the effect that occurs with East Asian tracers.

3.4.1.3 Seasonality of Tracer Transport

Figure 3.4d–f shows the vertical profiles of East Asia, North America and Europe tracers' mass concentration in July for EXP:T. The tracers' mass concentrations exhibit different vertical distributions than in January. This shows that in summer, aerosol emissions from all three source regions can transport to the Arctic via both the middle to high altitude pathways and also through low level transport. The relative importance of the high and low pathways are different in summer, however.

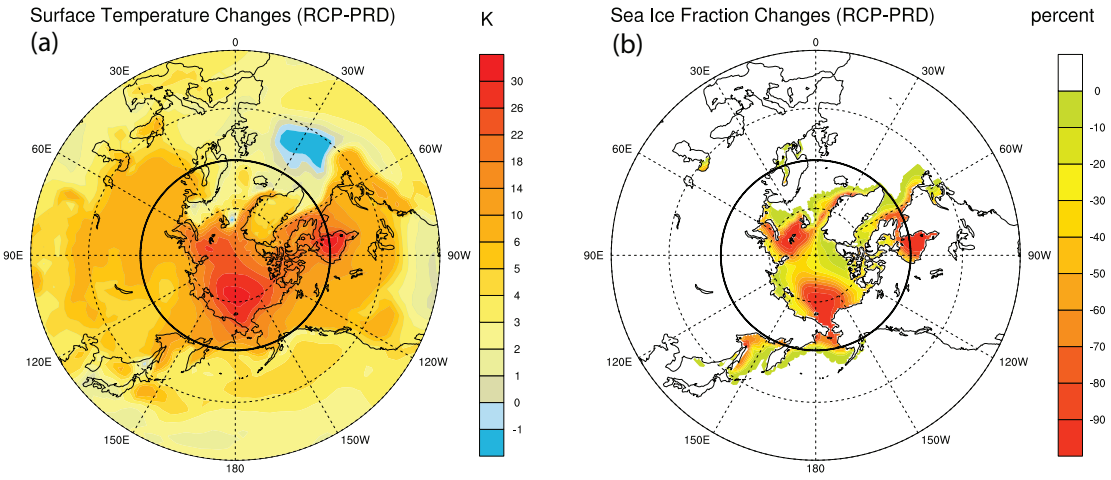

Figure 3.6: (a) January surface temperature difference between future and present climate (RCP–PRD) and (b) January Arctic sea ice extent difference (RCP–PRD). Figures show the region between 30°N to 90°N, and the bold black line indicates the 60°N circle.

The high altitude transport is still dominant for Arctic transport of East Asian and North American emissions. The altitude of maximum mass mixing ratio in the Arctic for East Asian and North American tracers elevates about 2800 m in comparison with January. For the European tracer, the Arctic mass mixing ratio also shows a maximum at high altitude, indicating high level transport from the source region. This change is caused by enhanced convection during summer, different potential temperatures between emission and receptor regions, and weakening of the polar dome and jet stream in summer (*Koch and Hansen*, 2005; *Stohl*, 2006). Figure 3.4d–f shows similar changes in Arctic burden for tracers emitted from East Asia, North America and Europe between present day and future climates. For tracers emitted during summer from East Asia, both the high and low portions of the Arctic atmosphere show increased mass mixing ratios in a warming climate. Meanwhile, we see decreased Arctic mixing ratios for North American tracers, and increased mixing ratios from European tracers.

3.4.2 Results for Experiment Transport+Deposition

3.4.2.1 Arctic Aerosol Fraction

The previous section showed that changing atmospheric dynamics associated with climate change have varying impacts on tracer transport to the Arctic. Another critical factor influencing the tracers' spatial and temporal distributions is the deposition process. In this section, we will use the same model framework to represent present day and future climates, but will use active wet and dry deposition for tracer removal processes. In EXP:T+D, the tracer is subject to the wet and dry deposition processes that it experiences during its atmospheric life cycle. The treatments of the wet and dry deposition for all the 200 tracers in this experiment are the same as the default settings for BC in BAM (*Rasch et al.*, 2000; *Barth et al.*, 2000). The SST and sea-ice distributions for present day and future climate representations are the same as

EXP:T.

Figure 3.7a shows the spatial pattern of the January Arctic aerosol fraction (AAF) in EXP:T+D, for all of the 200 tracers in present day climate. Figure 3.7a reveals that the pattern of tracers' AAF with active wet and dry deposition is very similar to that produced with constant aerosol lifetime in EXP:T. Figure 3.7b shows the AAF pattern for EXP:T+D in future climate. The general AAF pattern structure does not show dramatic changes from PRD to RCP, but the relative changes in Arctic aerosol fraction between the two climate scenarios are substantial, as shown in Figure 3.7c. From Figure 3.7c, we find that the AAF decreases significantly with climate warming for tracers emitted from almost the entire northern hemisphere mid-latitude land mass, except for a few regions in western Europe and southern Alaska. Emissions from the central and eastern parts of North America experience the strongest decreases in AAF. About 70% less of the tracers emitted from this region reside in the Arctic in future climate. This is caused by the net effects of decreasing Arctic transport as revealed by EXP:T, and increasing Arctic deposition efficiency in a warmer and wetter climate (Section 3.4.2.2). Meanwhile, for emissions from the west coast of North America, most of East Asia and Central Asia, and eastern Europe, the decrease in AAF is significant but not as substantial as that associated with emissions from central and eastern North America. This suggests that the effect on aerosol burden of more rapid Arctic deposition is partially offset by the enhanced northward transport of these emissions in future climate. The decreases in AAF for tracers emitted from most parts of Europe, Asia and western North America range from 20% to 50% in future climate.

3.4.2.2 Influence of Tracer Deposition

The distinct difference between the results from EXP:T and EXP:T+D indicates that changes in deposition are the dominant drivers of changes in the tracer burdens

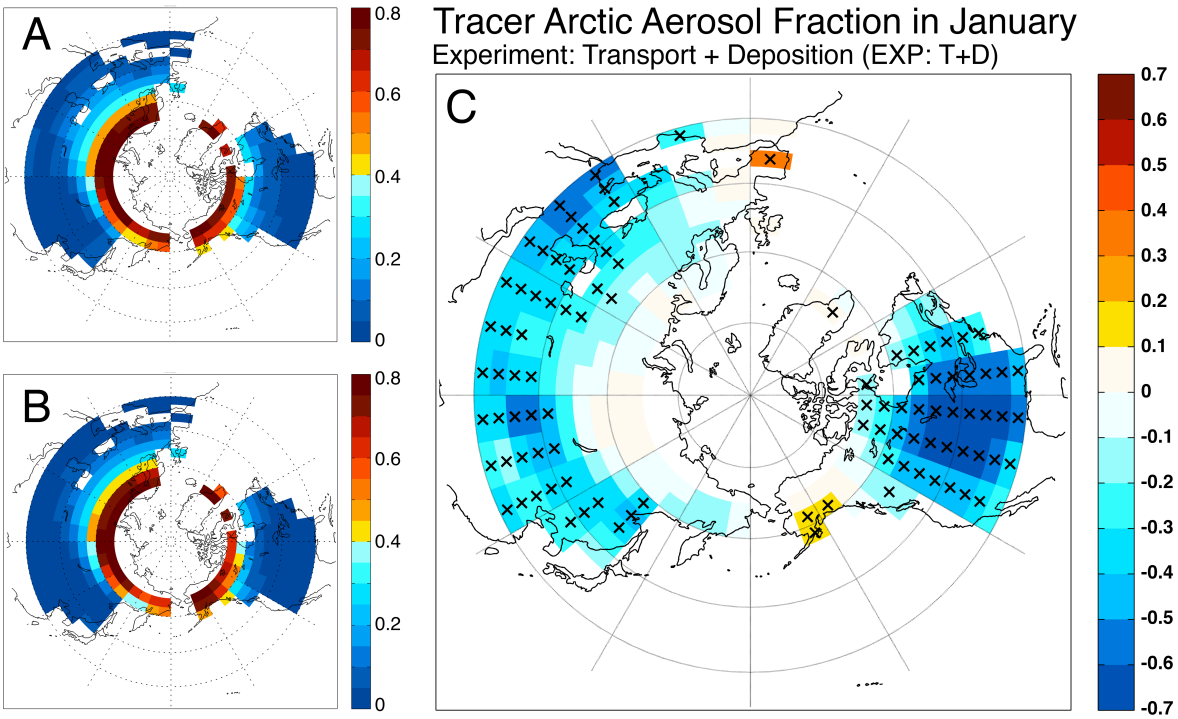

Figure 3.7: The same as Fig. 3.2 but for EXP:T+D (active transport and deposition).

with 21st century climate change. The purpose of this section is to investigate the relative changes in deposition *efficiency* from present day to future climate, as a means of identifying the regions along transport pathways that are responsible for enhanced deposition and therefore reduced Arctic aerosol burdens. Here we shift to using the additional tracer in EXP:T+D that has a simulated distribution associated with realistic BC emissions from year 2000. This tracer applies the year 2000 BC emission inventory developed with RCP8.5 scenario, with annual global emission of 7.5 Tg (*Rao and Riahi*, 2006; *Riahi et al.*, 2007, 2011). We refer to this tracer as the realistic BC tracer to distinguish it from the 200 tagged tracers analyzed in previous sections. The realistic BC tracer is subject to the same aerosol treatment as the other tagged tracers in EXP:T+D, and we use the same emission inventory in the present and future simulations presented here. As we focus here on the spatial distributions of relative changes in deposition efficiency, we are able to simply use a single global BC tracer, while retaining realistic spatial heterogeneity of BC emissions.

We use the tracer's first-order removal rate as a measure of the deposition efficiency. The first-order removal rate is defined as the tracer's total deposition rate normalized by its column burden (e.g., *Wang et al.*, 2013). This term reflects the tracer's atmospheric removal efficiency and has units of day^{-1}. Figure 3.8b shows the relative differences in the realistic BC tracer's first-order removal rate between present day and future climates in January. In the northern hemisphere, the largest relative increases in first-order removal rate are located in the Arctic and near the eastern shore of the Pacific. The Arctic mean first-order removal rate increases by 23.3% in January. This indicates that reduced Arctic aerosol burden in future climate is due more to faster removal of aerosols from the Arctic atmosphere than from reduced transport to the Arctic. This pattern is a direct result of the precipitation changes in future climate. Figure 3.9b shows the relative change in total precipitation rate from present to future climates in January. We can see that in the regions where the

relative increases in precipitation are large (like the Arctic and eastern Pacific), the tracers' deposition efficiency is also substantially enhanced. This is consistent with the fact that the majority of the tracer's removal is associated with wet deposition (e.g., *Garrett et al.*, 2010). As the Arctic removal process accelerates in future climate, the tracer's Arctic residence time and mean burden will tend to decrease. Thus, even though atmospheric circulation changes favor enhanced transport of East Asian emissions to the Arctic, the Arctic burden of these emissions will decrease due to the larger offsetting effect of increased deposition efficiency in the Arctic. By comparing the results of these two experiments, we can qualitatively state that aerosol wet deposition processes dominate the change in Arctic aerosol burden with anthropogenic climate warming.

3.4.2.3 Seasonality of Changes in Tracer Transport and Deposition

In EXP:T+D deposition becomes the dominant source of decreased AAF with climate change during winter. In July, the relative change in Arctic deposition efficiency is weaker compared to winter. From Figure 3.8c, we see that the first-order removal rate during July is enhanced near the Chukchi Sea and the east of Greenland, while decreasing over the west of Greenland and other regions in the Arctic. The regions that show substantial first-order removal rate changes in July also have large changes in precipitation rate, as depicted in Figure 3.9c. In July, the future mean Arctic first-order removal rate for the realistic BC tracer increases about 2.0% compared to present day climate.

3.4.3 Change in the Arctic BC Distribution in Future Climate

3.4.3.1 Change in BC Emission in Future Climate

In this section, we quantify changes in the Arctic BC budget in future climate due to changes in transport and deposition, as well as changes in BC emissions. We apply

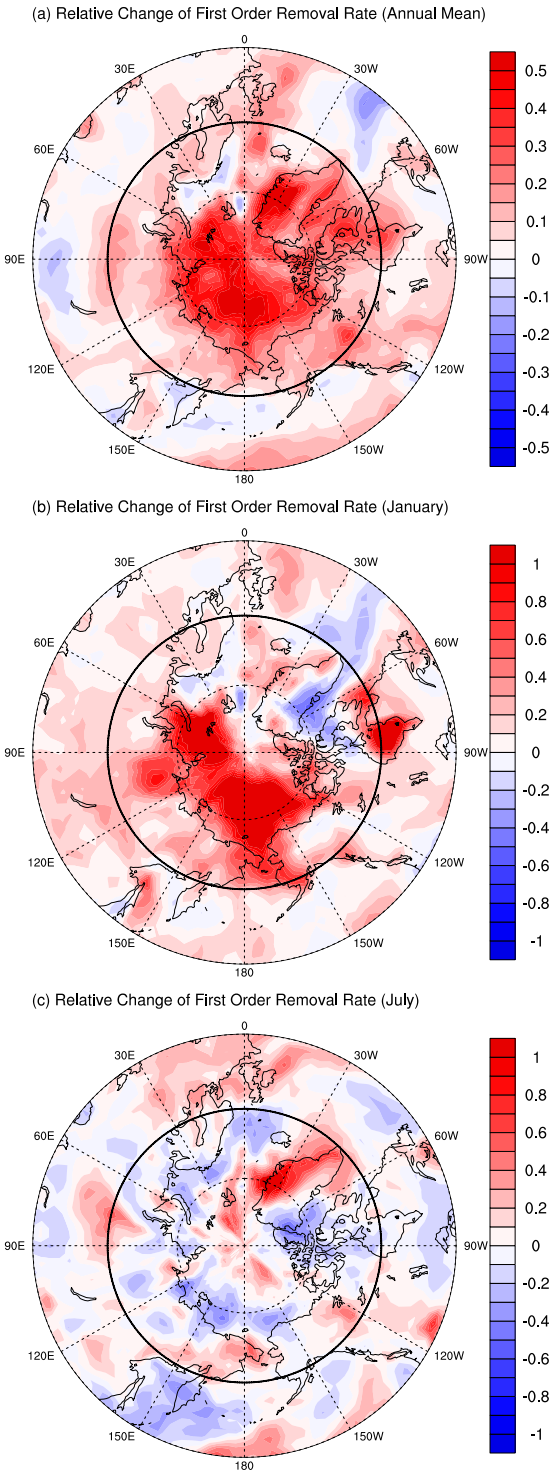

Figure 3.8: Relative change in the first order removal rate from present day to future climates ((RCP-PRD)/PRD) for present-day BC emissions during (a): annual mean, (b): January, and (c): July. Figures show the region between 45°N to 90°N, and the bold black line indicates the 60°N circle.

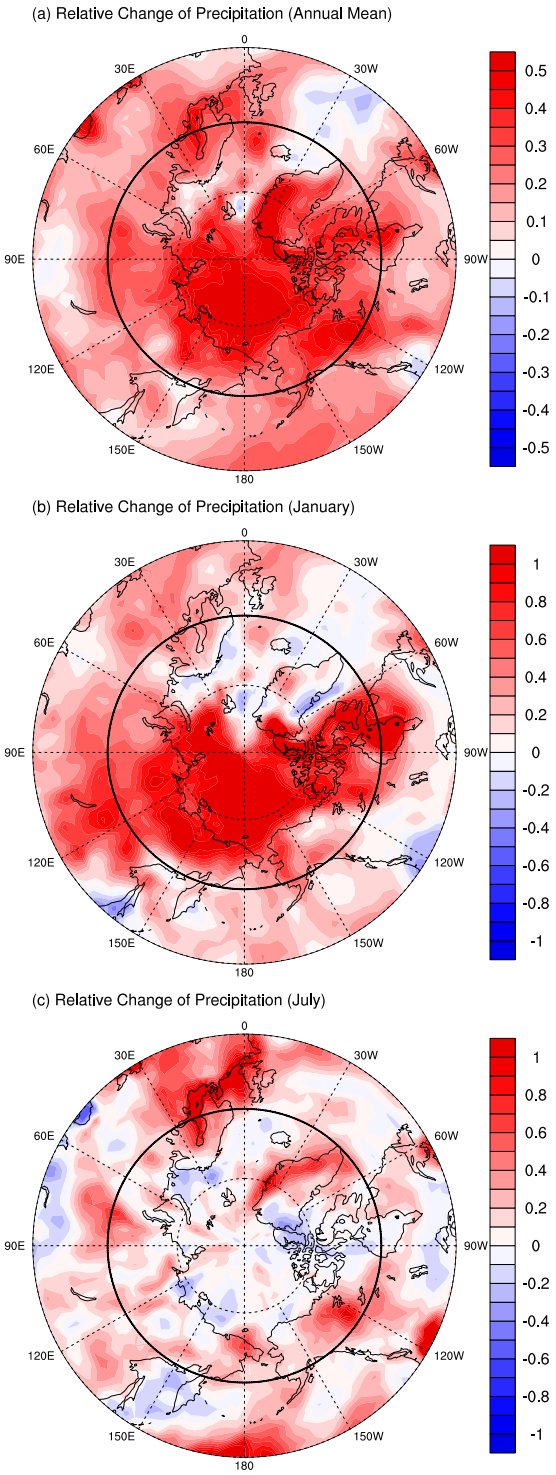

Figure 3.9: Relative change in the total precipitation rate (convective and stratiform) from present day to future climates ((RCP-PRD)/PRD) averaged over 15 years for (a): annual mean, (b): January, and (c): July. Figures show the region between 45°N to 90°N, and the bold black line indicates the 60°N circle.

model settings as in EXP:T+D with two additional tracers. One tracer represents the present day BC emission inventory (Ep) under the RCP8.5 scenario for year 2000 (*Rao and Riahi*, 2006; *Riahi et al.*, 2007, 2011). We simulate the distribution of this tracer both under present climate (EpCp) as well as future climate (EpCf). The relative changes $[(EpCf - EpCp)/EpCp]$ of this tracer's column burden inform on how the BC distribution will change solely due to changes in transport and deposition. A second tracer tracks a projected future emission inventory simulated in the presence of future climate (EfCf). The future emission inventory applies year 2100 BC emissions developed for RCP8.5 (*Rao and Riahi*, 2006; *Riahi et al.*, 2007, 2011). Table 3.1 shows the total annual global and Arctic emissions for these present day and future inventories. From Table 3.1, we can see the global annual BC emissions decrease by about 43.5% by the end of 21st century as projected by the RCP8.5 scenario. The BC emissions from 60°N to 90°N in this inventory decrease by 21.7%, but may not include realistic changes in Arctic shipping and flaring (*Corbett et al.*, 2010; *Stohl et al.*, 2013). The relative changes between EfCf and EpCp will help us quantify how the changes in emissions associated with economic and policy scenarios for the future will affect the BC distribution.

3.4.3.2 Net Change of Arctic BC Distribution

Figure 3.10 shows the relative change of the annual mean BC column burden between experiments EpCp and EpCf (panel a), and between experiments EpCp and EfCf (panel b). In both cases, there are strong reductions in the Arctic burden in future climate, though the changes are much larger when future emissions are also included. As discussed in Section 3.4.2.2, changes in deposition are a much larger contributor to the changes in Arctic aerosol distribution in future climate than changes in transport. Here we notice that regions which show large reductions in the BC column burden (Figure 3.10a) also show substantial increases in the first order

Table 3.1: Total annual global and Arctic BC emissions for present day and future emission inventories. Annual mean global and Arctic BC column burden, and Arctic deposition flux in simulations for present day emission with present day climate (EpCp), present day emission with future climate (EpCf) and future emission with future climate (EfCf).

Experiment	Global emission (Tg)	Arctic emission (kg)	Global mean column burden ($\mathrm{kg\,m^{-2}}$)	Arctic mean column burden ($\mathrm{kg\,m^{-2}}$)	Arctic mean deposition flux ($\mathrm{kg\,m^{-2}\,s^{-1}}$)
EpCp	7.52	5.49×10^{7}	2.24×10^{-7}	1.25×10^{-7}	2.73×10^{-13}
EpCf	7.52	5.49×10^{7}	2.25×10^{-7}	1.08×10^{-7}	2.75×10^{-13}
EfCf	4.25	4.30×10^{7}	1.35×10^{-7}	4.88×10^{-8}	9.56×10^{-14}

removal rate (Figure 3.8a). Table 3.1 shows that the annual mean Arctic BC column burden averaged over 60°N to 90°N decreases by 13.6% by the end of 21st century between EpCp and EpCf. Yet the change of annual mean Arctic BC deposition flux is only 0.7% between EpCp and EpCf. It indicates that in a warming climate, the annual mean BC deposition flux to the Arctic surface does not change much if the emission does not change. The increase of deposition efficiency in future climate is a more important contributor to the reduction of Arctic BC column burden other than changes in aerosol transport.

In previous sections, we showed that aerosol transport and deposition efficiencies both change in the future due to climate warming. Meanwhile, emissions will also continue to change with technological and economic developments. For example, the total global annual BC emissions decline from 7.52 Tg in 2000 to 4.25 Tg in 2100 in the RCP8.5 inventories. The reduction in BC emissions will also influence the global and Arctic BC budget. Figure 3.10b shows the relative change in BC column burden between experiments EfCf and EpCp, indicating dramatic decreases in the future when reduced BC emissions are also accounted for. The annual mean Arctic BC column burden averaged over 60°N to 90°N decreases 61.0% by the end of the 21st century due to changes in transport, deposition, and emissions. Figure 3.11 shows seasonal average of Arctic BC column burden for experiments EpCp, EpCf and EfCf. For the climate-induced changes in Arctic BC (difference between EpCp and EpCf), we notice that the reduction of Arctic BC column burden is most significant in fall and winter months because the increase of aerosol removal efficiency peaks during these seasons.

3.5 Conclusion

In this study, firstly, we use simulations with 200 tagged black carbon-like tracers in the Community Atmosphere Model version 4 (CAM4) to explore changes in atmo-

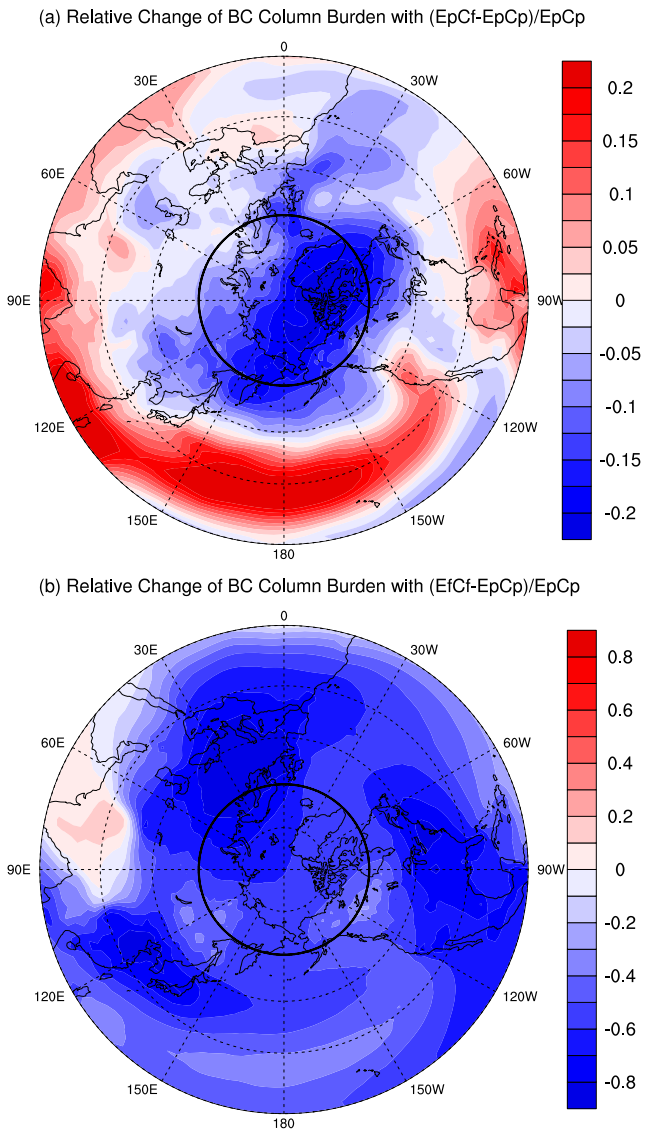

Figure 3.10: Relative change in the column burden of black carbon from present day to future climates simulated with: (a) present day emission inventory in both present day and future climates simulation (EpCf-EpCp)/EpCp, and (b) present day and projected future emission inventory for corresponding climate scenarios (EfCf-EpCp)/EpCp. Figures show the region between 45°N to 90°N, and the bold black line indicates 60°N circle.

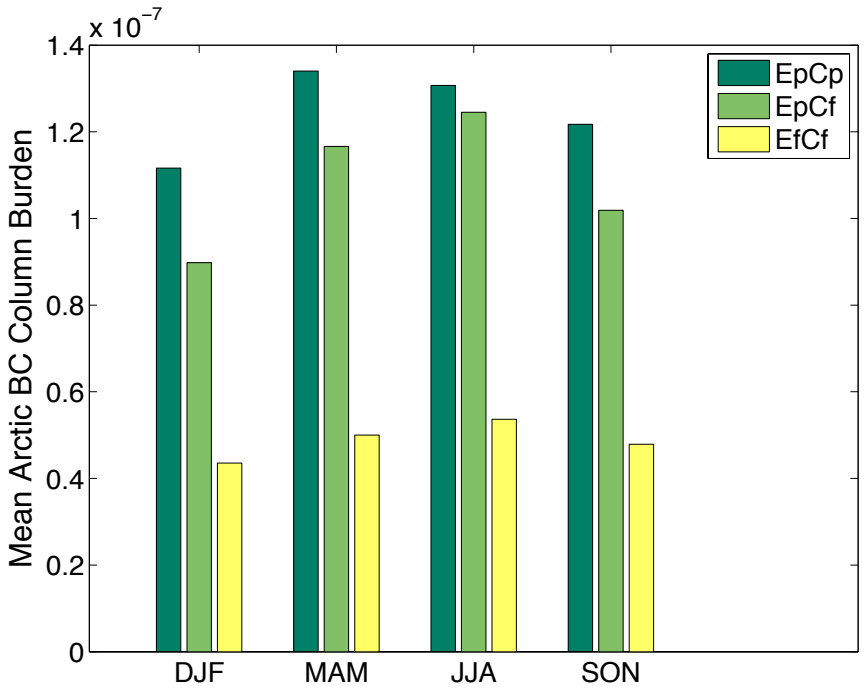

Figure 3.11: Seasonality of Arctic mean BC column burden averaged over 60°N to 90°N for experiments: EpCp, EpCf and EfCf.

spheric transport and deposition processes in the context of global climate change. We find that the poleward tracer transport efficiency for aerosols emitted during winter from East Asia will increase by about 10% – 22% in a warming climate. In particular, the meridional amplitude of the polar dome over the central and eastern Pacific will extend due to inhomogeneity in Arctic warming. This will cause the mid-tropospheric winds to shift north over the Pacific, favoring poleward transport of East Asian aerosol emissions. Meanwhile, as the mid-tropospheric wind shifts to the south over the North Atlantic and Greenland, tracers emitted from North America will experience decreased transport efficiency to the Arctic.

When we consider the combined effects of changes in transport and deposition processes, however, we find that deposition is the dominant process affecting the future Arctic tracer budget. The Arctic aerosol fraction (AAF, defined as a tracer's total Arctic burden divided by its global burden) for tracers emitted from East Asia and North America will decrease significantly in a warming climate due to more efficient wet removal in the Arctic. This results from enhanced precipitation in the Arctic, especially during winter. In simulations with present-day emissions of black carbon, enhanced wet removal reduces the Arctic annual mean black carbon column burden by 13.6% by the end of 21st century. Reduced BC emissions will likely lead to a further decrease in the Arctic black carbon burden, however, and are the leading cause of reduced Arctic BC under the RCP8.5 scenario. A simulation with combined climate changes and emissions changes under RCP8.5 shows the Arctic annual mean BC column burden decreasing by 61.0% by the end of 21st century.

CHAPTER IV

Parameter Sensitivity Study of Simulated Arctic Aerosols in CAM5

4.1 Introduction

The carbonaceous aerosols like black carbon (BC) and brown carbon (BrC) are contributors to the rapidly warming of the Arctic region (e.g., *Menon et al.*, 2002; *Hansen and Nazarenko*, 2004; *Jacobson*, 2004; *Stier et al.*, 2007; *Ramanathan and Carmichael*, 2008; *Flanner et al.*, 2009; *Bond et al.*, 2013). During the sunlit season, the darkening of snow and ice surface caused by BC increases surface solar heating and can accelerate melting of the glacier and sea ice. This process accelarates the albedo feedback in the climate system, which is an important positive climate feedback mechanisms and has profound impact on the Arctic climate and ecosystem (*Hansen and Nazarenko*, 2004; *Bond et al.*, 2013). Surface temperature response to the Arctic BC aerosol also depends strongly on its vertical distribution in atmosphere (*Flanner*, 2013). The simulated BC distributions in Chemical Transport Model (CTM) and General Circulation Model (GCM) have uncertainties related to global BC emission pattern, atmospheric transport and deposition processes, model snow and ice cover, and post-depositional transport of BC with meltwater (*Flanner et al.*, 2009; *Browse et al.*, 2012; *Bond et al.*, 2013; *Jiao et al.*, 2014).

The deposition efficiency and aerosol's atmospheric lifetime are the most important processes that govern the BC budget and distribution in high latitude region. For example, by analyzing the atmospheric BC field in AeroCom Phase I models, *Koch et al.* (2009b) found that increasing BC lifetime has a large impact on BC surface concentrations in remote regions. Meanwhile, analysis of surface measurements at Barrow indicates that the seasonality of aerosol concentration is dominated by wet deposition, rather than efficiency of transport from source regions (*Garrett et al.*, 2010; *Browse et al.*, 2012; *Lund and Berntsen*, 2012). *Garrett et al.* (2010) and *Garrett et al.* (2011) used observations to show that the seasonality of both light absorbing and light scattering aerosols are mainly controlled by wet scavenging in the Arctic. They argued that the high efficiency of aerosol removal processes in spring and summer is caused by the higher relative humidity and warm temperatures in these seasons.

Thus, improving the deposition and aerosol aging processes in GCMs that govern Arctic aerosol distributions will help us to better constrain the Arctic aerosol budget. *Liu et al.* (2011) found that the simulated Arctic BC field becomes closer to observations after adjusting the BC aging rate based on OH radical concentration, decreasing dry deposition velocity over snow and ice, and reducing wet removal efficiency in ice clouds. *Zhou et al.* (2012) showed that both the aerosol transport and wet deposition treatments in their model have strong influences on BC distributions in polar regions. *Wang et al.* (2013) improved the aerosol processes, including aerosol–cloud interactions, cloud microphysics and macrophysics, aerosol transformation, convective transport and aerosol wet removal, in the Community Atmosphere Model version 5 (CAM5). They significantly improved the comparison of BC and sulfate distribution in the Arctic with the observations, and indicated that wet removal, aerosol aging and aerosol–cloud interactions are the most important processes that control the Arctic aerosol budget.

In this study, we investigate how different physical parameterizations in the Modal Aerosol Module (MAM) in CAM5, may influence the simulated vertical distribution of Arctic BC aerosol. We conduct 15 experiments to test the sensitivity of the simulated aerosol fields to perturbations of selected aerosol process-related parameters in the Modal Aerosol Module with seven lognormal modes (MAM7), perturbed parameters include those that govern aerosol aging, in-cloud and below-cloud scavenging, aerosol hygroscopicity and dry deposition. The simulations are compared with observed aerosol vertical distributions and total aerosol extinction coefficients to assess model performance and quantify uncertainties associated with these sensitivity experiments. Observations applied here include Arctic aircraft measurements of black carbon vertical profiles from four different campaigns and total aerosol extinction coefficient observed from the CALIPSO satellite. This sensitivity study explored here will provide guidance for optimizing the aerosol simulations in CAM5.

4.2 Experiment Design

We use the Community Atmosphere Model version 5 (CAM5) coupled with MAM7 aerosol module to simulate global aerosol fields (*Liu et al.*, 2012; *Ghan et al.*, 2012). Several important improvements have already been implemented in MAM to improve the simulated Arctic BC distribution (*Wang et al.*, 2013). In this sensitivity study, we designed 15 experiments to investigate the simulated Arctic BC distribution in response to perturbed physical parameters, model resolution and different vertical treatment of emissions. Based on the time span of available observation datasets, we run the model from year 2006 to 2009. Model spin-up occurs in year 2006 and we use the remaining years for analysis. All simulations are driven by prescribed inter-annually varying sea surface temperature (SST) and sea ice fraction which represent conditions during the simulation period (*Rayner et al.*, 2003). The Control run (CTL) uses the default MAM settings along with most of the proposed parameteri-

zation improvements from *Wang et al.* (2013), but we keep the number of condensed monolayers needed for BC and Organic Matter (OM) to transfer into accumulation mode unchanged as three, which is the default setting in MAM. This parameter will be investigated further in the experiments. All the experiments prescribe the AeroCom BC emission inventory for consistency, except in the three-dimensional emission (3DE) experiment. In experiment 3DE, the model uses a vertically resolved three dimension emission inventory, which can deploy the aerosols emitted with biomass burning sources at different altitudes (*Ghan et al.*, 2012). The CTL simulation as well as all other experiments run on 1.9°x 2.5 ° resolution grid with 30 vertical layers, except that the High Resolution experiment (HiR) runs on a 0.9°x 1.25° resolution grid with 30 vertical layers. The physical parameter settings are the same for experiment CTL, 3DE and HiR.

For the other 12 experiments, we perturb six different parameters in MAM7 and study whether it improves or worsens the model's Arctic aerosol simulation. We perturb each of the parameters individually to maximum and minimum values listed in Table 4.1 based on previous theoretical work and expert judgement.

Table 4.1 lists the six parameters used in the sensitivity study, along with their perturbed values. The first four experiments (P1L, P1H, P2L and P2H) focus on the BC aging process and Primary Organic Matter (POM) hygroscopicity, which have direct impact on the BC atmospheric lifetime, because BC and POM are treated as internally mixed in MAM. In the first set of experiments, we set the number of condensed monolayers needed for BC and POM in the primary carbon mode to transfer into accumulation mode to a lower limit (P1L) of 1 layer and a higher limit (P1H) of 8 layers. This will implicitly decrease (P1L) and increase (P1H) the average BC atmospheric lifetime by changing the time needed for the aerosol to transfer into the accumulation mode and become subject to efficient wet removal process. For the second set of experiments, we directly perturb the hygroscopicity coefficient of POM

Table 4.1: Experiment design for the model sensitivity study.

Label	Parameter	Default Value	Perturbed value in the experiment
CTL	Control simulation	-	-
3DE	Emission inventory and deploy method	Surface flux	Surface flux + vertical deploy
P1L P1H	Number of condensed monolayers needed for transfer of BC and POM into accumulation mode	3	P1L: 1 P1H: 8
P2L P2H	Hygroscopicity of organic matters	0.1	P2L: 0 P2H: 0.4
P3L P3H	Scalar for efficiency of activation of entrained aerosols in convective clouds	1	P3L: 0.33 P3H: 3.0
P4L P4H	Scalar for liquid cloud fraction (in freeze-dry scheme)	1	P4L: 0.5 P4H: 2.0
P5L P5H	Stratiform in-cloud wet removal adjustment factor	1	P5L: 0.5 P5H: 2.0
P6L P6H	Scalar for dry deposition velocity over snow, sea ice and glaciers	1	P6L: 0.33 P6H: 3.0
HiR	Model resolution	1.9°x 2.5°	0.9°x 1.25°

to a lower limit (P2L) of zero and a higher limit (P2H) to 0.4 (compared to the model default value 0.1). Aerosol with larger hygroscopicity tends to experience more efficient wet removal with liquid precipitation. Thus perturbing this parameter will change the efficiency of aerosol wet removal processes and influence the aerosol atmospheric lifetime and distribution. In the next six sensitivity experiments (P3L – P5H), we perturb three different parameters related to aerosol activation and wet removal processes. The MAM incorporates a new treatment of convective transport and wet removal of aerosols, including aerosol activation at the cloud base using the scheme of *Abdul-Razzak and Ghan* (2000) and secondary activation of entrained aerosols in convective updrafts (*Wang et al.*, 2013). Parameter P3 is a scalar for the efficiency of activation of entrained aerosols above convective cloud base. This parameter controls the fraction of total aerosol activated at the cloud base and in convective updrafts. In the lower limit of P3 (P3L) we scale the total aerosol activation fraction by a factor of 0.33 and in the higher limit (P3H) we multiply it by a factor of 3.0. Here we note that the fraction of activated aerosols to total aerosols can not exceed 1. Thus in P3H the perturbed aerosol activation fraction is limited to 1. In the fourth and fifth parameter perturbation experiments, we investigate the influence of liquid cloud and stratiform cloud on aerosol's wet removal process. For the fourth parameter, we scale the total liquid cloud fraction in the aerosol calculation subroutines by a factor of 0.5 (P4L) and a factor of 2.0 (P4H). This adjustment will decrease or increase the total liquid cloud amount for aerosol scavenging and wet removal calculations. This places a direct control on aerosol's wet removal rate in the model. In the fifth set of parameter perturbation experiments, we adjust the stratiform in-cloud wet removal efficiency with a scalar of 0.5 for the lower limit scenario (P5L) and a scalar of 2.0 for higher limit scenario (P5H). In the last experiment, we perturb the aerosol's dry deposition velocity over snow, sea-ice and glaciers. In these experiments, we adjust the aerosol's dry deposition velocity over snow and ice by a factor of 0.33 (P6L) and 3.0 (P6H).

The motivation for the experiments with dry deposition velocity is that with default MAM7 settings, the simulated BC dry deposition velocity over snow and sea ice is much larger than the observations. The observed aerosol dry deposition velocity over snow and ice ranges generally from 0.02 to 0.06 $\mathrm{cm\,s^{-1}}$ (*Duan et al.*, 1988; *Nilsson and Rannik*, 2001; *Gallagher et al.*, 2002; *Contini et al.*, 2010), while the simulated dry deposition velocity over snow and ice ranges from 0.08 to 0.20 $\mathrm{cm\,s^{-1}}$ in the control simulation. This bias is particularly predominant over sea ice in the winter. These experiments (P6L and P6H) will help inform us whether the uncertainty of aerosol's dry deposition rate will have a potential impact on the simulated aerosol field.

4.3 Observation Data

4.3.1 Aircraft Measurement Campaigns

Since the simulated Arctic vertical distribution of BC aerosol is the primary focus of this study, we use the BC measurements collected from several aircraft observation campaigns to evaluate the model's performance. The data collected from these campaigns measure the vertical profile of BC concentrations in different regions. Here we apply the data from four aircraft measurement campaigns, which are:

(1) The NASA Arctic Research of the Composition of the Troposphere from Aircraft and Satellites (ARCTAS) mission (*Jacob et al.*, 2010).

(2) The Aerosol, Radiation, and Cloud Process affecting Arctic Climate (ARCPAC) campaign (*Brock et al.*, 2011).

(3) The Polar Airborne Measurements and Arctic Regional Climate Model Simulation Project (PAM-ARCMIP) (*Stone et al.*, 2010).

(4) The High-performance Instrumented Airborne Platform for Environmental Research Pole-to-Pole Observations (HIPPO) (*Schwarz et al.*, 2010; *Wofsy et al.*, 2011; *Kipling et al.*, 2013; *Wang et al.*, 2014b).

The ARCTAS and ARCPAC campaigns collected BC measurements over the Alaskan Arctic and Western Canada during the spring and summer months in year 2008 (*Jacob et al.*, 2010; *Brock et al.*, 2011). All of the four campaigns used a Single Particle Soot Photometer (SP2) and a Two Particle Soot Absorption Photometers (PSAP) to take in-flight measurements of BC atmospheric concentration and the spectral light absorption coefficient. The SP2 measures the BC mass by determining the mixed particle size and non-BC coating using the scattering signal of a laser induced incandescence at 70-700 nmwavelength. The PSAP quantifies the spectral light absorption coefficient of the total and submicron absorptive aerosol, such as BC, at the wavelengths of 450nm, 550nm and 660nm. The PAM-ARCMIP focused on the BC profile over the central Arctic during April 2009 (*Stone et al.*, 2010). The HIPPO campaign conducted in-flight measurements of a variety of atmospheric compositions and covered large areas of the Pacific Ocean and High latitude regions in both hemispheres (e.g., *Schwarz et al.*, 2010; *Wofsy et al.*, 2011; *Kipling et al.*, 2013). The available observation data from the HIPPO campaign covers the Arctic, middle latitude region and the tropics. The flight tracks of the four aircraft measurement campaigns are shown on Figure 4.1. We only use the data collected during year 2008–2009 as we currently lack computational and storage resources to expand the simulations to a longer period.

4.3.2 CALIOP Satellite Lidar Measurement

As our primary goal is to improve the simulation of vertical distribution of BC aerosol in the Arctic, the perturbed parametrization experiments may reduce the model's bias in the high latitude region at the expense of worsening the global simulation especially near the emission source regions. To investigate whether a particular parameter perturbation may result in larger aerosol bias in other regions, we use a well-calibrated vertical aerosol extinction coefficient observation product from

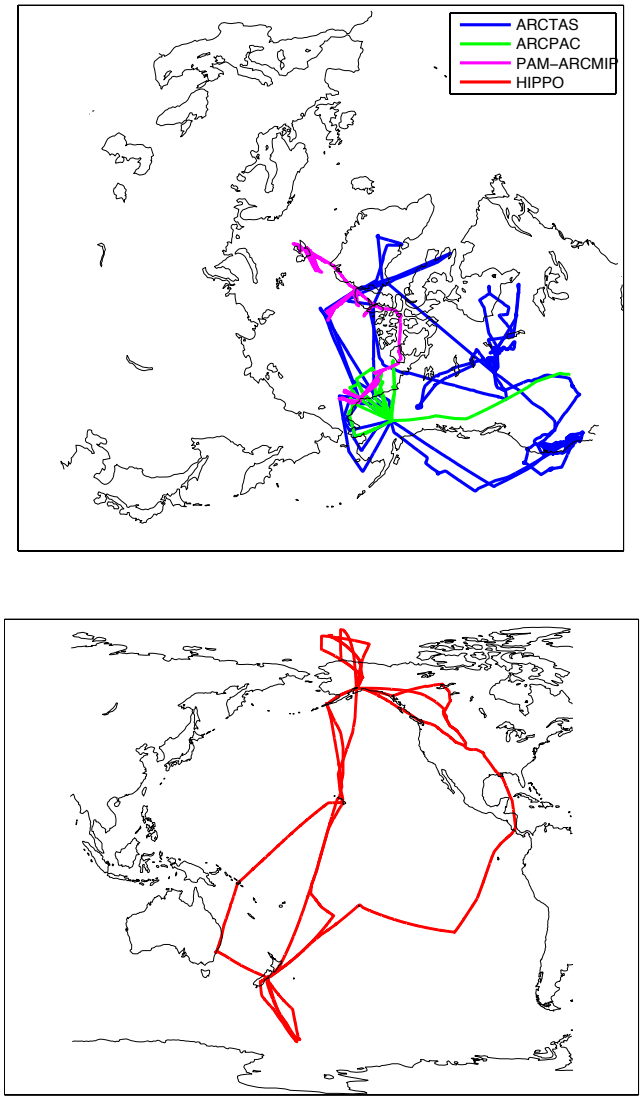

Figure 4.1: Flight tracks of the ARCTAS, ARCPAC, PAM-ARCMIP (upper panel) and HIPPO (lower panel) campaigns.

the CALIPSO (Cloud-Aerosol Lidar and Infrared Pathfinder Satellite Observations) satellite, which has a much greater temporal and spatial coverage compared to the aircraft measurements. The CALIOP (Cloud-Aerosol Lidar with Orthogonal Polarization) is a Lidar equipment onboard the CALIPSO satellite. The CALIPSO satellite can measure the profile of vertical distribution of aerosols and optically thin clouds (*Winkeri et al.*, 2010). It provides attenuated back scattering data at 532 nm and 1064 nm for continuous global aerosol vertical profile measurements. Here we follow the same model evaluation procedure to compare the simulations with CALIOP data as proposed by *Koffi et al.* (2012). The CALIOP Layer Product version 3.01 is used to evaluate the simulations with different experiment designs. We adopt the climatology of the aerosol vertical distribution in the troposphere (0 – 10 km) averaged over years 2007 – 2009. This dataset is derived by *Koffi et al.* (2012) and provided by the AeroCom (Aerosol Comparisons between Observations and Models) community (http://aerocom.met.no/databenchmarks.html).

Koffi et al. (2012), split the CALIOP data into 13 sub-continental regions which have widely-varying ratios of industrial, dust and biomass burning pollution sources. These regions are selected because of their different emission source characteristics. Among them, Eastern United States (EUS), West Europe (WEU), Eastern China (ECN), and Indian Subcontinent (IND) represent the source regions of industrial pollution. North Africa and Arabian Peninsula (NAF) and Western China (WCN) represent large source regions of mineral dust. Central Atlantic Ocean (CAT), North Atlantic Ocean (NAT) and Northwestern Pacific Ocean (NWP) are chosen to represent regions influenced by marine aerosols and the outflows of major dust and industrial pollution sources. Southern Africa (SAF), Central Africa (CAF), South America (SAM) and Southeastern Asia (SEA) are regions dominated by biomass burning emissions (*Yu et al.*, 2010; *Koffi et al.*, 2012). The exact location of each region is plotted in Figure 1 from *Koffi et al.* (2012). We adopt the same definitions

of these regions here.

4.4 Results

Here we assess the simulated aerosol fields with three different analyses. Firstly, we investigate how the annual and seasonal Arctic mean vertical distribution of BC aerosols response to different parameter perturbations in Section 4.4.1. Then, we compare the simulated BC vertical distributions with aircraft measurements collected from four campaigns in Section 4.4.2. The comparison with in-flight Arctic BC measurements is the primary focus of this study and serves as a benchmark to evaluate the effects of individual experiment. Lastly, in Section 4.4.3, we compare the simulated total aerosol extinction with satellite observations at various regions globally in order to assess the degree of perturbation each experiment introduced to global aerosol field.

4.4.1 Sensitivity Study of BC Vertical Profile in the Arctic Region

In this section, we investigate how different parameter perturbations affect the Arctic mean vertical distribution of BC concentrations. It provides a preliminary assessment of the relative influences of different processes, prior to our evaluation of model results subsampled to the observational domains. Figure 4.2 shows the Arctic annual mean vertical profile of simulated BC atmospheric concentration. For this figure as well as for the following analyses, we define the Arctic to be the region between 67°N and the north pole. This domain excludes major anthropogenic or biomass burning emission sources, allowing us to study how these experiments may influence aerosol transport and deposition in remote regions. From Figure 4.2 we can see that several parameters have significant influences on the simulated BC concentration, especially in the middle to high altitude atmosphere. Experiments P2L, P3L, P4L and P5L show significant increase of simulated BC concentrations in the Arctic.

All of the above experiments aimed to directly or indirectly reduce or slow the BC wet deposition process in the model. For example, in P2L we set the hygroscopicity of POM to zero. In MAM, BC is internally mixed with other aerosols like sulfate, Secondary Organic Matters (SOM), POM and sea salt in the primary carbon mode and accumulation mode. Thus reducing the hygroscopicity of POM will decrease the efficiency of aerosols in both modes to be removed by wet deposition. Decreasing the hygroscopicity of POM also slows the transfer of BC and POM from the primary carbon mode to the accumulation mode. Experiment P4L scales the total liquid cloud fraction by a factor of 0.5 in the aerosol calculation subroutines. As the wet deposition is the most important aerosol removal process and dominates the aerosol distributions in the Arctic (e.g., *Garrett et al.*, 2010; *Browse et al.*, 2012; *Lund and Berntsen*, 2012; *Jiao et al.*, 2014), reducing the total liquid cloud amount appears to have the strongest effect in increasing the simulated BC burden in the Arctic. As shown in Figure 4.2, experiment P4L results in about five to six fold increase in BC concentration between 700 hPa to 300 hPa altitude. In contrast, experiment P4H shows the lowest simulated BC concentrations in the Arctic among all the experiments, which again demonstrates that the total liquid cloud fraction, which controls the wet removal process of aerosol, is a first order control of the aerosol burden in remote region. For experiment P5L, in which we reduce the stratiform in-cloud wet removal by a factor of two, the simulated BC concentration roughly doubles in the Arctic. Meanwhile, experiment P5H shows a decrease of BC amount in the Arctic, due to enhanced wet removal in stratiform clouds.

As shown in Figure 4.2, other experiments exhibit little changes in the annual mean BC concentration profile, which indicates they may only pose secondary effects compared to wet removal process in this model. Perturbing the number of condensed monolayers needed for BC to transfer into the accumulation mode only shows a marginal effect on the simulated Arctic BC vertical distribution. As shown

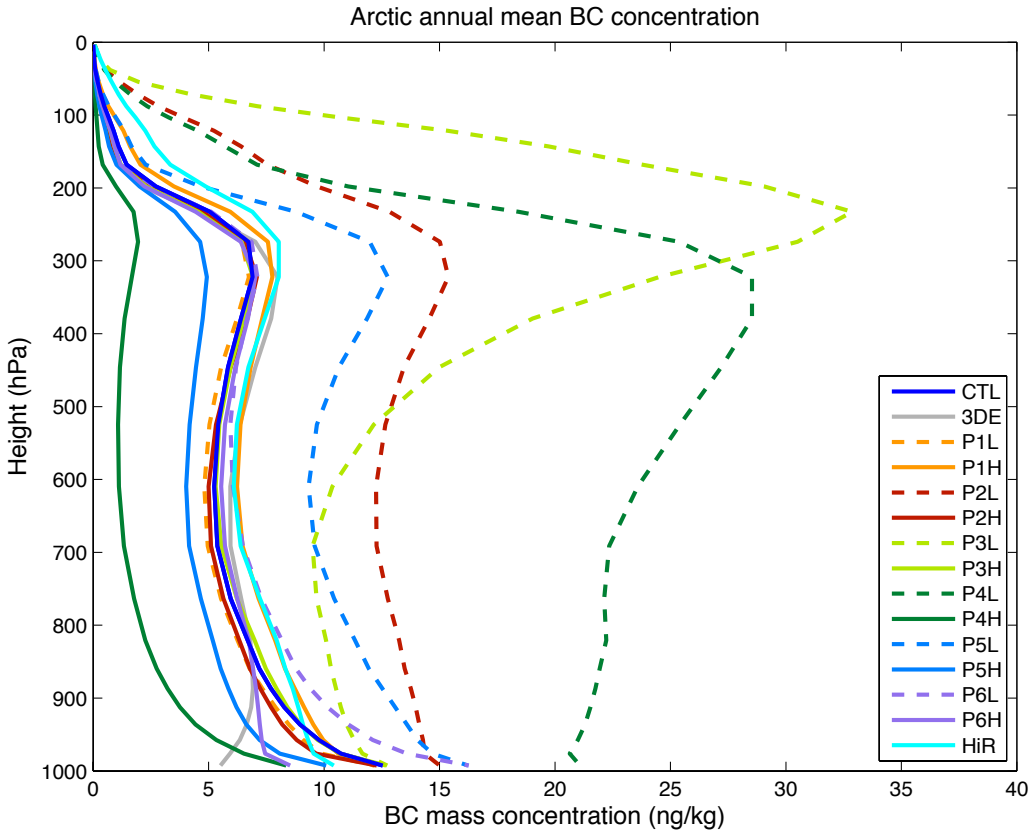

Figure 4.2: The annual mean vertical profile of atmospheric BC mass concentration for different experiments, averaged over the Arctic region (67°N– 90°N). Experiment labels are listed in Table 4.1.

in *Liu et al.* (2012), by increasing the number of condensed monolayers from the default value of 3 to 8, the global BC lifetime and the fraction of BC in primary carbon mode are significantly increased. Yet here we only see a slight increase of BC concentration in the Arctic associated with this change in isolation. The deployment of a three-dimensional vertical resolved emission inventory for biomass burning sources also shows limited effects. We do see a marginal increase in middle to high altitude BC concentration but the magnitude is small. This experiment (3DE) also shows a decrease of near surface (900 – 1000 hPa) BC concentration, which might be partially caused by inconsistences between the surface emission inventory used in CTL and 3DE. The run conducted at 1° resolution (Experiment HiR) gives a slight difference in the annual BC vertical profile in the Arctic, but the change is relatively small.

Figure 4.3 and Figure 4.4 shows the vertical profiles of Arctic BC concentration averaged during winter months (DJF) and summer months (JJA) respectively. Those two figures show very similar results as Figure 4.2, especially for the relative change of BC concentration in each experiment compared to CTL. In both winter and summer seasons, the parameters associated with wet removal processes exhibit a dominate effect on Arctic BC concentration, especially in the middle to high altitude troposphere. For the run with 1° horizontal resolution, though it shows limited changes in Arctic BC concentration in winter season, it results in a substantial increase of BC concentration in summer season, especially in the lower troposphere (700–900 hPa).

Figure 4.5 shows the global annual mean of simulated BC vertical profile. Since our focus is on improving simulated BC distribution in the Arctic, the analysis of the global mean is not our primary focus. Yet we still want to characterize how different parameter settings may alter the BC simulation field as well as other aerosols globally, in order to see whether an improvement in the Arctic may lead to reduction of the model's performance in other regions. From Figure 4.5, we can see that with the exception of experiment P3L, all other experiment do not show substantially

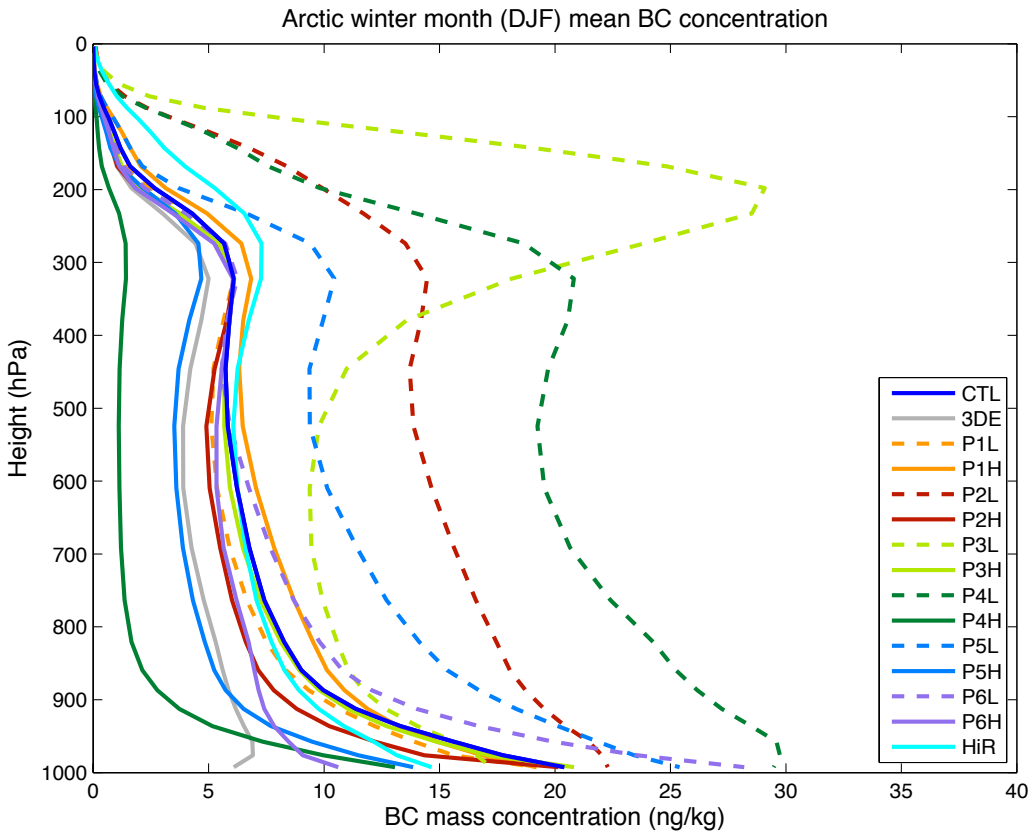

Figure 4.3: The same as Figure4.2, but averaged in winter months (DJF).

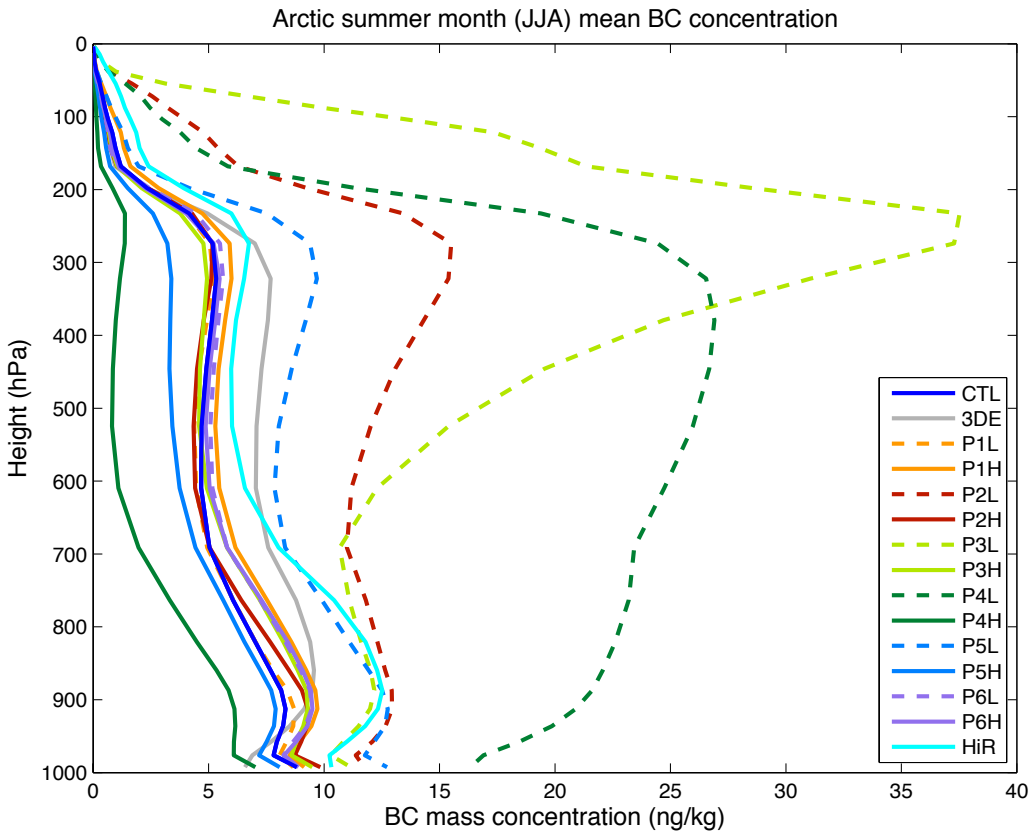

Figure 4.4: The same as Figure4.2, but averaged in summer months (JJA).

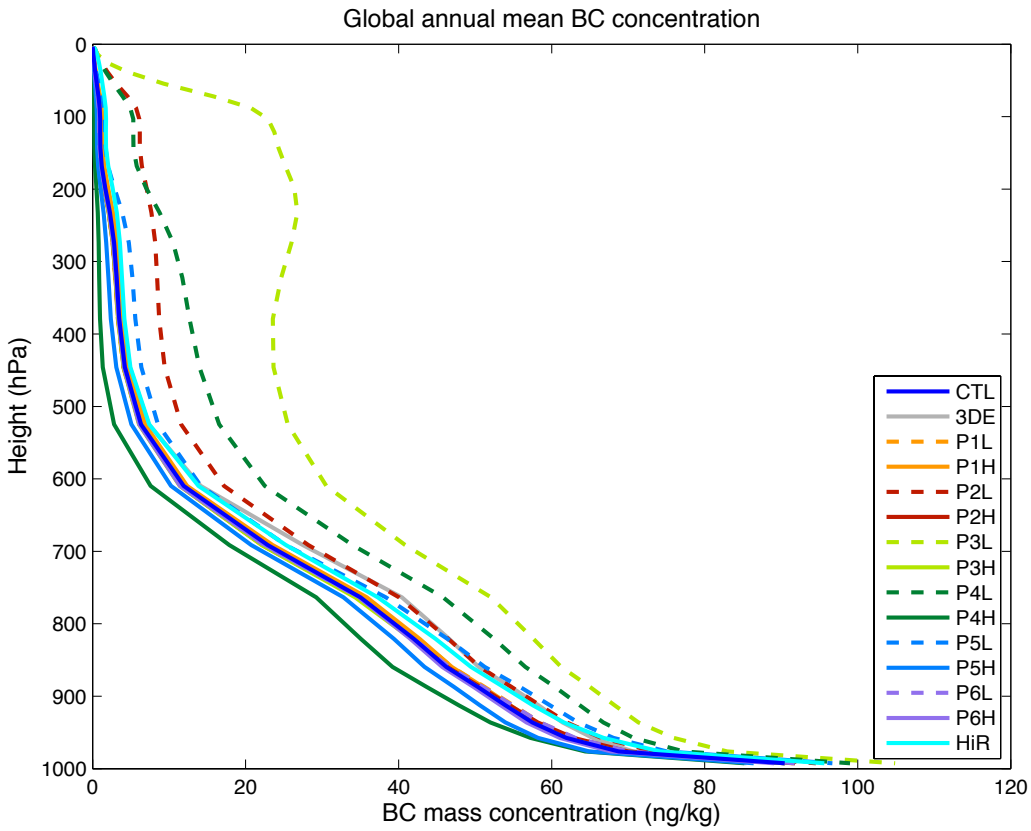

Figure 4.5: The global annual mean vertical profile of atmospheric BC mass concentration for different experiments. Experiment labels are listed in Table 4.1.

different results compared to the CTL simulation. For experiment P3L, Figure 4.5 shows that the BC concentration increases substantially in the middle to high altitude troposphere globally, and the concentration boost is about an order of magnitude near the tropopause. This indicates that we would need to be very cautious in tuning this parameter to achieve reasonable Arctic BC distributions, as it may dramatically disturb the global aerosol field. Since the results from other experiments do not show such dramatic changes, parameters perturbed in those experiments may hold greater promise for realistically improving the Arctic BC simulation fields. In Section 4.4.3 we will explore this further by comparing the simulated aerosol extinction coefficient with CALIOP measurements.

4.4.2 Comparison between Simulated BC Vertical Profile and Aircraft Measurements

Several aircraft surveys have been carried out during the last decade to provide a better observation of the vertical distribution of trace gases and aerosols. Here we use the observations of BC atmospheric mass concentrations from four aircraft campaigns (ARCTAS, ARCPAC, PAM-ARCMIP and HIPPO) to compare with the simulated BC fields. Figure 4.6 – Figure 4.10 show the comparison between simulated BC mass mixing ratio averaged over the grid cells matching the time (in precision of the exact hour when the measurement is recorded), location and altitude of measurements from each campaign. For the ARCTAS, ARCPAC and PAM-ARCMIP we focus our analysis on the Arctic region since these campaigns targeted high latitudes. We only use measurements which were taken north of 67°N for the Arctic comparison, consist with our definition of the Arctic region used previously in our study. The HIPPO campaign conducted atmospheric trace gas and aerosol measurements over a much greater domain, spanning the tropics to high latitudes in both hemispheres. Thus we take advantage of the large sampling domain of the HIPPO dataset and compare both the Arctic measurements and global measurements with our simulations. For the Arctic analyses, we exclude measurements that shows a BC mass mixing ratio greater than $1000\,\mathrm{ng\,kg^{-1}}$, since such measurement are likely influenced by local emission sources or strong pollution plumes that are unresolved in the model.

Figure 4.6 and Figure 4.7 show the comparisons results with ARCTAS and ARCPAC campaign measurements respectively. The ARCTAS and ARCPAC campaigns specifically targeted pollution plumes, and their sampling locations are more likely to represent air masses which are polluted with biomass burning emissions. The measurements in the ARCPAC dataset were strongly affected by early-season biomass burning in April 2008, as almost all of the samples in the ARCPAC campaign were collected in that month (*Warneke et al.*, 2010; *Brock et al.*, 2011). This biomass burn-

ing signal is revealed in Figure 4.7. We can see that measurements in the ARCPAC dataset show relatively large BC concentrations; almost an order of magnitude larger than the profiles in other campaigns. Thus even if the model fails to simulate the BC vertical profile observed in the ARCPAC campaign, we cannot solely blame the model parameterization or settings, because a GCM with 1° to 2° grid resolutions is not designed to resolve such fine scale biomass burning plumes. In the ARCTAS dataset, there still exists a maximum in BC concentration at 500–600 hPa with a peak BC mass concentrations of about 70 $\mathrm{ng\,kg^{-1}}$. Yet we see that the measurements in this dataset show much smaller values compared to the ARCPAC campaign. The BC measurements from the PAM-ARCMIP (Figure 4.8) and HIPPO (Figure 4.9) campaigns show smaller BC concentrations which are more representative of the remote atmosphere, as these two campaigns did not target biomass burning pollution plumes.

The results from the model and observation comparison (Figure 4.6 – Figure 4.9) indicate that the control run (CTL) with default model configuration fails to capture the observed Arctic BC vertical profile. In all four comparison plots, the simulated BC concentrations in CTL are a factor of two to ten smaller than the aircraft measurements. In order to reduce the bias of simulated BC concentration, we perturb parameters governing aerosol atmospheric lifetime, wet removal efficiency and dry deposition velocity in the model as described in Section 4.2. From Figure 4.6 to Figure 4.9, the comparisons show that the simulated BC concentration increases substantially in those experiments which aim at prolonging BC atmospheric lifetime and reducing wet deposition efficiency (i.e. experiment: P1H, P2L, P3L, P4L and P5L). Figure 4.6 shows a significant reduction of the deviation between simulation and observations for both experiments P1H and P4L. Figure 4.7 also indicates experiments P1H and P4L perform better compared to other experiments, yet still have large negative biases due to this campaign targeting biomass burning plumes. This result

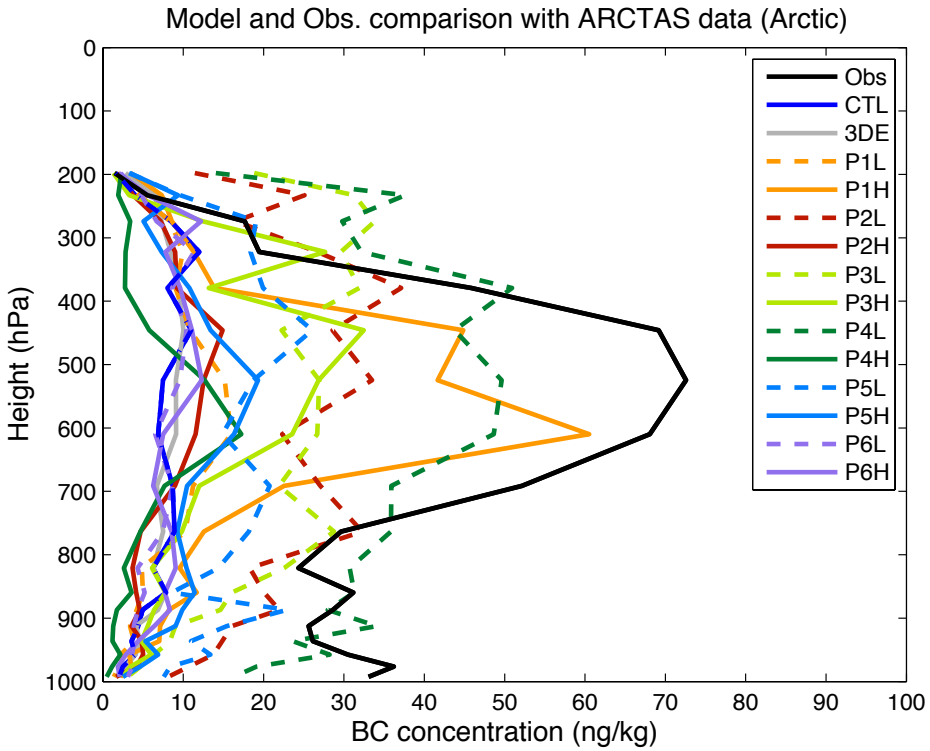

Figure 4.6: Comparison of simulated BC vertical profiles for different model experiments, with the ARCTAS campaign measurements. We extract the simulated BC concentration at the exact location, altitude and time as the measurement was collected for accurate comparison. The profiles are averaged over all samples collected within the Arctic region (67°N– 90°N).

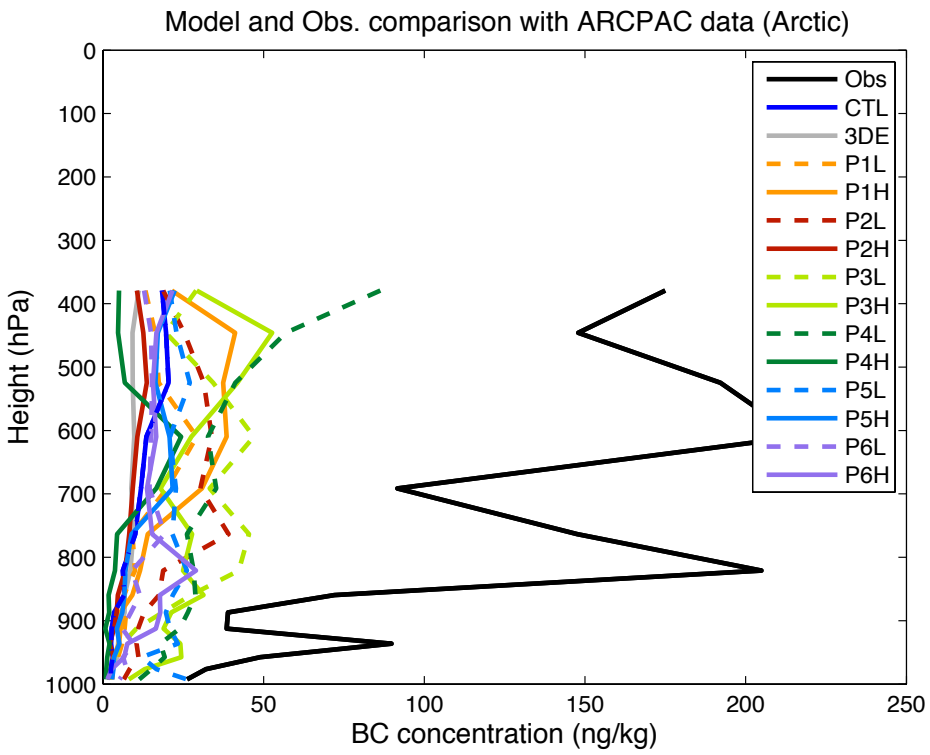

Figure 4.7: The same as Figure.4.6, but for the ARCPAC campaign.

indicates that slowing the BC aging process or decreasing the total liquid cloud fraction in the model could enhance long range BC transport to the Arctic and boost the BC concentration in the middle altitude region (400 – 700 hPa).

As shown in Figure 4.8 and Figure 4.9, the results from experiments P2L and P4L are closer to the observations compared to other experiments. The simulated BC field consistently shows increasing concentrations in the middle to upper troposphere in experiment P4L, which suggests that by directly reducing the liquid cloud content we can improve the model result in the Arctic. We also notice that when the aerosol activation efficiency is decreased in convective clouds, the BC concentration near the tropopause increases dramatically as shown in Figure 4.2, Figure 4.9 and Figure 4.10, whereas measurements to not indicate local maximum of this altitude. It may indicate that we need to be very cautious when tuning this parameter. For other parameter sensitivity experiments, the improvements compared to the control

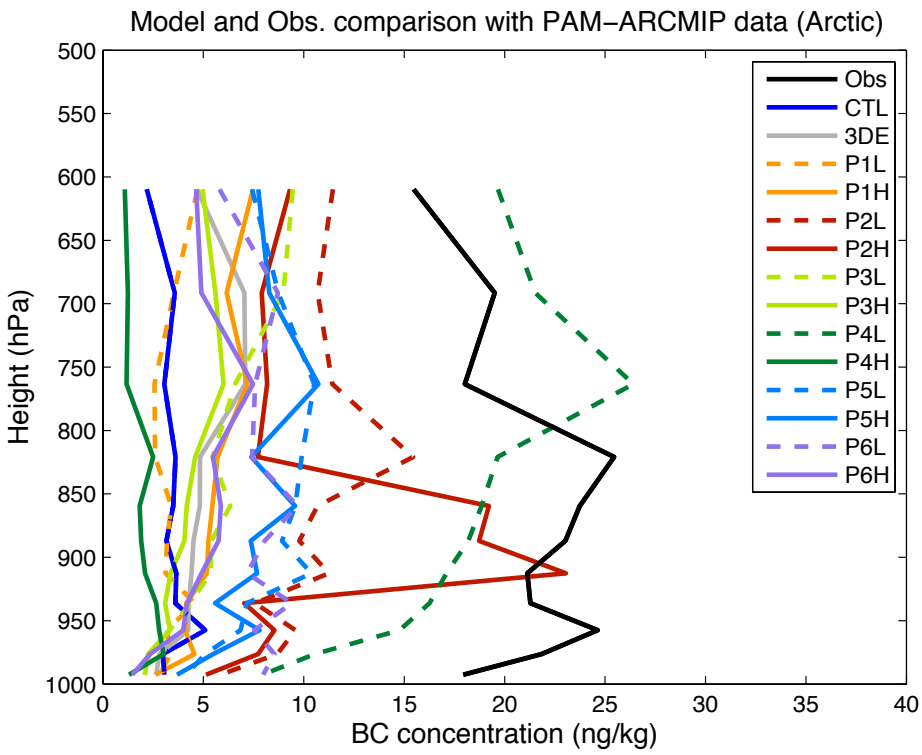

Figure 4.8: The same as Figure.4.6, but for the PAM-ARCMIP campaign.

run are not as substantial and consistent as the parameters mentioned above. This indicates that the aerosol atmospheric lifetime and wet deposition processes are the most important factors controlling the Arctic distribution. We suggest that further model improvement should focus on these two processes.

Figure 4.10 shows the results from different experiments to all available HIPPO measurements across the globe. Figure 4.10 shows experiments P2L, P3L and P4L simulate quite unrealistic increases of BC concentration in the middle to upper troposphere (200–600 hPa), with their maximum concentration ranges between 20 ng $kg^{-1}$and 30 ng kg^{-1}. While all other experiments show quite small biases compared to the measurements, which implies that even though tuning the parameters associated with wet removal processes may improve the modeling results in the Arctic, the simulated global mean BC concentration may become unrealistic high. Thus we need to further investigate how to tune these parameters for consistent improvement in the simulated

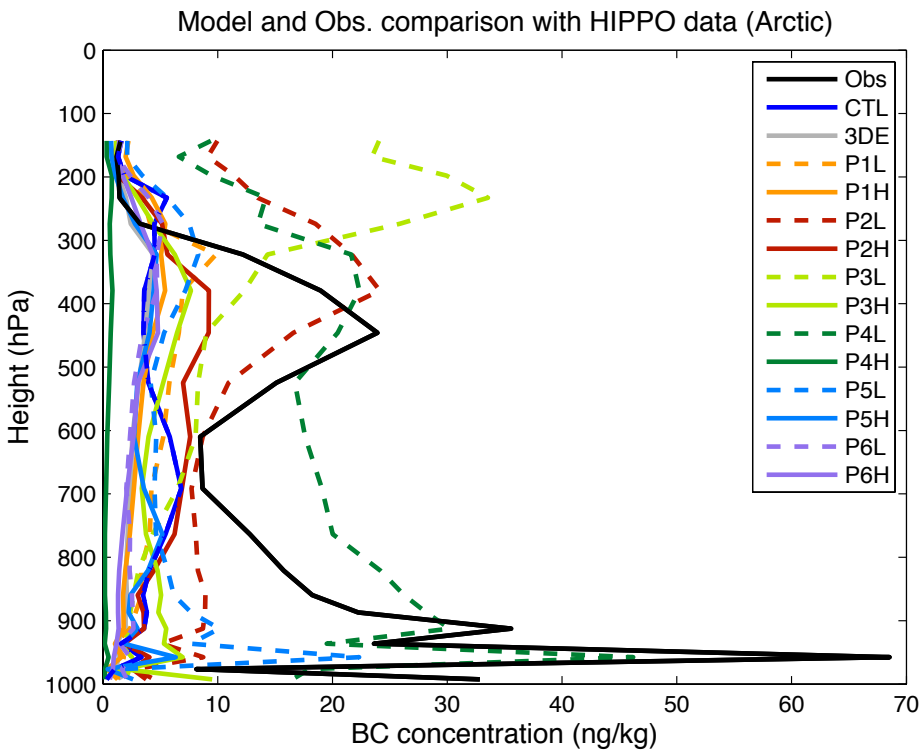

Figure 4.9: The same as Figure.4.6, but for the HIPPO campaign.

BC field.

4.4.3 Comparison between Simulated Aerosol Extinction and CALIOP Measurements

In this section we use the vertically resolved total aerosol extinction coefficient observed from CALIPSO satellite to evaluate the performances of different sensitivity experiments in terms of simulated total aerosol extinction in different regions. This comparison provides a holistic estimate of whether certain experiments may suffer from regional biases due to parameter perturbation. Figure 4.11 shows the comparison between models and observations in 13 different regions defined by *Koffi et al.* (2012). Note the Arctic region is not included in this comparison (*Koffi et al.*, 2012). In all regions, the simulated aerosol extinction coefficient vertical profiles from most experiments agree quite well with observations. A partial reason for this is that

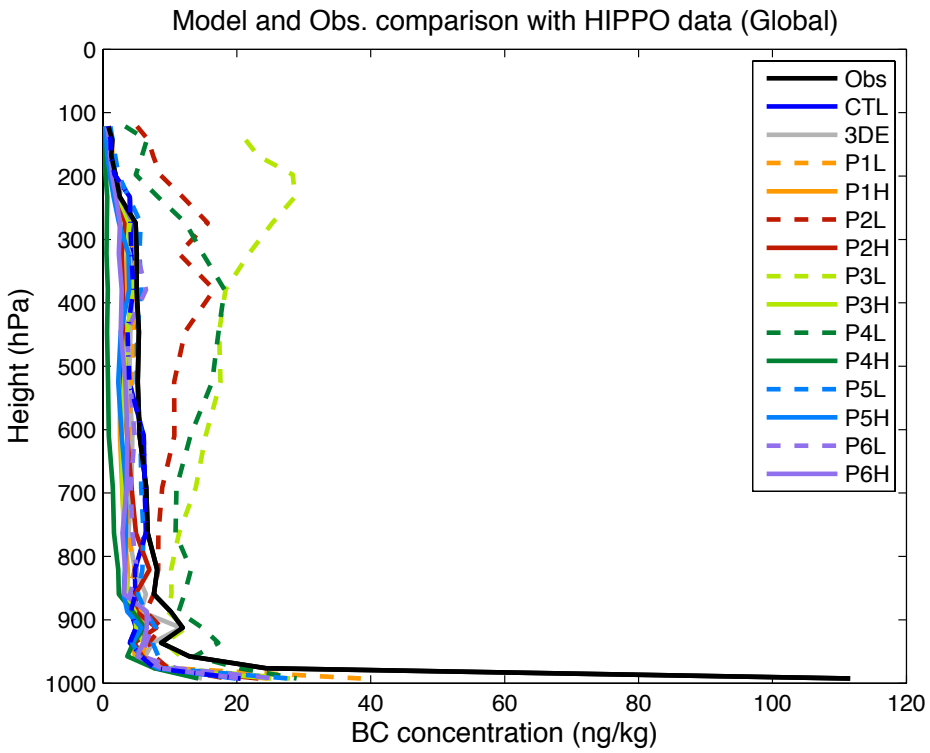

Figure 4.10: The same as Figure.4.6, but for the HIPPO campaign and averaged over all available samples collected globally in year 2009.

we target parameters that are expected to have strong effects on BC aerosol, while the total aerosol extinction is dominated by many other species. Yet the experiment P3L, in which we reduce the activation efficiency in convective clouds, shows relatively large high bias compared to the satellite observations in most regions, especially in the middle to high altitude troposphere. In the Eastern United States (EUS), North Atlantic Ocean (NAT) and Northwestern Pacific Ocean (NWP) regions, experiment P4L also reveals that high model bias may result from a globally uniform reduction of total liquid cloud content in the aerosol wet removal calculations. Thus it indicates that we need to consider more subtle methods to improve the aerosol activiation and wet removal processes in the model.

Another interesting phenomenon in Figure. 4.11 is that regardless of how strongly we perturb a parameter or model configuration, the simulated total aerosol extinction ceofficient profiles look very similar to the control run in terms of the shape. The simulated total aerosol fields from nearlly all perturbed parameter experiments are very similar to the CTL experiment, just scaled by a nearly constant factor from the surface to the top of atmosphere. We can see from this figure that in most regions, if the control simulation agrees quite well with the observations, the perturbed parameter experiments can slightly reduce the model biases at best. But if the control simulation itself is strongly biased, such as in region North Africa and Arabian Peninsula (NAF), the parameter perturbation cannot improve the comparison. This indicates that such biases may not originate from the errors in the model's physical parameterizations. The biases of simulated aerosol distribution are more likely to result from the limitation of the model resolution and the wrong representation of clouds (*Wang et al.*, 2013).

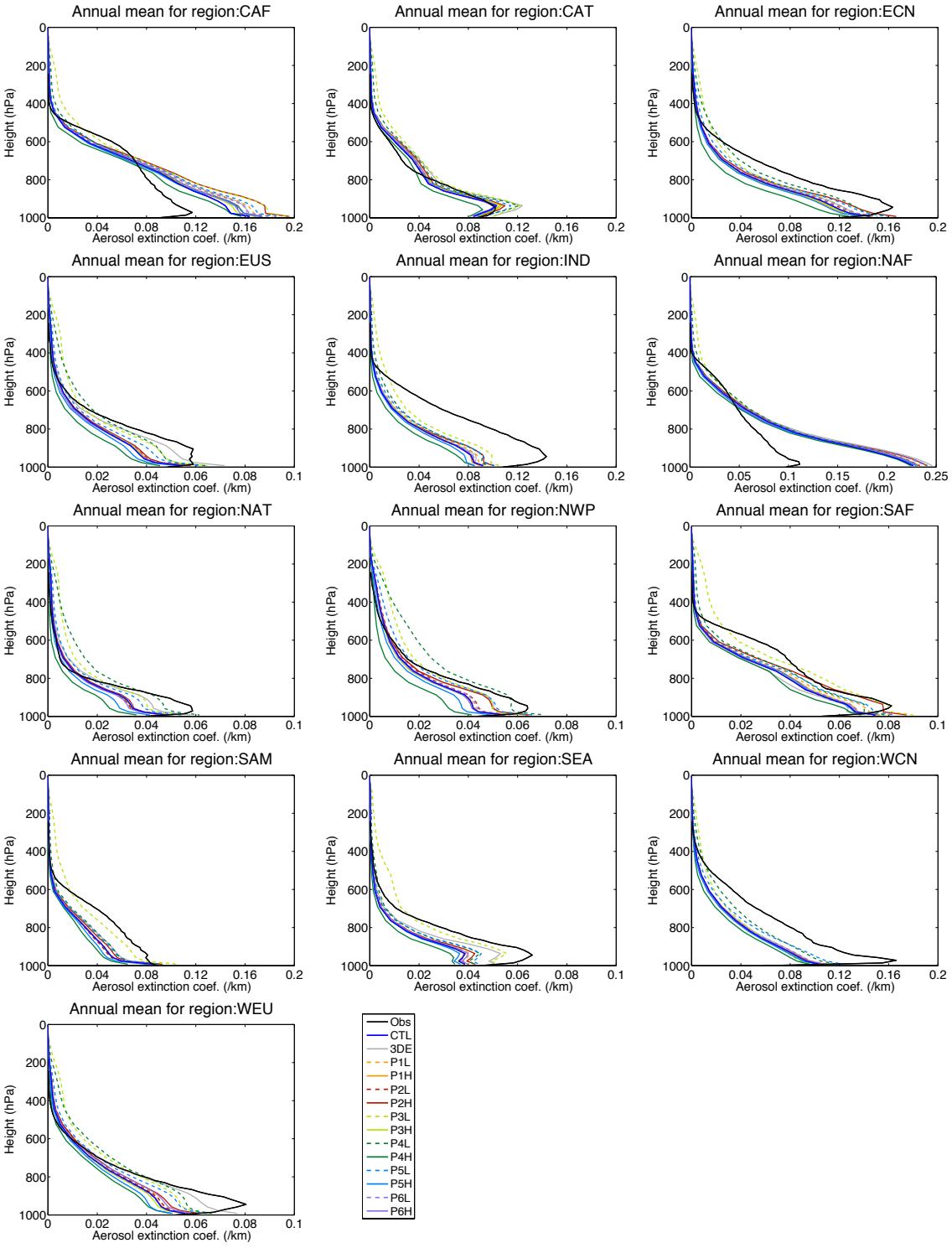

Figure 4.11: Comparison of annual mean simulated total aerosol extinction coefficient (km^{-1}) vertical profiles and the CALIOP satellite measurements. The data are averaged over years 2007 – 2009. Note the figures are plotted on different scales. The regions are defined as in Figure 1 in *Koffi et al.* (2012).

4.5 Conclusion

In this study, we explore how different physical parameterization settings and model configurations in CAM5 influence the simulated vertical distribution of aerosol fields, especially of black carbon. The simulation with default model configuration shows a substantial underestimate of BC concentration in the Arctic region compared to aircraft measurements. Results show that by prolonging the BC atmospheric lifetime or reducing the wet removal rate, the simulated BC concentration increases, especially in the middle to high altitude troposphere. Other parameters and model configurations show limited effect. Comparisons with total aerosol extinct coefficient observed with CALIPSO satellite show that reduced aerosol activation efficiency in convective cloud and reduced total liquid cloud content lead to overestimation of the aerosol extinct coefficient in most regions. This indicates that care must be taken when tuning these paremeters to archieve good performance in one particular region. This study also implies that in order to improve the simulated BC field in the Arctic, a better representation of wet removal process, including more realistic liquid cloud field, must be considered. A combination of well tuned parameters for reduction of wet removal efficiency, decreasing dry deposition velocity and prolonged BC atmospheric lifetime can be used to improve the model's simulated Arctic BC field.

CHAPTER V

Conclusion and Discussion

5.1 Summary of Results

In Chapter II, we simulated and evaluated the BC in snow concentrations and radiative effect in the Arctic. We applied the offline land and sea ice components of the Community Earth System Model version 1.0.3 (CESM) with the prescribed aerosol deposition fields from 25 models contributing to two phases of the AeroCom (Aerosol Comparisons between Observations and Models) project. Firstly we compare the simulated BC in snow concentration with an extensive field measurements campaign in the Arctic (*Doherty et al.*, 2010). We found that the models overestimate BC in snow concentration, especially for those models in Phase II, in most regions except northern Russia and Norway. The mean bias for AeroCom phase I models is -4.4 $(-13.2$ to $+10.7)\,\mathrm{ng\,g^{-1}}$ and for phase II models is $+4.1$ $(-13.0$ to $+21.4)\,\mathrm{ng\,g^{-1}}$, compared to the observational mean of $19.2\,\mathrm{ng\,g^{-1}}$.

Our results showed that the variation associated with aerosol emission inventories and meltwater scavenging efficiency have only limited contribution to the inter-model variations of simulated BC-in-snow distributions. Further analysis revealed that large inter-model variation in local BC deposition efficiency and Arctic BC atmospheric lifetime were likely to be the leading sources of the variation in model performance. We applied these simulation results to estimate the BC in snow radiative effects. The

multi-model mean of Arctic radiative effect from BC-in-snow is $0.15\,\mathrm{W\,m^{-2}}$ in phase I models, and $0.18\,\mathrm{W\,m^{-2}}$ in phase II models. We obtained our best estimate of the mean BC-in-snow Arctic radiative effect ($0.17\,\mathrm{W\,m^{-2}}$) after correcting for model biases relative to observed BC concentrations in different regions.

In Chapter III, we explored the potential changes of aerosol transport pathway and deposition processes in the Arctic in the context of climate change. We applied a modified version of the Bulk Aerosol Module (BAM) in the Community Atmosphere Model version 5 (CAM5) to track the distributions and fluxes of 200 black carbon like tracers emitted from different locations. In one experiment, we assigned identical constant e-folding atmospheric lifetime to all of the 200 tracers and study how the changes in transport pathway may influence their Arctic distribution. We found that under the Representative Concentration Pathway 8.5 (RCP8.5) future climate conditions, changing wind patterns caused the Arctic burdens of tracers emitted from East Asia and West Europe during winter to increase by about 20% compared to present climate. This change in wind pattern, however, decreases the Arctic burdens of North American emissions by 20 – 40%. Analysis indicated that the changing meteorological conditions result partially from an altered winter polar dome structure that results from Arctic amplification and inhomogeneous sea ice loss and surface warming.

In another experiment, all aerosol tracers are removed from the atmosphere with dry and wet deposition fluxes simulated by the model. When aerosol deposition is considered, changes in this term become the dominant driver of Arctic BC changes. Simulations showed that in future warming climate under the RCP8.5 scenario, the Arctic mean first-order removal rate increased by 23.3% in January. The increased removal rate is caused by increased cloud content and more liquid phase precipitation. Analysis showed that with a present day BC emission inventory, the Arctic annual mean burden would decrease by 13.6% by the end of 21st century, because of warming-

induced transport and deposition changes, while simulations with changing climate and emissions under RCP8.5 showed a 61.0% reduction.

In Chapter IV, we perturbed several physical parameters and model configurations in the Modal Aerosol Module with 7 Lognormal Modes (MAM7) in CAM5 to study their influences on the simulated vertical distribution of aerosol fields, especially for black carbon. We applied the observed vertical profile of BC mass concentration from four aircraft measurement campaigns (ARCTAS, ARCPAC, PAM-ARCMIP and HIPPO) to assess the model's performance. Control simulation with default model configuration showed large underestimation of BC concentration in the Arctic, especially in the middle to high altitude troposphere, compared to aircraft measurements. Results showed that in experiments with increased BC atmospheric lifetime or reduced wet removal rate, the biases between simulated BC vertical profile and aircraft observations decreased in the Arctic. Other parameters and model configurations showed moderate to limited effect. Comparisons with total aerosol extinct coefficient observed with CALIPSO satellite showed that the experiments with reduced aerosol activation efficiency in convective cloud and decreased total liquid cloud content overestimated the aerosol extinct coefficient in many regions. This indicates that a combination of well tuned parameters for reduction of wet removal efficiency, decreasing dry deposition velocity and prolonged BC atmospheric lifetime can be used to improve the model's simulated Arctic BC field, but these perturbation must be implemented carefully so as not to worsen the global simulation.

5.2 Future Studies

This thesis sheds light on several research topics that I would like to explore in future studies. In Chapter IV, we found that the parameters asscociated with aerosol's wet removal processes have large impacts on the simulated Arctic aerosol fields. Yet results also indicated that we need to tune those paremeters with caution as they

may perturb the aerosol simulation unrealistically in some regions. We also speculate that the simulated cloud field is also a key component for determining the aerosol field in the Arctic, since the modeled BC concentration increased substantially in high latitudes with reduced liquid cloud content. So as a next step, I will conduct several additional experiments with further perturbed model resolutions to investigate this process further. It is our hypothesis that high resolution simulations may be able to better resolve fine scale cloud characteristics, that are quite important for aerosol wet deposition processes. Improved resolution of the aerosol-cloud co-locations may lead to a better representation of simulated aerosol fields. Combined with the results from this thesis, I will explore whether refined model resolution globally or regionally could improve the simulated cloud fields and further reduce the biases in aerosol fields.

In addition, I would also like to design several experiments to combine some of the parameters in a single experiment but with different degrees of perturbations. For example, I plan to perturb the POM hygroscopicity and aerosol dry deposition velocity over snow and ice all together in a single experiment, as we are confident that those processes are represented incorrectly in the model. Those experiments will help us gain more knowledge about the parametrization of aerosol related processes in CAM5.

There are additional aerosol observations that we can use for the comparison as well. Firstly, there are several stations in the Arctic that collect near-surface BC measurements. The measurement locations include: Oliktok Point, Alaska; Barrow, Alaska; Alert, Canada; Zeppelin Station, Norway; Pallas, Finland and Station Nord, Greenland. Since we archived the BC in snow concentrations as well, we can also apply the measurements of BC in Arctic snow as in Chapter II. Comparison with the BC in snow measurements also help us to gain better understanding of how the BC related processes in the atmosphere may affect its distribution on the snow and ice surface in Arctic. The Aerosol Optical Depth (AOD) measurements collected by the

AErosol RObotic NETwork (AERONET) can also be compared with the simulated AOD from different experiments. This comparison will help us to assess the simulated global mean of AOD, which serves as a benchmark of the performance of global aerosol simulations.

BIBLIOGRAPHY

BIBLIOGRAPHY

Aan de Brugh, J. M. J., M. Schaap, E. Vignati, F. Dentener, M. Kahnert, M. Sofiev, V. Huijnen, and M. C. Krol (2011), The European aerosol budget in 2006, *Atmospheric Chemistry and Physics*, *11*(3), 1117–1139, doi:10.5194/acp-11-1117-2011.

Abdul-Razzak, H., and S. J. Ghan (2000), A parameterization of aerosol activation 2. Multiple aerosol types, *J. Geophys. Res.*, *105*(D5), 6837–6844.

Ackermann, I. J., H. Hass, M. Memmesheimer, A. Ebel, F. S. Binkowski, and U. Shankar (1998), Modal aerosol dynamics model for Europe: development and first applications, *Atmospheric Environment*, *32*(17), 2981 – 2999, doi: http://dx.doi.org/10.1016/S1352-2310(98)00006-5.

Barth, M. C., P. Rasch, J. T. Kiehl, C. M. Benkovitz, and S. E. Schwartz (2000), Sulfur chemistry in the National Center for Atmospheric Research Community Climate Model: Description, evaluation, features, and sensitivity to aqueous chemistry, *J. Geophys. Res.*, *105*(D1), doi:10.1029/1999JD900773.

Bauer, S. E., and D. Koch (2005), Impact of heterogeneous sulfate formation at mineral dust surfaces on aerosol loads and radiative forcing in the Goddard Institute for Space Studies general circulation model, *J. Geophys. Res.*, *110*(D17202), doi: 10.1029/2005JD005870.

Bauer, S. E., D. Koch, N. Unger, S. M. Metzger, D. T. Shindell, and D. G. Streets (2007), Nitrate aerosols today and in 2030: a global simulation including aerosols and tropospheric ozone, *Atmospheric Chemistry and Physics*, *7*(19), 5043–5059, doi:10.5194/acp-7-5043-2007.

Bauer, S. E., D. L. Wright, D. Koch, E. R. Lewis, R. McGraw, L.-S. Chang, S. E. Schwartz, and R. Ruedy (2008), MATRIX (Multiconfiguration Aerosol TRacker of mIXing state): an aerosol microphysical module for global atmospheric models, *Atmospheric Chemistry and Physics*, *8*(20), 6003–6035, doi:10.5194/acp-8-6003-2008.

Bauer, S. E., S. Menon, D. Koch, T. C. Bond, and K. Tsigaridis (2010), A global modeling study on carbonaceous aerosol microphysical characteristics and radiative effects, *Atmospheric Chemistry and Physics*, *10*(15), 7439–7456, doi:10.5194/acp-10-7439-2010.

Bellouin, N., J. Rae, A. Jones, C. Johnson, J. Haywood, and O. Boucher (2011), Aerosol forcing in the Climate Model Intercomparison Project (CMIP5) simulations by HadGEM2-ES and the role of ammonium nitrate, *J. Geophys. Res.*, *116*(D20206), doi:10.1029/2011JD016074.

Berglen, T. F., T. K. Berntsen, I. S. A. Isaksen, and J. K. Sundet (2004), A global model of the coupled sulfur/oxidant chemistry in the troposphere: The sulfur cycle, *J. Geophys. Res.*, *109*(D19310), doi:10.1029/2003JD003948.

Bian, H., M. Chin, J. M. Rodriguez, H. Yu, J. E. Penner, and S. Strahan (2009), Sensitivity of aerosol optical thickness and aerosol direct radiative effect to relative humidity, *Atmospheric Chemistry and Physics*, *9*(7), 2375–2386, doi:10.5194/acp-9-2375-2009.

Bintanja, R., and E. C. van der Linden (2013), The changing seasonal climate in the Arctic, *Nature*, *3*(1556), doi:10.1038/srep01556.

Bond, T. C., E. Bhardwaj, R. Dong, R. Jogani, S. Jung, C. Roden, D. G. Streets, and N. M. Trautmann (2007), Historical emissions of black and organic carbon aerosol from energy-related combustion, 1850–2000, *Global Biogeochem. Cycles*, *21*, GB2018, doi:10.1029/2006GB002840.

Bond, T. C., et al. (2013), Bounding the role of black carbon in the climate system: A scientific assessment, *Journal of Geophysical Research: Atmospheres*, pp. n/a–n/a, doi:10.1002/jgrd.50171.

Bourgeois, Q., and I. Bey (2011), Pollution transport efficiency toward the Arctic: Sensitivity to aerosol scavenging and source regions, *Journal of Geophysical Research: Atmospheres*, *116*(D8), n/a–n/a, doi:10.1029/2010JD015096.

Briegleb, B., and V. Ramanathan (1982), Spectral and diurnal variations in clear sky planetary albedo, *J. Appl. Meteor.*, *21*, 11601171, doi: http://dx.doi.org/10.1175/1520-0450(1982)021¡1160:SADVIC¿2.0.CO;2.

Briegleb, B. P., and B. Light (2007), A Delta-Eddington multiple scattering parameterization for solar radiation in the sea ice component of the Community Climate System Model, *Tech. Rep. NCAR/TN–472+STR*, National Center for Atmospheric Research.

Brock, C. A., et al. (2011), Characteristics, sources, and transport of aerosols measured in spring 2008 during the aerosol, radiation, and cloud processes affecting Arctic Climate (ARCPAC) Project, *Atmos. Chem. Phys.*, *11*(6), 2423–2453, doi: 10.5194/acp-11-2423-2011.

Browse, J., K. S. Carslaw, S. R. Arnold, K. Pringle, and O. Boucher (2012), The scavenging processes controlling the seasonal cycle in Arctic sulphate and black carbon aerosol, *Atmospheric Chemistry and Physics*, *12*(15), 6775–6798, doi:10.5194/acp-12-6775-2012.

Browse, J., K. S. Carslaw, A. Schmidt, and J. J. Corbett (2013), Impact of future Arctic shipping on high-latitude black carbon deposition, *Geophys. Res. Lett.*, *40*(16), 4459–4463, doi:10.1002/grl.50876.

Chin, M., T. Diehl, O. Dubovik, T. F. Eck, B. N. Holben, A. Sinyuk, and D. G. Streets (2009), Light absorption by pollution, dust, and biomass burning aerosols: a global model study and evaluation with AERONET measurements, *Annales Geophysicae*, *27*(9), 3439–3464, doi:10.5194/angeo-27-3439-2009.

Contini, D., A. Donateo, F. Belosi, F. M. Grasso, G. Santachiara, and F. Prodi (2010), Deposition velocity of ultrafine particles measured with the Eddy-Correlation Method over the Nansen Ice Sheet (Antarctica), *J. Geophys. Res.*, *115*, D16202, doi:10.1029/2009JD013600.

Conway, H., A. Gades, and C. F. Raymond (1996), Albedo of dirty snow during conditions of melt, *Water Resour. Res.*, *32*(6), doi:10.1029/96WR00712.

Corbett, J. J., D. A. Lack, J. J. Winebrake, S. Harder, J. A. Silberman, and M. Gold (2010), Arctic shipping emissions inventories and future scenarios, *Atmos. Chem. Phys.*, *10*(19), 9689–9704, doi:10.5194/acp-10-9689-2010.

de Meij, A., M. Krol, F. Dentener, E. Vignati, C. Cuvelier, and P. Thunis (2006), The sensitivity of aerosol in Europe to two different emission inventories and temporal distribution of emissions, *Atmospheric Chemistry and Physics*, *6*(12), 4287–4309, doi:10.5194/acp-6-4287-2006.

DeMott, P., A. Prenni, X. Liu, S. Kreidenweis, M. Petters, C. Twohy, M. Richardson, T. Eidhammer, and D. Rogers (2010), Predicting global atmospheric ice nuclei distributions and their impacts on climate, *Proceedings of the National Academy of Sciences*, *107*(25), 11,217–11,222.

Dentener, F., et al. (2006), Emissions of primary aerosol and precursor gases in the years 2000 and 1750 prescribed data-sets for AeroCom, *Atmospheric Chemistry and Physics*, *6*(12), 4321–4344, doi:10.5194/acp-6-4321-2006.

Doherty, S. J., S. G. Warren, T. C. Grenfell, A. D. Clarke, and R. E. Brandt (2010), Light-absorbing impurities in Arctic snow, *Atmospheric Chemistry and Physics*, *10*(23), 11,647–11,680, doi:10.5194/acp-10-11647-2010.

Doherty, S. J., T. C. Grenfell, S. Forsstrm, D. L. Hegg, R. E. Brandt, and S. G. Warren (2013), Observed vertical redistribution of black carbon and other insoluble light-absorbing particles in melting snow, *Journal of Geophysical Research: Atmospheres*, pp. n/a–n/a, doi:10.1002/jgrd.50235.

Dou, T., C. Xiao, D. T. Shindell, J. Liu, K. Eleftheriadis, J. Ming, and D. Qin (2012), The distribution of snow black carbon observed in the Arctic and compared to the GISS-PUCCINI model, *Atmospheric Chemistry and Physics*, *12*(17), 7995–8007, doi:10.5194/acp-12-7995-2012.

Duan, B., C. W. Fairall, and D. W. Thomson (1988), Eddy correlation measurements of the dry deposition of particles in wintertime, *J. Appl. Meteor.*, *27*(5), 642–652.

Easter, R. C., et al. (2004), MIRAGE: Model description and evaluation of aerosols and trace gases, *Journal of Geophysical Research: Atmospheres*, *109*(D20), n/a–n/a, doi:10.1029/2004JD004571.

Eckhardt, S., et al. (2015), Current model capabilities for simulating black carbon and sulfate concentrations in the Arctic atmosphere: a multi-model evaluation using a comprehensive measurement data set, *Atmospheric Chemistry and Physics*, *15*(16), 9413–9433, doi:10.5194/acp-15-9413-2015.

Flanner, M. G. (2013), Arctic climate sensitivity to local black carbon, *J. Geophys. Res. Atmos.*, *118*(4), 1840–1851, doi:10.1002/jgrd.50176.

Flanner, M. G., C. S. Zender, J. T. Randerson, and P. J. Rasch (2007), Present day climate forcing and response from black carbon in snow, *J. Geophys. Res.*, *112*, D11202, doi:10.1029/2006JD008003.

Flanner, M. G., C. S. Zender, P. G. Hess, N. M. Mahowald, T. H. Painter, V. Ramanathan, and P. J. Rasch (2009), Springtime warming and reduced snow cover from carbonaceous particles, *Atmos. Chem. Phys.*, *9*(7), 2481–2497.

Francis, J. A., and S. J. Vavrus (2012), Evidence linking Arctic amplification to extreme weather in mid-latitudes, *Geophys. Res. Lett.*, *39*(6), doi:10.1029/2012GL051000.

Gallagher, M. W., E. Nemitz, J. R. Dorsey, D. Fowler, M. A. Sutton, M. Flynn, and J. Duyzer (2002), Measurements and parameterizations of small aerosol deposition velocities to grassland, arable crops, and forest: Influence of surface roughness length on deposition, *J. Geophys. Res.*, *107*(D12), doi:10.1029/2001JD000817.

Garrett, T. J., C. Zhao, and P. C. Novelli (2010), Assessing the relative contributions of transport efficiency and scavenging to seasonal variability in Arctic aerosol, *Tellus*, *62B*, 190–196, doi:10.1111/j.1600-0889.2010.00453.x.

Garrett, T. J., S. Brattström, S. Sharma, D. E. Worthy, and P. Novelli (2011), The role of scavenging in the seasonal transport of black carbon and sulfate to the Arctic, *Geophys. Res. Lett.*, *38*(16), L16805, doi:10.1029/2011GL048221.

Gent, P. R., et al. (2011), The Community Climate System Model version 4, *J. Climate*, *24*, 4973–4991, doi:10.1175/2011JCLI4083.1.

Gettelman, A., H. Morrison, and S. J. Ghan (2008), A new two-moment bulk stratiform cloud microphysics scheme in the Community Atmospheric Model (CAM3), Part II: Single-Column and Global Results, *J. Climate*, *21*(15), 3642–3659.

Ghan, S. J., and R. C. Easter (2006), Impact of cloud-borne aerosol representation on aerosol direct and indirect effects, *Atmospheric Chemistry and Physics*, *6*(12), 4163–4174, doi:10.5194/acp-6-4163-2006.

Ghan, S. J., X. Liu, R. C. Easter, R. Zaveri, P. J. Rasch, , and J.-H. Yoon (2012), Toward a minimal representation of aerosols in climate models: Comparative decomposition of aerosol direct, semidirect, and indirect radiative forcing, *J. Climate*, *25*, doi:http://dx.doi.org/10.1175/JCLI-D-11-00650.1.

Grenfell, T. C., S. J. Doherty, A. D. Clarke, and S. G. Warren (2011), Light absorption from particulate impurities in snow and ice determined by spectrophotometric analysis of filters, *Appl. Opt.*, *50*(14), 2037–2048, doi:10.1364/AO.50.002037.

Grini, A., G. Myhre, J. K. Sundet, and I. S. A. Isaksen (2002), Modeling the Annual Cycle of Sea Salt in the Global 3D Model Oslo CTM2: Concentrations, Fluxes, and Radiative Impact, *J. Climate*, *15*, doi:http://dx.doi.org/10.1175/1520-0442(2002)015¡1717:MTACOS¿2.0.CO;2.

Grini, A., G. Myhre, C. S. Zender, and I. S. A. Isaksen (2005), Model simulations of dust sources and transport in the global atmosphere: Effects of soil erodibility and wind speed variability, *J. Geophys. Res.*, *110*(D02205), doi:10.1029/2004JD005037.

Hansen, J., and L. Nazarenko (2004), Soot climate forcing via snow and ice albedos, *101*(2), 423-428, doi:10.1073/pnas.2237157100.

Henderson-Sellers, A., and M. F. Wilson (1983), Surface albedo data for climatic modeling, *Reviews of Geophysics*, *21*(8), 1743–1778, doi:10.1029/RG021i008p01743.

Holland, M., D. A. Bailey, B. P. Briegleb, B. Light, and E. Hunke (2012), Improved sea ice shortwave radiation physics in CCSM4: The impact of melt ponds and aerosols on Arctic sea ice, *J. Climate*, *25*, 1413–1430, doi:10.1175/JCLI-D-11-00078.1.

Holland, M. M., and C. M. Bitz (2003), Polar amplification of climate change in coupled models, *Climate Dyn.*, *21*, 221–232, doi:10.1007/s00382-003-0332-6.

Hoose, C., and O. Möhler (2012), Heterogeneous ice nucleation on atmospheric aerosols: a review of results from laboratory experiments, *Atmospheric Chemistry and Physics*, *12*(20), 9817–9854, doi:10.5194/acp-12-9817-2012.

Hurrell, J. W., et al. (2013), The Community Earth System Model: A Framework for Collaborative Research, *Bulletin of the American Meteorological Society*, *94*(9), 1339–1360, doi:10.1175/BAMS-D-12-00121.1.

IPCC (2013), Climate Change 2013: The Physical Science Basis. Contribution of Working Group I to the Fifth Assessment Report of the Intergovernmental Panel on Climate Change, *Cambridge University Press, Cambridge, United Kingdom and New York, NY, USA*, p. 1535 pp, doi:doi:10.1017/CBO9781107415324.

Ito, A., and J. E. Penner (2005), Historical emissions of carbonaceous aerosols from biomass and fossil fuel burning for the period 18702000, *Global Biogeochemical Cycles*, *19*(2), n/a–n/a, doi:10.1029/2004GB002374.

Iversen, T., and Ø. Seland (2002), A scheme for process-tagged SO4 and BC aerosols in NCAR CCM3: Validation and sensitivity to cloud processes, *J. Geophys. Res.*, *107*(D24), doi:10.1029/2001JD000885.

Jacob, D. J., et al. (2010), The Arctic Research of the Composition of the Troposphere from Aircraft and Satellites (ARCTAS) mission: design, execution, and first results, *Atmospheric Chemistry and Physics*, *10*(11), 5191–5212, doi:10.5194/acp-10-5191-2010.

Jacobson, M. Z. (2004), Climate response of fossil fuel and biofuel soot, accounting for soot's feedback to snow and sea ice albedo and emissivity, *J. Geophys. Res.*, *109*, D21201, doi:10.1029/2004JD004945.

Jiao, C., et al. (2014), An AeroCom assessment of black carbon in Arctic snow and sea ice, *Atmospheric Chemistry and Physics*, *14*(5), 2399–2417, doi:10.5194/acp-14-2399-2014.

Kahn, R. (2012), Reducing the uncertainties in direct aerosol radiative forcing, *Surveys in Geophysics*, *33*(3-4), 701–721, doi:10.1007/s10712-011-9153-z.

Kaufman, Y. J., D. Tanre, and O. Boucher (2002), A satellite view of aerosols in the climate system, *Nature*.

Kinne, S., et al. (2006), An AeroCom initial assessment optical properties in aerosol component modules of global models, *Atmospheric Chemistry and Physics*, *6*(7), 1815–1834, doi:10.5194/acp-6-1815-2006.

Kipling, Z., P. Stier, J. P. Schwarz, A. E. Perring, J. R. Spackman, G. W. Mann, C. E. Johnson, and P. J. Telford (2013), Constraints on aerosol processes in climate models from vertically-resolved aircraft observations of black carbon, *Atmospheric Chemistry and Physics*, *13*(12), 5969–5986, doi:10.5194/acp-13-5969-2013.

Kirkevåg, A., and T. Iversen (2002), Global direct radiative forcing by process-parameterized aerosol optical properties, *J. Geophys. Res.*, *107*(D20), doi:10.1029/2001JD000886.

Kirkevåg, A., et al. (2013), Aerosol climate interactions in the norwegian earth system model noresm1-m, *Geoscientific Model Development*, *6*(1), 207–244, doi:10.5194/gmd-6-207-2013.

Kistler, R., et al. (1999), The NCEP-NCAR 50-Year Reanalysis: Monthly Means CD-ROM and Documentation, *Bull. Amer. Meteor. Soc.*, *82*, 247–267, doi:http://dx.doi.org/10.1175/1520-0477(2001)082¡0247:TNNYRM¿2.3.CO;2.

Klonecki, A., P. Hess, L. Emmons, L. Smith, J. Orlando, and D. Blake (2003), Seasonal changes in the transport of pollutants into the Arctic troposphere-model study, *Journal of Geophysical Research: Atmospheres*, *108*(D4), n/a–n/a, doi: 10.1029/2002JD002199.

Koch, D. (2001), Transport and direct radiative forcing of carbonaceous and sulfate aerosols in the GISS GCM, *J. Geophys. Res.*, *106*(D17), doi: 10.1029/2001JD900038.

Koch, D., and A. D. Del Genio (2010), Black carbon semi-direct effects on cloud cover: review and synthesis, *Atmospheric Chemistry and Physics*, *10*(16), 7685–7696, doi:10.5194/acp-10-7685-2010.

Koch, D., and J. Hansen (2005), Distant origins of Arctic black carbon: A Goddard Institute for Space Studies ModelE experiment, *J. Geophys. Res.*, *110*, D04204, doi:10.1029/2004JD005296.

Koch, D., G. A. Schmidt, and C. Field (2006), Sulfur, sea salt and radionuclide aerosols in GISS ModelE, *J. Geophys. Res.*, *111*(D06206), doi: 10.1029/2004JD005550.

Koch, D., T. C. Bond, D. Streets, N. Unger, , and G. R. van der Werf (2007), Global impacts of aerosols from particular source regions and sectors, *J. Geophys. Res.*, *112*(D02205), doi:10.1029/2005JD007024.

Koch, D., S. Menon, A. D. Genio, R. Ruedy, I. Alienov, and G. A. Schmidt (2009a), Distinguishing aerosol impacts on climate over the past century, *J. Climate*, *22*, 2659–2677.

Koch, D., et al. (2009b), Evaluation of black carbon estimations in global aerosol models, *Atmospheric Chemistry and Physics*, *9*(22), 9001–9026, doi:10.5194/acp-9-9001-2009.

Koch, D., et al. (2011), Soot microphysical effects on liquid clouds, a multimodel investigation, *Atmospheric Chemistry and Physics*, *11*(3), 1051–1064, doi: 10.5194/acp-11-1051-2011.

Koffi, B., et al. (2012), Application of the CALIOP layer product to evaluate the vertical distribution of aerosols estimated by global models: AeroCom phase I results, *J. Geophys. Res.*, *117*, D10201, doi:10.1029/2011JD016858.

Krol, M., S. Houweling, B. Bregman, M. van den Broek, A. Segers, P. van Velthoven, W. Peters, F. Dentener, and P. Bergamaschi (2005), The two-way nested global chemistry-transport zoom model TM5: algorithm and applications, *Atmospheric Chemistry and Physics*, *5*(2), 417–432, doi:10.5194/acp-5-417-2005.

Lamarque, J.-F., G. Kyle, M. Meinshausen, K. Riahi, S. Smith, D. van Vuuren, A. Conley, and F. Vitt (2011), Global and regional evolution of short-lived

radiatively-active gases and aerosols in the Representative Concentration Pathways, *Climatic Change*, *109*(1-2), 191–212, doi:10.1007/s10584-011-0155-0.

Lamarque, J.-F., et al. (2010), Historical (1850–2000) gridded anthropogenic and biomass burning emissions of reactive gases and aerosols: methodology and application, *Atmos. Chem. Phys.*, *10*(15), 7017–7039, doi:10.5194/acp-10-7017-2010.

Lamarque, J.-F., et al. (2012), CAM-chem: description and evaluation of interactive atmospheric chemistry in the Community Earth System Model, *Geoscientific Model Development*, *5*(2), 369–411, doi:10.5194/gmd-5-369-2012.

Law, K. S., and A. Stohl (2007), Arctic air pollution: Origins and impacts, *Science*, *315*, 1537–1540.

Lawrence, D., et al. (2011), Parameterization Improvements and Functional and Structural Advances in Version 4 of the Community Land Model, *Journal of Advances in Modeling Earth Systems*, *3*(45), doi:10.1029/JAMES.2011.3.45.

Lawrence, P. J., and T. N. Chase (2007), Representing a new MODIS consistent land surface in the Community Land Model (CLM 3.0), *Journal of Geophysical Research: Biogeosciences*, *112*(G1), n/a–n/a, doi:10.1029/2006JG000168.

Lee, L. A., K. J. Pringle, C. L. Reddington, G. W. Mann, P. Stier, D. V. Spracklen, J. R. Pierce, and K. S. Carslaw (2013a), The magnitude and causes of uncertainty in global model simulations of cloud condensation nuclei, *Atmospheric Chemistry and Physics*, *13*(17), 8879–8914, doi:10.5194/acp-13-8879-2013.

Lee, M.-Y., C.-C. Hong, and H.-H. Hsu (2015), Compounding effects of warm sea surface temperature and reduced sea ice on the extreme circulation over the extratropical North Pacific and North America during the 20132014 boreal winter, *Geophysical Research Letters*, *42*(5), 1612–1618, doi:10.1002/2014GL062956.

Lee, Y. H., et al. (2013b), Evaluation of preindustrial to present-day black carbon and its albedo forcing from Atmospheric Chemistry and Climate Model Intercomparison Project (ACCMIP), *Atmospheric Chemistry and Physics*, *13*(5), 2607–2634, doi:10.5194/acp-13-2607-2013.

Liu, J., S. Fan, L. W. Horowitz, and H. Levy II (2011), Evaluation of factors controlling long-range transport of black carbon to the Arctic, *J. Geophys. Res.*, *116*(D4), D04307, doi:10.1029/2010JD015145.

Liu, X., and J. E. Penner (2002), Effect of Mount Pinatubo H2SO4/H2O aerosol on ice nucleation in the upper troposphere using a global chemistry and transport model, *Journal of Geophysical Research: Atmospheres*, *107*(D12), AAC 2–1–AAC 2–18, doi:10.1029/2001JD000455.

Liu, X., et al. (2012), Toward a minimal representation of aerosols in climate models: description and evaluation in the Community Atmosphere Model CAM5, *Geosci. Model Dev.*, *5*(3), 709–739, doi:10.5194/gmd-5-709-2012.

Lund, M. T., and T. Berntsen (2012), Parameterization of black carbon aging in the OsloCTM2 and implications for regional transport to the Arctic, *Atmospheric Chemistry and Physics*, *12*(15), 6999–7014, doi:10.5194/acp-12-6999-2012.

Ma, P.-L., J. R. Gattiker, X. Liu, and P. J. Rasch (2013), A novel approach for determining source–receptor relationships in model simulations: a case study of black carbon transport in northern hemisphere winter, *Environmental Research Letters*, *8*(2), 024,042.

McConnell, J. R., et al. (2007), 20th-century industrial black carbon emissions altered Arctic climate forcing, *Science*, *317*(5843), 1381–1384, doi: 10.1126/science.1144856.

Menon, S., J. Hansen, L. Nazarenko, and Y. Luo (2002), Climate Effects of Black Carbon Aerosols in China and India, *Science*, *297*(5590), 2250–2253, doi: 10.1126/science.1075159.

Morrison, H., and A. Gettelman (2008), A new two-moment bulk stratiform cloud microphysics scheme in the Community Atmospheric Model (CAM3), Part I: Description and numerical tests, *J. Climate*, *21*(15), 3642–3659.

Myhre, G., et al. (2007), Comparison of the radiative properties and direct radiative effect of aerosols from a global aerosol model and remote sensing data over ocean, *Tellus B*, *59*(1), 115–129, doi:10.1111/j.1600-0889.2006.00226.x.

Myhre, G., et al. (2009), Modelled radiative forcing of the direct aerosol effect with multi-observation evaluation, *Atmospheric Chemistry and Physics*, *9*(4), 1365–1392, doi:10.5194/acp-9-1365-2009.

Myhre, G., et al. (2013), Radiative forcing of the direct aerosol effect from AeroCom Phase II simulations, *Atmospheric Chemistry and Physics*, *13*(4), 1853–1877, doi: 10.5194/acp-13-1853-2013.

Nilsson, E. D., and U. Rannik (2001), Turbulent aerosol fluxes over the Arctic Ocean: 1. Dry deposition over sea and pack ice, *J. Geophys. Res.*, *106*(D23), 32,125–32,137, doi:10.1029/2000JD900605.

Novakov, T., and J. E. Penner (1993), Large contribution of organic aerosols to cloud-condensation-nuclei concentrations, *Nature*, *365*(6449), 823–826.

Oleson, K. W., D. M. Lawrence, G. B. Bonan, M. G. Flanner, E. Kluzek, P. J. Lawrence, S. Levis, S. C. Swenson, and P. E. Thornton (2010), *Technical Description of version 4.0 of the Community Land Model (CLM)*, National Center for Atmospheric Research.

Penner, J. E., L. Xu, and M. Wang (2011), Satellite methods underestimate indirect climate forcing by aerosols, *Proceedings of the National Academy of Sciences*, *108*(33), 13,404–13,408, doi:10.1073/pnas.1018526108.

Pitari, G., E. Mancini, V. Rizi, and D. T. Shindell (2002), Impact of future climate and emission changes on stratospheric aerosols and ozone, *J. Atmos. Sci.*, *59*, doi: http://dx.doi.org/10.1175/1520-0469(2002)059¡0414:IOFCAE¿2.0.CO;2.

Pitari, G., et al. (2008), Radiative forcing from particle emissions by future supersonic aircraft, *Atmospheric Chemistry and Physics*, *8*(14), 4069–4084, doi:10.5194/acp-8-4069-2008.

Ramanathan, V., and G. Carmichael (2008), Global and regional climate changes due to black carbon, *Nature Geosci.*, *1*, 221–227.

Rao, S., and K. Riahi (2006), The role of Non-CO2 greenhouse gases in climate change mitigation: Long-term scenarios for the 21st century, *The Energy Journal*, *27*, 177–200.

Rasch, P. J., W. D. Collins, and B. E. Eaton (2001), Understanding the Indian Ocean Experiment (INDOEX) aerosol distributions with an aerosol assimilation, *J. Geophys. Res.*, *106*(D7), doi:10.1029/2000JD900508.

Rasch, P. J., et al. (2000), A comparison of scavenging and deposition processes in global models: results from the WCRP Cambridge Workshop of 1995, *Tellus B*, *52*(4), 1025–1056, doi:10.1034/j.1600-0889.2000.00980.x.

Rayner, N. A., D. E. Parker, E. B. Horton, C. K. Folland, L. V. Alexander, D. P. Rowell, E. C. Kent, and A. Kaplan (2003), Global analyses of sea surface temperature, sea ice, and night marine air temperature since the late nineteenth century, *Journal of Geophysical Research: Atmospheres*, *108*(D14), n/a–n/a, doi: 10.1029/2002JD002670.

Reddy, M. S., and O. Boucher (2004), A study of the global cycle of carbonaceous aerosols in the LMDZT general circulation model, *Journal of Geophysical Research: Atmospheres*, *109*(D14), n/a–n/a, doi:10.1029/2003JD004048.

Riahi, K., A. Grbler, and N. Nakicenovic (2007), Scenarios of long-term socio-economic and environmental development under climate stabilization, *Technological Forecasting and Social Change*, *74*(7), 887 – 935, doi: http://dx.doi.org/10.1016/j.techfore.2006.05.026, greenhouse Gases - Integrated Assessment.

Riahi, K., S. Rao, V. Krey, C. Cho, V. Chirkov, G. Fischer, G. Kindermann, N. Nakicenovic, and P. Rafaj (2011), RCP 8.5A scenario of comparatively high greenhouse gas emissions, *Climatic Change*, *109*(1-2), 33–57, doi:10.1007/s10584-011-0149-y.

Samset, B. H., et al. (2013), Black carbon vertical profiles strongly affect its radiative forcing uncertainty, *Atmospheric Chemistry and Physics*, *13*(5), 2423–2434, doi: 10.5194/acp-13-2423-2013.

Schulz, M., M. Chin, and S. Kinne (2009), The Aerosol Model Comparison Project, AeroCom, Phase II: Clearing Up Diversity, *IGAC Newsletter*, (No.41).

Schulz, M., et al. (2006), Radiative forcing by aerosols as derived from the AeroCom present-day and pre-industrial simulations, *Atmospheric Chemistry and Physics*, *6*(12), 5225–5246, doi:10.5194/acp-6-5225-2006.

Schwarz, J. P., J. R. Spackman, R. S. Gao, L. A. Watts, P. Stier, M. Schulz, S. M. Davis, S. C. Wofsy, and D. W. Fahey (2010), Global-scale black carbon profiles observed in the remote atmosphere and compared to models, *Geophysical Research Letters*, *37*(18), n/a–n/a, doi:10.1029/2010GL044372.

Screen, J. A., and I. Simmonds (2010), The central role of diminishing sea ice in recent Arctic temperature amplification, *Nature*, *464*, 1334–1337, doi: 10.1038/nature09051.

Screen, J. A., C. Deser, and I. Simmonds (2012), Local and remote controls on observed Arctic warming, *Geophys. Res. Lett.*, *39*(10), L10709, doi: 10.1029/2012GL051598.

Seland, Ø., T. Iversen, A. Kirkevåg, and T. Storelvmo (2008), Aerosol-climate interactions in the CAM-Oslo atmospheric GCM and investigation of associated basic shortcomings, *Tellus A*, *60*(3), 459–491, doi:10.1111/j.1600-0870.2008.00318.x.

Serreze, M. C., A. P. Barrett, J. C. Stroeve, D. N. Kindig, and M. M. Holland (2009), The emergence of surface-based Arctic amplification, *The Cryosphere*, *3*(1), 11–19.

Sharma, S., E. Andrews, L. A. Barrie, J. A. Ogren, and D. Lavoue (2006), Variations and sources of the equivalent black carbon in the High Arctic revealed by long term observations at Alert and Barrow: 1989–2003, *J. Geophys. Res*, *111*, D14208, doi:10.1029/2005JD006581.

Shindell, D., and G. Faluvegi (2009), Climate response to regional radiative forcing during the twentieth century, *Nature Geosci*, *2*(4), 294–300.

Shindell, D. T., et al. (2008), A multi-model assessment of pollution transport to the Arctic, *Atmos. Chem. Phys.*, *8*, 5353–5372.

Shindell, D. T., et al. (2013), Radiative forcing in the ACCMIP historical and future climate simulations, *Atmospheric Chemistry and Physics*, *13*(6), 2939–2974, doi: 10.5194/acp-13-2939-2013.

Skeie, R. B., T. Berntsen, G. Myhre, C. A. Pedersen, J. Ström, S. Gerland, and J. A. Ogren (2011a), Black carbon in the atmosphere and snow, from pre-industrial times until present, *Atmospheric Chemistry and Physics*, *11*(14), 6809–6836, doi: 10.5194/acp-11-6809-2011.

Skeie, R. B., T. K. Berntsen, G. Myhre, K. Tanaka, M. M. Kvalevåg, and C. R. Hoyle (2011b), Anthropogenic radiative forcing time series from pre-industrial times until 2010, *Atmospheric Chemistry and Physics*, *11*(22), 11,827–11,857, doi:10.5194/acp-11-11827-2011.

Spracklen, D. V., K. J. Pringle, K. S. Carslaw, M. P. Chipperfield, and G. W. Mann (2005), A global off-line model of size-resolved aerosol microphysics: I. Model development and prediction of aerosol properties, *Atmospheric Chemistry and Physics*, *5*(8), 2227–2252, doi:10.5194/acp-5-2227-2005.

Spracklen, D. V., K. S. Carslaw, U. Pöschl, A. Rap, and P. M. Forster (2011), Global cloud condensation nuclei influenced by carbonaceous combustion aerosol, *Atmospheric Chemistry and Physics*, *11*(17), 9067–9087, doi:10.5194/acp-11-9067-2011.

Sterle, K. M., J. R. McConnell, J. Dozier, R. Edwards, and M. G. Flanner (2013), Retention and radiative forcing of black carbon in eastern Sierra Nevada snow, *The Cryosphere*, *7*(1), 365–374, doi:10.5194/tc-7-365-2013.

Stevens, B., and G. Feingold (2009), Untangling aerosol effects on clouds and precipitation in a buffered system, *Nature*, *461*, 607–613, doi:10.1038/nature08281.

Stier, P., J. H. Seinfeld, S. Kinne, and O. Boucher (2007), Aerosol absorption and radiative forcing, *Atmospheric Chemistry and Physics*, *7*(19), 5237–5261, doi:10.5194/acp-7-5237-2007.

Stier, P., et al. (2005), The aerosol-climate model ECHAM5-HAM, *Atmospheric Chemistry and Physics*, *5*(4), 1125–1156, doi:10.5194/acp-5-1125-2005.

Stier, P., et al. (2013), Host model uncertainties in aerosol radiative forcing estimates: results from the AeroCom Prescribed intercomparison study, *Atmospheric Chemistry and Physics*, *13*(6), 3245–3270, doi:10.5194/acp-13-3245-2013.

Stohl, A. (2006), Characteristics of atmospheric transport into the Arctic troposphere, *J. Geophys. Res.*, *111*, D11306, doi:10.1029/2005JD006888.

Stohl, A., Z. Klimont, S. Eckhardt, K. Kupiainen, V. P. Shevchenko, V. M. Kopeikin, and A. N. Novigatsky (2013), Black carbon in the Arctic: the underestimated role of gas flaring and residential combustion emissions, *Atmospheric Chemistry and Physics*, *13*(17), 8833–8855, doi:10.5194/acp-13-8833-2013.

Stone, R. S., et al. (2010), A three-dimensional characterization of Arctic aerosols from airborne Sun photometer observations: PAM-ARCMIP, April 2009, *J. Geophys. Res.: Atmos.*, *115*(D13), doi:10.1029/2009JD013605.

Szopa, S., et al. (2013), Aerosol and ozone changes as forcing for climate evolution between 1850 and 2100, *Climate Dynamics*, *40*(9-10), 2223–2250, doi:10.1007/s00382-012-1408-y.

Takemura, T., T. Nozawa, S. Emori, T. Y. Nakajima, and T. Nakajima (2005), Simulation of climate response to aerosol direct and indirect effects with aerosol transport-radiation model, *J. Geophys. Res.*, *110*(D02202), doi:10.1029/2004JD005029.

Takemura, T., M. Egashira, K. Matsuzawa, H. Ichijo, R. O'ishi, and A. Abe-Ouchi (2009), A simulation of the global distribution and radiative forcing of soil dust aerosols at the last glacial maximum, *Atmospheric Chemistry and Physics*, *9*(9), 3061–3073, doi:10.5194/acp-9-3061-2009.

Textor, C., et al. (2006), Analysis and quantification of the diversities of aerosol life cycles within AeroCom, *Atmospheric Chemistry and Physics*, *6*(7), 1777–1813, doi:10.5194/acp-6-1777-2006.

Textor, C., et al. (2007), The effect of harmonized emissions on aerosol properties in global models an AeroCom experiment, *Atmospheric Chemistry and Physics*, *7*(17), 4489–4501, doi:10.5194/acp-7-4489-2007.

Vignati, E., M. Karl, M. Krol, J. Wilson, P. Stier, and F. Cavalli (2010), Sources of uncertainties in modelling black carbon at the global scale, *Atmospheric Chemistry and Physics*, *10*(6), 2595–2611, doi:10.5194/acp-10-2595-2010.

von Hardenberg, J., L. Vozella, C. Tomasi, V. Vitale, A. Lupi, M. Mazzola, T. P. C. van Noije, A. Strunk, and A. Provenzale (2012), Aerosol optical depth over the Arctic: a comparison of ECHAM-HAM and TM5 with ground-based, satellite and reanalysis data, *Atmospheric Chemistry and Physics*, *12*(15), 6953–6967, doi:10.5194/acp-12-6953-2012.

Wang, H., P. J. Rasch, R. C. Easter, B. Singh, R. Zhang, P.-L. Ma, Y. Qian, S. J. Ghan, and N. Beagley (2014a), Using an explicit emission tagging method in global modeling of source-receptor relationships for black carbon in the Arctic: Variations, sources, and transport pathways, *Journal of Geophysical Research: Atmospheres*, *119*(22), 12,888–12,909, doi:10.1002/2014JD022297.

Wang, H., et al. (2013), Sensitivity of remote aerosol distributions to representation of cloud–aerosol interactions in a global climate model, *Geosci. Model Dev.*, *6*(3), 765–782, doi:10.5194/gmd-6-765-2013.

Wang, Q., et al. (2011), Sources of carbonaceous aerosols and deposited black carbon in the Arctic in winter–spring: implications for radiative forcing, *Atmos. Chem. Phys.*, *11*(23), 12,453–12,473, doi:10.5194/acp-11-12453-2011.

Wang, Q., et al. (2014b), Global budget and radiative forcing of black carbon aerosol: Constraints from pole-to-pole (HIPPO) observations across the Pacific, *Journal of Geophysical Research: Atmospheres*, *119*(1), 195–206, doi:10.1002/2013JD020824.

Warneke, C., et al. (2010), An important contribution to springtime Arctic aerosol from biomass burning in Russia, *Geophys. Res. Lett*, *37*(5), L01801, doi:10.1029/2009GL041816.

Winkeri, D. M., et al. (2010), The CALIPSO Mission: A Global 3D View of Aerosols and Clouds, *Bull. Amer. Meteor. Soc.*, *91*, 1211–1229, doi:http://dx.doi.org/10.1175/2010BAMS3009.1.

Wofsy, S. C., et al. (2011), HIAPER Pole-to-Pole Observations (HIPPO): fine-grained, global-scale measurements of climatically important atmospheric gases and aerosols, *Phil. Trans. R. Soc. A*, *369*(1943), 2073–2086, doi:10.1098/rsta.2010.0313.

Xu, B., J. Cao, D. R. Joswiak, X. Liu, H. Zhao, and J. He (2012), Post-depositional enrichment of black soot in snow-pack and accelerated melting of Tibetan glaciers, *Environ. Res. Lett.*, *7*(014022), doi:10.1088/1748-9326/7/1/014022.

Yu, H., M. Chin, D. M. Winker, A. H. Omar, Z. Liu, C. Kittaka, and T. Diehl (2010), Global view of aerosol vertical distributions from CALIPSO lidar measurements and GOCART simulations: Regional and seasonal variations, *Journal of Geophysical Research: Atmospheres*, *115*(D4), n/a–n/a, doi:10.1029/2009JD013364.

Yun, Y., and J. E. Penner (2012), Global model comparison of heterogeneous ice nucleation parameterizations in mixed phase clouds, *Journal of Geophysical Research: Atmospheres*, *117*(D7), n/a–n/a, doi:10.1029/2011JD016506.

Zhang, K., et al. (2012), The global aerosol-climate model ECHAM-HAM, version 2: sensitivity to improvements in process representations, *Atmospheric Chemistry and Physics*, *12*(19), 8911–8949, doi:10.5194/acp-12-8911-2012.

Zhou, C., J. E. Penner, M. G. Flanner, M. M. Bisiaux, R. Edwards, and J. R. McConnell (2012), Transport of black carbon to polar regions: Sensitivity and forcing by black carbon, *Geophysical Research Letters*, *39*(22), n/a–n/a, doi:10.1029/2012GL053388.